





This is to certify that the  
thesis entitled  
AN EVALUATION OF HIGH ENERGY ION  
IMPLANTATION FOR WEAR STUDIES

presented by  
Todd L. Rachel

has been accepted towards fulfillment  
of the requirements for

M.S. degree in Mechanical  
Engineering



Major professor

Date March 8, 1991

**LIBRARY  
Michigan State  
University**

**PLACE IN RETURN BOX to remove this checkout from your record.  
TO AVOID FINES return on or before date due.**

<b>DATE DUE</b>	<b>DATE DUE</b>	<b>DATE DUE</b>
<del>APR 22 2003</del>	_____	_____
APR 22 2003 <del>041403</del>	_____	_____
_____	_____	_____
_____	_____	_____
_____	_____	_____
_____	_____	_____
_____	_____	_____

**MSU is An Affirmative Action/Equal Opportunity Institution**

**AN EVALUATION OF HIGH ENERGY ION IMPLANTATION  
FOR WEAR STUDIES**

**By**

**Todd L Rachel**

**A THESIS**

**Submitted to  
Michigan State University  
in partial fulfillment of the requirements  
for the degree of**

**MASTER OF SCIENCE**

**Department of Mechanical Engineering**

**1991**

657-4129

## ABSTRACT

### AN EVALUATION OF HIGH ENERGY ION IMPLANTATION FOR WEAR STUDIES

By

**Todd L Rachel**

The use of radiotracers in wear studies has shown to have a clear advantage over other wear measuring techniques. One type of radiotracer measurement technique is that of Ion Implantation in which an accelerated ion beam penetrates the surface of an engine part to be worn and implants radioactive beam nuclei. As the part is subjected to mechanical friction, the ions are collected in the engine oil and detected as the implanted material is worn away. This technique has many advantages, but one possible disadvantage is the change in nature of the target material, which has the possibility of changing the wear rate of the part. To determine if material properties are affected, a  $^{20}\text{Ne}$ , 2.5 MeV / nucleon non-radioactive beam was used to implant varying amounts of ions ( $2 \times 10^{12}$ ,  $2 \times 10^{13}$ , and  $2 \times 10^{14}$  ions/cm<sup>2</sup>) into ceramic and stainless steel specimens. The specimens were then tested for a change in hardness and elastic modulus due the implantation of ions using a Nano Indentation Machine. The ceramic material, silicon nitride, and the stainless steel 17-4PH both showed a decrease in hardness and elastic modulus due to ion implantation at the ion dosage of  $2 \times 10^{14}$  ions/cm<sup>2</sup>. The  $2 \times 10^{13}$  and  $2 \times 10^{12}$  ions/cm<sup>2</sup> dosages showed no change in hardness or elastic modulus. Finally, an ion implantation detection system required to detect gamma radiation for engine wear studies was designed.

## **ACKNOWLEDGMENTS**

**I would like to give thanks to several important people.**

**To Dr. Schock, my major professor, who through his knowledge and guidance made this project successful.**

**To my good friend Tom Stuecken for the machining of associated hardware and who gave me a life time of knowledge and invaluable assistance.**

**To Dr. Ronningen for the tedious instruction on the use of the gamma ray detector, patience and late nights especially during the cyclotron run.**

**To Richard Shalek for the stainless steel preparation, fabrication of the gold foil degraders, helpful knowledge and companionship at Oak Ridge National Laboratory.**

**To Dr. Grummon for his instruction and gold foil fabrication.**

**To Dr. McHarris for his helpful comments.**

**To my advisory committee Dr. Schock, Dr. Grummon and Dr. Sommerton for their guidance.**

**To my wife for being so understanding and supportive throughout my masters program.**

**And to my family, who with their scholastic persistence in my younger years, their constant support and substantial financial contributions, made my education possible.**

## TABLE OF CONTENTS

	Page
LIST OF TABLES.....	vi
LIST OF FIGURES .....	vii
CHAPTER 1 - INTRODUCTION.....	1
1.1 Problem Statement.....	1
1.2 Literature Survey .....	3
CHAPTER 2 - FACILITIES AND SYSTEM COMPONENTS .....	5
2.1 Wear Specimens.....	5
2.2 Buehler Polisher / Grinder Machine .....	8
2.3 Cyclotron .....	9
2.4 Nuclear Radioisotopes .....	11
2.5 Ion Implanting Depth Model (TRIM).....	15
2.6 Gamma Ray Analysis System.....	17
2.6.1 Gamma ray Detection System .....	18
2.6.1.1 Gamma ray Detector and Accessories .....	18
2.6.1.2 Preamplifier.....	19
2.6.1.3 Cryostat/Dewar System .....	19
2.6.2 Pulse Modification System .....	20
2.6.2.1 Amplifier.....	20
2.6.2.2 Analog to Digital Converter (ADC) .....	22
2.6.2.3 Digital Stabilizer .....	24
2.6.3 Liquid Nitrogen System.....	25
2.6.4 Multichannel Analyzing System.....	27
2.6.4.1 System 100.....	27
2.6.4.2 MicroSampo.....	28
2.7 Nano- Indentation Machine .....	29

	Page
<b>CHAPTER 3 - PREPARATION AND PROCEDURES .....</b>	<b>37</b>
<b>3.1 Specimen Preparation .....</b>	<b>37</b>
<b>3.2 TRIM .....</b>	<b>41</b>
<b>3.3 Cyclotron Ion Implantation.....</b>	<b>45</b>
<b>3.4 Nano Indentation.....</b>	<b>52</b>
<b>CHAPTER 4 - RESULTS AND DISCUSSION .....</b>	<b>61</b>
<b>4.1 Detection of Specimen's Radioactivity .....</b>	<b>61</b>
<b>4.2 Nano Indentation.....</b>	<b>64</b>
<b>4.3 TRIM .....</b>	<b>91</b>
<b>CHAPTER 5 - SUMMARY AND CONCLUSIONS.....</b>	<b>95</b>
<b>CHAPTER 6 - RECOMMENDATIONS .....</b>	<b>97</b>
<b>LIST OF REFERENCES.....</b>	<b>98</b>
<b>APPENDIX - DESIGN OF ION IMPLANTATION WEAR SYSTEM.....</b>	<b>100</b>

## LIST OF TABLES

	Page
Table 1 Silicon Nitride Components .....	5
Table 2 Silicon Nitride Properties.....	6
Table 3 17-4PH Stainless Steel Components .....	7
Table 4 17-4PH Stainless Steel Properties.....	8
Table 5 Surface Preparation Procedure for Silicon Nitride .....	39
Table 6 Surface Preparation Procedure for Stainless Steel.....	40
Table 7 'Doubled Specimens' Test Matrix.....	48
Table 8 Actual Number of Ions Implanted in Specimens.....	50
Table 9 Cyclotron Beam Current Variation.....	50
Table 10 Beam Degradation Foil Thickness.....	51
Table 11 'Single Specimen' Test Matrix .....	51
Table 12 Activity of Silicon Nitride no. 6 .....	61
Table 13 Spectrum Energy Calibration.....	63
Table 14 Varying Hardness Values .....	67
Table 15 Exhaust Activity Verses Blower Flow Rate .....	105

## LIST OF FIGURES

	Page
Figure 1 Target Pod Set Up .....	10
Figure 2 Stable Nuclei .....	12
Figure 3 Nucleon Binding Energy .....	14
Figure 4 Gamma Ray Detection System.....	17
Figure 5 Schematic of Nano Indenter Machine .....	31
Figure 6 Displacement Sensing System.....	33
Figure 7 Typical Load Displacement Curve.....	34
Figure 8 Berkovich Indenter .....	35
Figure 9 Dimensions of the Specimens .....	37
Figure 10 Ion Implantation Depth from a Non Smooth Surface .....	38
Figure 11 Ideal Ion Implantation Profile .....	42
Figure 12 TRIM's Calculated Degraded Ion Implanted Concentration Depth .....	43
Figure 13 Dose Depth Relation for a Non Degraded Beam into Silicon Nitride.....	44
Figure 14 Dose Depth Relation for a Non Degraded Beam into Stainless Steel .....	44
Figure 15 Cyclotron Beam 'Wings' on Scintillator Plate .....	47
Figure 16 Nano Indenter Specimen Holder .....	53
Figure 17 Master Menu of Nano Indenter Computer .....	54
Figure 18 Runs A, B and C on Silicon Nitride no 6 ( $10^{14}$ ions).....	56
Figure 19 Run D on Silicon Nitride no. 7 ( $10^{13}$ ions) .....	56
Figure 20 Run E on Silicon Nitride no. 10 (control specimen) .....	57
Figure 21 Runs F, G and H on stainless steel no.4 ( $10^{14}$ ions).....	58
Figure 22 Run I on Silicon Nitride no.7 ( $10^{13}$ ions) .....	58
Figure 23 Run K, L, and M on stainless steel no.2 ( $10^{13}$ ions).....	59
Figure 24 Run P on stainless steel no.1 ( $10^{12}$ ions).....	60
Figure 25 Run Q, R, and S on Silicon Nitride no.8 ( $10^{12}$ ions).....	60

	Page
Figure 26 Silicon Nitride no. 6 Detected Spectrum.....	62
Figure 27 Averaged Control Hardness of Silicon Nitride .....	64
Figure 28 Averaged Control Elastic Modulus of Silicon Nitride .....	65
Figure 29 Hardness of Silicon Nitride no.6 (Run B) .....	68
Figure 30 Elastic Modulus of Silicon Nitride no.6 (Run B).....	69
Figure 31 Hardness of Silicon Nitride no.6 (Run C) .....	71
Figure 32 Elastic Modulus of Silicon Nitride no.6 (Run C).....	72
Figure 33 Hardness of Silicon Nitride no.7 (Run D and I).....	73
Figure 34 Elastic Modulus of Silicon Nitride no.7, Run D and I .....	75
Figure 35 Hardness of Silicon Nitride no.8, Runs Q and R.....	77
Figure 36 Elastic Modulus of Silicon Nitride no.8 (Runs Q and R).....	78
Figure 37 Hardness for Stainless Steel control Runs H and M.....	80
Figure 38 Elastic Modulus for Stainless Steel Control Runs H and M .....	81
Figure 39 Hardness of Stainless Steel no.4, Run F and G .....	82
Figure 40 Elastic Modulus for Stainless Steel no.4 Run F and G .....	84
Figure 41 Hardness of Run K and L of Stainless Steel no.2.....	86
Figure 42 Elastic Modulus of Run K and L of Stainless Steel no.2 .....	87
Figure 43 Hardness of Run P on Stainless Steel no.1 .....	89
Figure 44 Elastic Modulus of Run P on Stainless Steel no.1 .....	90
Figure 45 Beam Incident on Magnified Specimen Contact Surfaces.....	92
Figure 46 Varying Ion Implantation Depth with Jagged Surface.....	93
Figure 47 Indentation of Deeper Implanted Regions.....	93
Figure 48 Oil Detection System.....	103
Figure 49 Exhaust Dilution System .....	106

# CHAPTER 1

## INTRODUCTION

### 1.1 Problem Statement

Inherent to any internal combustion engine is the matter of mechanical wearing of components subjected to high contact areas such as bearings and piston rings. Many techniques and much research has gone into the study of trying to reduce the wear of the engine components. Different materials affect the wear rates and patterns of a given mechanical system. Materials other than metals, like ceramics, are being studied to possibly help reduce the wear problem. Another area that is being focused upon is lubrication. In creating a lubricant which reduces the surface friction, the wear rate could be lowered. And of course, changes in the overall design to reduce the frictional surface area and still maintain dependability of the part would reduce the amount of wearing. Several factors external to the engine also have an effect on the wear rate. Owners maintenance, the driving techniques and frequency of use can change the rate of wear of engine parts.

There are several techniques available to measure the wear of a part in an engine. One technique to measure wear is to disassemble the engine and physically measure the dimensions of the part of interest. This tear down technique changes the subsequent wear pattern of the engine since exact reassembly is impossible. Another method is 'Part Dimensional Change' where a sensor is connected to the part which senses a change in dimension of the part. The 'Part Weight Change' method, is a technique used in which the part must be weighed on a sensitive scale and then put back into the engine. All of the above mentioned techniques depend on access to the engine and accuracy of measurement. The above also have the possibility of poor repeatability and reproducibility of data.

Another method of measuring mechanical wear is the Radioactive Tracer Method. This technique uses a in situ method of measuring the wear of a engine part while the engine is running. This method is very repeatable, able to make reproducible tests, and quick once the system is set up. The technique is able to evaluate transient wearing behavior, and can measure specific areas of a component. Wear measurements as small as one micron can be detected.

One type of radiotracer measurement technique is that of Surface Layer Activation (SLA) in which a heavy ion beam hits the individual engine part to be worn and caus-

es the nucleus of the atoms which make up the material to become unstable and thus release energy. One form of released energy is in the form of gamma rays. The now unstable atom is a radioactive ion. The detectable radioactive ions are worn away with the part's material and are detected in the engine's oil in a quantitative manner. The amount of material worn from the part is related to the amount of detected radioactivity.

SLA activates the surface of the part to be studied, so it depends on the nuclear properties of the elements that make up the part. Thus SLA is limited to those elements that can be transmuted into radioactive species with reasonably long half lives and easily identifiable radiation, usually elements having the atomic number greater than or equal to 24. The material limitation is currently quite extensive, e.g. chromium and iron, where p, d or He ion bombardment can produce an isotope with a detectable gamma ray. Hence material such as plastics, rubber and ceramics which are part of the wear scene and  $Z < 24$  can not be used in SLA technology. Furthermore this method has the capability of changing the wear patterns of the material since the material has undergone a change itself.

Ion Implantation is another radiotracer technique which uses the detection of radioactive ions. But instead of bombarding the target with a high energy, heavy ion cyclotron beam to change the atomic nature of the material, the beam merely implants ions into the surface, thus retaining the original atomic structure. This method can be used on any material, including ceramics and plastics, not just materials with the atomic number above 24.

Even though damage done by Ion Implantation is assumed to be considerably less than SLA (proposed by R.Ronningen [1]), the question still arises of does this method of testing change the material properties in any way? Our goal is to determine if the implantation of ions into the experimental specimens causes a material change. The implanting of radiotracer ions into a material is a physical one which takes a lot of energy and may create heat from the collisions. The amount of radiation damage incurred is primarily dependent on the ion energy, the ion dose, the target temperature, and the mass and chemical bonding of the target atoms. This overall method has the potential of causing damage to the implanted part. If sufficient damage occurs, the tribological properties of the target may change thus effecting the wear rate. If the implantation did effect the wear results then the experimental specimens would be considered to have a different microstructure than the original specimen. By implanting experimental specimens with varying amounts of ions and then comparing the specimen's wear rate and hardness against a control (non-implanted) specimen, we can

determine if there exists a possible threshold dose of ions implanted where the tribological properties are unaffected.

## 1.2 Literature Survey

Much research has been done on the effects of irradiation on ceramic materials. Most of this research has been performed by the materials community, while the automobile engineer merely uses the technique without knowing the potential problems associated with the method. Most of the following work was taken from the Engineered Materials Journals, where the research was plentiful.

Bhattacharya et al. [2] used optical microscopy, surface profilometry, Auger electron spectroscopy and a transmission electron microscopy to study the high energy ion irradiation effects on the surfaces of silicon carbide and hot pressed silicon nitride. Optical microscopy and surface profilometry revealed that 1 MeV  $\text{Ni}^+$  ion irradiation at a dose of  $1 \times 10^{16} \text{ cm}^{-2}$  produced swelling and roughness on both SiC and  $\text{Si}_3\text{N}_4$ . Auger electron spectroscopy in combination with sputtering revealed that the SiC surface became carbon rich, whereas the  $\text{Si}_3\text{N}_4$  surface became Si rich due to ion irradiation. Cross section TEM analysis of the surface layer of irradiated SiC showed that  $1 \mu\text{m}$  of material at the surface became amorphous due to irradiation with 1 MeV  $\text{Ni}^+$  at a dose of  $1 \times 10^{16} \text{ cm}^{-2}$ . Amorphization has also been observed in  $\text{Si}_3\text{N}_4$ .

Townsend [3] looked at the optical effects of ion implantation. Townsend stated that by the selection of ion energy and ion dose, one can inject trace impurities that control luminescence, generate absorption bands or complex defect aggregates, stimulate production of new crystalline phases or destroy crystallinity. Such property changes are valuable in diagnostic studies and indeed the high rates of energy deposition along an ion track allow production of defect clusters or excited states which are otherwise unattainable. Implantation invariably stimulated luminescence which provided a sensitive means of analysis to measure purity and near surface defect concentrations. Post implantation measurements revealed changes in many physical and chemical properties of the materials.

Burggraaf et al. [4] studied ion implantation and monolayer techniques for modifying ceramic surfaces. The authors suggested that thin surface layers with a thickness up to  $1 \mu\text{m}$  can be prepared within a ceramic matrix or on top of it. Concentration profiles of the dopant atoms were produced with different shapes while the structure was

crystalline or amorphous. Thin layers or complex layer structures were produced or thermodynamically stable solid solutions as well, from metastable compounds or composites. A variety of properties were changed, e.g., optical, electrical, mechanical, catalytic, and corrosive. Mono layer techniques were found to be especially interesting for modifying internal surfaces of porous materials and for changing chemical reactivity.

Cochran et al. [5] investigated the mechanical and structural properties of ion implanted yttria stabilized zirconia ceramics. The authors implanted yttria stabilized zirconia with 100KeV  $\text{Ca}^+$ ,  $\text{Al}^+$  and  $\text{O}_2^+$  ions at fluences of  $10^{15}$  to  $6 \times 10^{16}$  ions/cm<sup>2</sup>. Knoop microhardness with a shallow indenter penetration depth peaked at a dose of  $10^{16}$  ions/cm<sup>2</sup> for both  $\text{Al}^+$  and  $\text{O}_2^+$  but  $\text{Ca}^+$  produced no effect on microhardness. Vicker's microhardness with a much greater indenter penetration depth did not show detectable change by implantation but fracture toughness measurements from the same Vicker's indentations exhibited 10-23% increases at the highest  $\text{O}_2^+$  doses and 20-25% increases at high  $\text{Al}^+$  doses. Reflection electron diffraction showed that the surface had not been made amorphous by the  $6 \times 10^{16}$   $\text{Al}^+$  dose as a well crystallized diffraction pattern was obtained.

Oliver et al. [6] studied the hardness of ion implanted ceramics. The authors state that it has been established that the wear behavior of ceramic materials can be modified through ion implantation. Studies have been done to characterize the effect of implantation on the structure and composition of ceramic surfaces. To determine the effects of an ion implanted  $\text{Al}_2\text{O}_3$ , a commercially available ultra low load hardness tester was used to characterize  $\text{Al}_2\text{O}_3$  with different implanted species and doses. The hardness of the base material is compared with the highly damaged crystalline state and the amorphous material.

Even though much research has been done on the implantation damage of materials, the critical dosage required to produce a hardness change has not been accurately determined for automotive frictional materials. The current research finds the threshold ion dosage which causes material hardness elastic modulus changes. These property changes may cause the material to wear differently than the original material.

## CHAPTER 2

### FACILITIES AND SYSTEM COMPONENTS

#### 2.1 Wear Specimens

Ceramic and a metal materials were used as test specimens which are applicable to wear applications. The ceramic was a Silicon Nitride ( $\text{Si}_3\text{N}_4$ ) NC-132 supplied by Norton Corporation. This ceramic is often used in advanced engine wear research due to its hardness and stability under high temperatures. This ceramic is known to undergo amorphization during irradiation which could be detectable in changing material hardness or wear patterns [7]. The  $\text{Si}_3\text{Ni}_4$  components shown in Table 1.

Table 1  $\text{Si}_3\text{Ni}_4$  Components

Element	Max. wt %	Typical wt %
Mg	1.0	0.4-0.6
Al	0.5	0.18-0.3
Fe	0.75	0.16-0.35
Ca	0.05	0.006-0.03
Mn	-	0.05
B	-	0.003
W	3.0	1.5-2.0

Silicon and Nitride components make up the remaining weight percentage. NC-132 is a high strength, hot pressed ceramic that is considered to be the standard for

advanced ceramic materials. NC-132 retains its strength and oxidation resistance above useful temperature ranges of nickel-cobalt super alloys. NC-132 is characterized by high density, excellent thermal shock resistance, chemical inertness and high hardness. The Silicon Nitride is > 98% dense. NC-132 has the material properties shown in Table 2.

Table 2 Silicon Nitride Material Properties

	English	SI
Bulk Density	199/200 lbs/ft <sup>3</sup>	3.2/3.3 g/cc
Hardness, KHN <sub>100</sub>	2000	
Strength 3 pt. 20 C	140/160 x 10 <sup>3</sup> psi	990/1100 MPa
Fracture Toughness	4.9/6.0 x 10 <sup>3</sup> Lb-in <sup>-3/2</sup>	5.4/6.6 MNm <sup>-3/2</sup>
Creep Rate %/HR @ 1350 C, 20 ksi	0.1 / 0.007	
Young's Modulus, E	45 x 10 <sup>6</sup> psi	310 GPa
Thermal Expansion	1.9 x 10 <sup>-6</sup> /F	3.5 x 10 <sup>-6</sup> /C
Thermal Conductivity	220 BTU-in/hr-ft <sup>2</sup> -F	32 W/m K
Critical Quench T	1110 / 1300 F	600 / 700 C
Max. Use Temperature	2460 F	1350 C

The metallic specimen selected was Stainless Steel 17-4PH which originally contained mostly austenite. Grummon and Shalek [8] suggested that the metallic alloy be processed (heat treated and quenched) to produce a metastable structure (of 98% martensite) which could be a sensitive gage of radiation induced structural change induced by low dose irradiation. Since the phase was metastable, it could revert back to the austenite phase if sufficient kinetic energy was applied to the specimen. The typical properties of the 17-4PH are shown in Table 3.

Table 3 17-4PH Stainless Steel Components

Element	Wt. %
C	0.014
MN	0.61
SI	0.37
P	0.025
S	0.027
CR	15.15
NI	4.41
CU	3.46
CB+TA	0.19
N	0.019
MO	0.18

The element iron makes up the remaining weight percentage. The solution was treated by Shalek [8] at 1900 F (1040 C), held at temperature for a time commensurate with section thickness, and rapidly cooled as required to below 90 F (32 C).

Table 4 17-4PH Stainless Steel Properties

Yield Strength, (.20 PCT.) KSI	192.0
Tensile Strength, KSI	199.0
Elongation in 1.4 ins.,PCT	14.0
Reduction in area, PCT	48.0
Hardness, BHN	401
Hardness, HB	321

A review of literature indicates a threshold dose of  $1 \times 10^{16}$  ion/cm<sup>2</sup> for observable material property changes in irradiated metals.

## 2.2 Buehler Polisher / Grinder Machine

The Buehler Polisher/Grinder machine is used for planar grinding and polishing of test specimens. The system is electronically controlled from two front panels. The machine consists of a base containing an abrasive platen and a head which holds test specimens on a shaft. Three abrasive platens are used, two ceramic platens of varying hardness and a nylon platen for polishing. The shaft on to which a five specimen holding wheel is attached, rotates and is lowered onto the base platen. Both the head shaft and the platen rotate, in counter rotation to each other for best results suggested by Buehler. The rubbing of the specimen surfaces on the platen, mixed with abrasive solutions, causes the specimen material to be worn away. The system is controlled from a upper and lower control panel, in which specimen holder force on platen, rotation direction, duration, water lubrication and platen speed can be chosen. The platens are Metlap #6, Metlap #10 and a nylon platen. The higher the Metlap number, the harder the plate material. The abrasive solutions are a diamond suspension liquid whose varying diameter diamond particles are suspended in either a oil or water base for lubrication. For the final polishing stages, a MasterMet solution which contains no diamonds is used. The diamond size varies from a 45 $\mu$ m to 0.25 $\mu$ m diamond diameter. The larger diamond suspension is for removing specimen material while the smaller diamond suspension is for polishing. Diamond suspension is used for ceramic specimen preparation since it is harder than the ceramic specimen material

which we are using.

The specimen holder is a five piece holding wheel which holds 1.25 inch diameter specimens contained in mounting material. Normally the individual specimen mounts are made using an epoxy mix from Buehler called EPO-KWICK epoxy. The mixed hardener is poured on top of the specimen in a plastic cup and allowed to dry. While drying, the specimens are placed in a vacuum cell to remove any air trapped in the viscous epoxy.

Once hardened and at room temperature, the specimens are placed in the specimen holding wheel by use of a specimen mounting rig. This rig holds the specimen holding wheel firmly, approximately 0.125 inches from its base plate. When the specimen mounts are placed in the specimen holding wheel, the mounts fall to the base plate and are secured, thus resulting in five specimen mounts that are all equidistant from the holding wheel.

Once all the specimens are mounted into the holding wheel, the wheel is then placed on the polishing head where it 'floats', meaning that it can wobble thus conforming to any non flat platen surface. The appropriate settings are chosen for platen speed, force of the specimens on the platen, duration of run, etc. Once the machine is running, it must be manned and diamond suspension sprayed onto the surface approximately every 15 seconds. The machine will run until the time duration runs out or the session is cancelled.

### 2.3 Cyclotron

In order to implant ions into a target material, the National Super Conducting Cyclotron Laboratory (NSCL) at Michigan State University is used. The cyclotron implants ions into the specimen by use of a ion beam which is generated at its core and is transported down a beam line. The beam line is made of nuclei of atoms of virtually any single element. The nuclei are stripped of some of their electrons before entering the beam line. The collision of the beam with a target creates useful particles which are then implanted into the specimen. A group at Michigan State University which includes researchers from the College of Engineering and the NSCL are experimenting with possible useful beams concurrent with Ion Implantation Research [9].

In order to make use of the cyclotron accelerated beam, the target specimens must be placed at the end of the beam line and organized as needed. The components of interest lie at the end of the beam line in a vacuum sealed stainless steel pot. The experimental pot has a bolted flange for beam line connection, a windowed flange for

television monitoring, a top flange for access to the components and a bottom flange which held several movable shafts. All the flanges were lip type which use copper gaskets to seal off the vacuum. Pressure solenoids that moved the shafts were connected to the external portion of the bottom flange. Objects that were to be moved in and out of the beam were connected to the movable shafts, see Figure 1. The pressure solenoids were remotely operated from the cyclotron control room outside the radiation vault. The pot contained four items. The item that was first in the beam line was a stationary 0.125 x 0.625 inch slotted scintillator plate. The side facing the beam was painted with a material that scintillates when exposed to the cyclotron beam allowing the beam shape to be viewed. The slot only allowed a controlled portion of the larger beam to pass through.

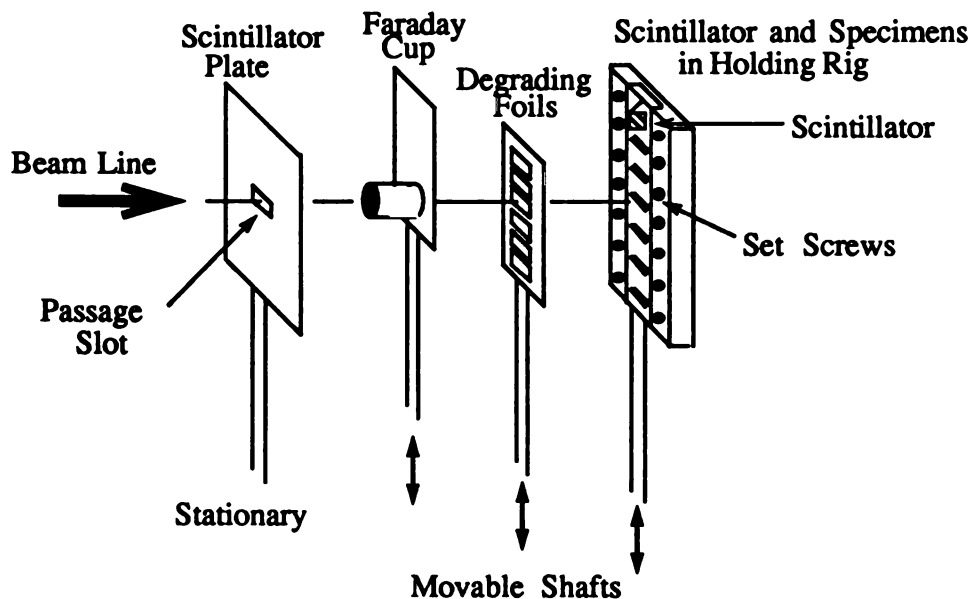


Figure 1 Target Pod Set Up

The second item in line is a Farady cup used to measure the beam current. This piece could be moved in and out of the beam line. The Faraday cup was connected to wires leading out of the pot and connected to a count meter in the control room. The third item was a movable piece that contained foil degraders of varying thick-

ness. The degraders are used for degrading the beam intensity before hitting the specimens. The last item was a rig that held six specimen mounts and one scintillator piece in order to view beam location.

## **2.4 Nuclear Radioisotopes**

The nucleus of an atom consist of  $N$  neutrons (no charge) and  $Z$  protons (positive charge), both of which are considered nucleons. The mass number ( $A$ ) of an element is the number of nucleons. The atomic number of an element is the number of protons ( $Z$ ). An isotope is a nuclei with the same number of protons and a different number of neutrons than the definition of the element. The stability of an isotope depends on the number of protons and neutrons in the nucleus.

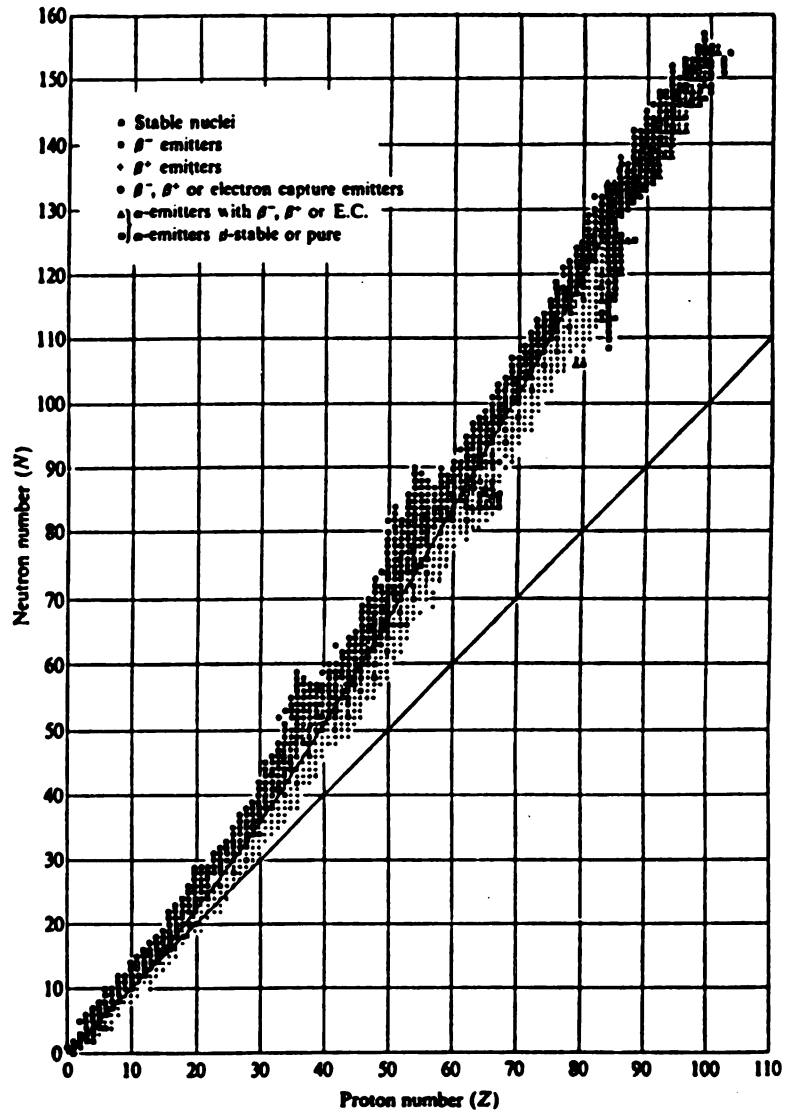


Figure 2 Stable Nuclei

Figure 2 shows the plot of the neutron number  $N$  versus the atomic number  $Z$  for all known nuclei. Each small square represents an isotope and the solid black squares represent stable isotopes. Two smooth curves, one through the stable isotopes and the other for  $N=Z$ , have been drawn. It is evident that for low values of  $N$  and  $A$ , the stable isotopes have  $N=Z$ . For heavier elements, the stability curve gradually departs from the  $N=Z$  line, reaching a slope of 1.6 for  $A=238$ . The isotopes on both sides of the curve are radioactive and eventually decay in such a way as to form the final stable isotopes.

The forces between the nuclei must be attractive, or there would be no stable nuclei because of the repulsive Coulomb force between the protons. Also, these attractive forces must be much stronger than the Coulomb repulsive forces, or there would be no stable heavy nuclei, because the Coulomb repulsion between the large number of protons would disrupt the heavy nuclei. The binding energy of the nucleus is decreased by the Coulomb repulsion of the protons in the nucleus. Because Coulomb forces are long range forces, each proton effects every other proton, not just its immediate neighbors. The repulsive force, therefore, goes on increasing with increasing  $Z$  and hence, with increasing  $A$ . This Coulomb repulsive force has two consequences, (1) The average binding energy per nucleon drops as  $A$  increases as seen in Figure 3 or (2) the locus of the stable nuclei should depart from the  $N=Z$  towards the direction of a higher number of neutrons, shown in Figure 2.

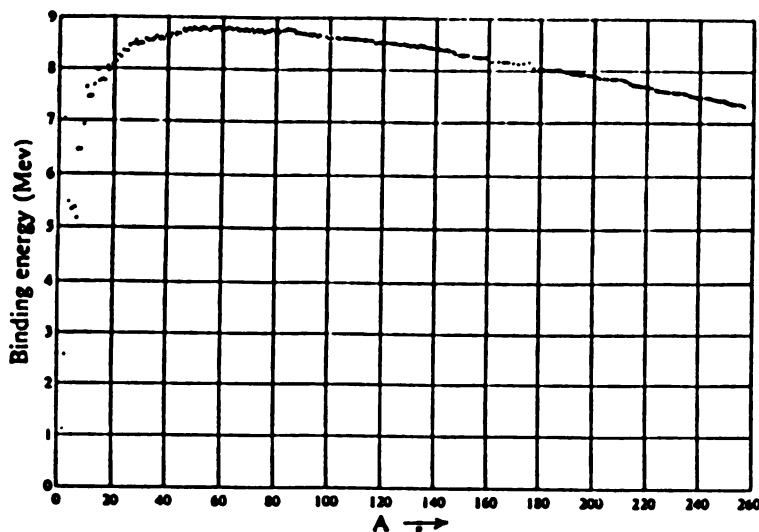


Figure 3 Binding Energy per Nucleon.

When an unstable nucleus decays, it emits an alpha particle, a beta particle, or a gamma ray. In the process, the original particle decays into another particle, and the element is called radioactive. Alpha particles have very weak penetrating power and can be stopped by a sheet of paper, but they can cause intense ionization in the gas through which they travel. Beta particles have less ionizing power but more penetrating power than alpha particles. Beta particles can easily pass through thin foils of metals a few millimeters thick. Gamma rays cause even less ionization but can penetrate through slabs of different materials many centimeters thick, including any engine block. Gamma rays carry no charge, thus they are not deflected by electric or magnetic field and they exhibit all the characteristics of electromagnetic waves. Gamma rays are used for the wear study in question.

When a nucleus emits a particle, it has essentially decayed, thus the radioactivity decreases. Experimental evidence shows that radioactive decay follows an exponential law. An expression used for the exponential decay is  $N = N_0 e^{-\lambda t}$  where  $N$  is the number of radioactive nuclei present at time 't'.  $N_0$  is the original number of radioactive nuclei present. The probability of decay per unit time  $= \lambda = \ln 2 /$  (half life of isotope). If an element has a half life of one day, then the element will contain one half of the number of radioactive nuclei in one day then it did to begin with. It is im-

possible to predict when a particular unstable nucleus will decay.

The activity of a radioactive specimen is defined as the number of disintegrations per second (dps) that occur in the specimen. A unit of activity used often is the curie which is equal to  $3.7 \times 10^{10}$  dps. Radioactive decay is a law of nature and conforms strictly to it. A given isotope always has the same half life and set of associated gamma ray energies, independent of how, when or where it was made. Each isotope gives off one or several gamma rays with specific energies. These gamma ray energies for all known isotopes are documented in such articles such as the 'Chart of Nuclides' [10]. As an example, the isotope  $^{54}\text{Mn}$  has only one gamma ray at the energy of 834.83 KeV. It also shows that  $^{54}\text{Mn}$  has a half life of 312.7 days and a branch ratio of 99.98.

## 2.5 Ion Implanting Depth Model (TRIM)

In order to estimate the penetration depth of energetic  $^{20}\text{Ne}$  ions into solid target specimens, an ion implantation depth model was used, known as TRIM (Transport of Ions in Matter) [11]. TRIM is primarily concerned with the quantitative evaluation of how the ions lose energy to the solid and the final distribution of these ions after they stop within the solid. Also considered are the first order effects on the atoms of the solid, particularly the electronic excitation of the atoms, the displacement of lattice atoms by energetic collisions and the production of plasmons and phonons in the solids by the passing ions. The ions may have energies from 10 eV to 2 GeV/amu. The program will accept complex targets made up of compound materials with up to three layers made up of different materials. It will calculate both the final distribution of the ions and also all kinetic phenomena associated with the ion's energy loss: target damage, ionization, and photon production. All target atom cascades in the target are followed in detail, and the redistribution of these target atoms is determined. TRIM only calculates the beam implantation for a monoenergetic beam. Computer simulations of the polyenergetic interacting beam are achieved by running several different monoenergetic beams of varying energies and nature and combining them into one file. Computer simulations of the polyenergetic beam are necessary to understand the overall interaction process. The TRIM simulation consists of following a large number of individual ion or particle histories in a target. Each history begins with a given energy, position, and direction. The particle is assumed to change direction as a result of binary nuclear collisions and move in straight free-flight paths

between collisions. The energy is reduced as a result of nuclear and electronic energy losses, and a history is terminated either when the energy drops below a pre-specified value or when the particle's position is outside the target. The target is considered amorphous with atoms at random locations, and thus the directional properties of the crystal lattice are ignored. The nuclear and electronic energy losses or stopping powers are assumed to be independent. Therefore, particles lose energy in discrete amounts in nuclear collision and lose energy continuously from electronic interactions.

TRIM helps to understand the physical results of ion implantation and to aid in the preparation of the properties test. The deposit of ions depends on the size and energy of the ions and the material of the target. Some combinations give sharp concentration peaks at a specific depth, where as others are more apt to be largely distributed. In any case a direct beam into a specimen will not give a uniform concentration of ions through some depth.

## 2.6 Gamma Ray Analysis System

The Gamma Ray Analysis System is used for detecting radioactive ions that emit gamma rays. The gamma ray analysis system contains four components: a gamma ray detection system, a pulse modification system, a liquid nitrogen system and a multichannel analyzing system. The purpose of the detection system is to detect gamma rays of various energies.

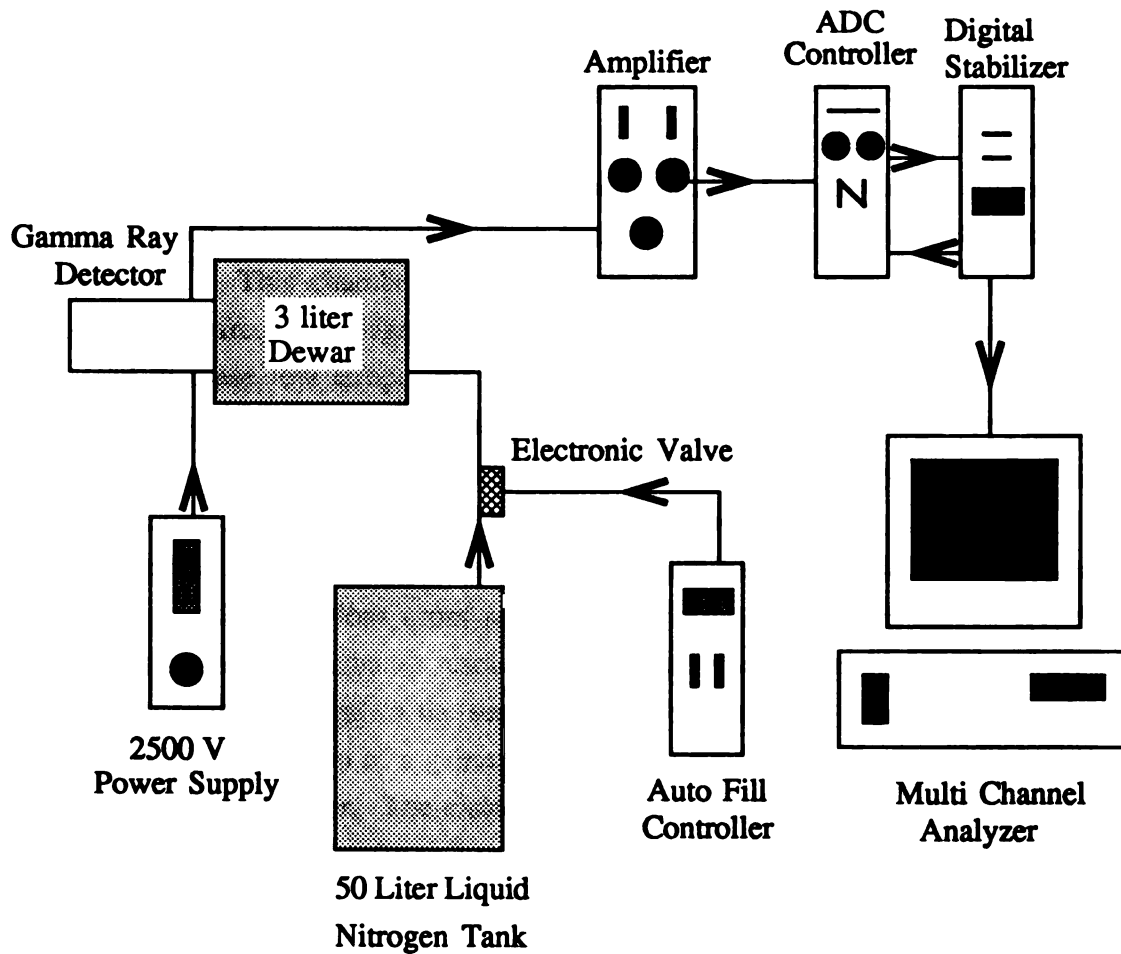


Figure 4 Gamma Ray Detection System

## **2.6.1 Gamma Ray Detection System**

The gamma detector contains four components; a semi-conductor gamma ray detector, a preamplifier, a cryostat/dewar system which maintains the detector element in a vacuum at cryostat temperatures and a liquid nitrogen dewar. The purpose of this system is to detect gamma rays and to produce a voltage peak proportional to the gamma ray's energy.

### **2.6.1.1 Gamma ray Detector and Accessories**

The gamma ray detector is a High-Purity Germanium coaxial photon detector, manufactured by EG&G Ortec, model number Gem 90220-P-Plus. The detector contains a single crystal of germanium 75.8mm in diameter and 92.9mm in length and is located in the center of the cylinder 3mm from the end cap of the detector. The crystal is located in the detector chamber which contains a vacuum and a 2500 volt electric field across it. This chamber is also kept at a temperature of -198.5 C to reduce 'noise' of radio frequency signals to the sensitive detection element. The detector is maintained at these low temperatures by having liquid nitrogen flow around it. The detection chamber needs approximately 24 hours to cool from ambient temperature in order to operate correctly. The GEM series detector uses a p-type material with a lithium diffused outer contact in the detection chamber. The closed end coaxial detector configuration blends the closed outer contact end into the outside cylinder surface, resulting in small absorptions cross sections. The low capacitance, closed end detectors have lower noise and better resolution. The purpose of the detector is to produce a voltage pulse proportional to the sensed gamma ray energy. Electron hole pairs are produced by the absorption of a gamma ray into the single crystal of germanium located in the detector chamber. The electron hole pairs are then swept across a 2500 volt electric field to oppositely charged contacts in the detection chamber. The electrons moving through the electric field produces an induced current. This current is then sent to the preamplifier.

A radioactive specimen holder was fabricated to hold one inch diameter thin calibrated specimen wafers. The holder is made of clear plastic and has 0.5 inch distance increments positions from the detector. The plastic holder slips over the end of the detector, open box end facing up ward. The solid calibrated specimen is placed in a 2.5 x 3.2 inch cardboard rectangle with a one inch hole in the middle for the specimen. When detecting a source, it is important that the source is in the same position

for every count test.

**Solid Angle** is a topic that is of concern when counting a specimen. Radioactive specimens give off gamma rays in every direction. If the detector were able to surround the entire specimen, as a sphere, then it could intercept every gamma ray being emitted. But the detector only sees a fraction of the gamma rays emitted and the geometric name for the cone of interception is called the solid angle. This angle is a fraction of the entire solid angle which is a sphere.

### **2.6.1.2 Preamplifier**

The preamplifier is a consealed sheath approximately the same diameter as the detector's outer sheath. The absorption of the gamma ray by the detector produces a current pulse at the preamplifier input. Each current pulse is integrated by the charge sensitive loop which is essentially a FET input operational amplifier with capacitive feedback. A feedback resistor R in parallel with the feedback capacitor C removes the charge stored by the input capacitance. This results in the exponential decay with time constant  $\tau = R \cdot C$ , of each charge loop pulse. The pole zero cancellation network differentiates the charge loop output to give a shorter decay time constant and is adjusted to eliminate pulse undershoot following differentiation. The preamplifier requires power of 24 volts which is supplied by the amplifier in the Pulse Modification System discussed later. The detector cryostat contains a temperature sensing element attached to the cooling path of the detector. The sensing element connects to a hybrid monitoring circuit which is incorporated into the preamplifier. An output cable from the preamplifier is connected to the remote shutdown input on the rear panel of the bias supply in the power box. The bias supply will reduce the detector's bias voltage to zero if the temperature resistance is greater than approximately 135 ohms. The monitoring circuit in the preamp provides this condition if the detector temperature becomes too high. Although no alarm is provided, the bias supply meter will indicate zero voltage and system noise will greatly increase after shutdown occurs. The automatic shutdown circuitry should be placed in operation before applying any bias to the detector. This is a critical safety device to prevent damage to the expensive detector.

### **2.6.1.3 Cryostat/Dewar System**

The cryostat/dewar system maintains the detector element in a high vacuum

at close to liquid nitrogen temperatures. The three liter dewar which is connected to the detector serves as a reservoir of liquid nitrogen while the cryostat provides a path for heat transfer from the detector element to the liquid nitrogen reservoir. Both the dewar and the cryostat rely upon a vacuum to insulate cold inner parts from the outer surfaces. The cryostat provides an outer envelope which can be maintained internally at high vacuum. The cryostat also contains a mount for the detector element and electrical components. Vacuum feed through in the cryostat allow electrical connections to be made from the detector to the preamp and high voltage filter. The cryostat contains a cryogenic vacuum pump that consists of one or more reservoirs of molecular sieve - a pelletized material with an extremely large surface to volume ratio which absorbs large volumes of gas when cooled to liquid nitrogen temperatures. This method of cryosorption pumping provides a good cryostat vacuum for continuous operation over a period of approximately five years. The three liter reservoir must be filled every 24 hours due to vaporization of the liquid nitrogen. The dewar is filled from a connection in the back of the container. This dewar is part of the liquid nitrogen system which has the sole purpose of providing liquid nitrogen to the cryostat to keep the detector element cool.

### **2.6.2. Pulse Modification System**

The Pulse Modification System's purpose is to take a rather crude input voltage pulse of given magnitude and convert it to a digital number which is proportional to the magnitude of the voltage pulse. To achieve this, the system requires three components: an amplifier, an analog to digital converter and a digital stabilizer.

#### **2.6.2.1 Amplifier**

The purpose of the amplifier is to create a well defined pulse from a poorly defined pulse from the preamplifier. The model 2020 amplifier's objective is to shape pulses, received from the detector preamplifier, into a near Gaussian shaped pulse so that there is consistency of shape entering the analog to digital controller.

Found on the front panel, the course and fine gain controls adjust the peak amplitude. By changing the amplitude, the relative energy associated with the incoming gamma ray will change, thus changing the energy at which the gamma ray appears on the resulting software screen. A super fine gain 22 turn adjustment screw is used for resolution better than 0.0063%. The polarity switch sets the model 2020 for the polar-

ity of the incoming preamplifier signal. The input polarity switch is always set to positive for this setup.

In the shaping section of the panel, the P/Z 22 turn adjustment screw optimizes the pole / zero setting which optimizes amplifier baseline recovery and overload performance for the preamplifier fall time constant. A correct pole / zero setting makes for a smooth pulse restoration to the baseline. The multiplier button multiplies the shaping time setting by 1 or 2. The shaping time knob selects the shaping time constant. This constant is somewhat proportional to the amount of time the amplifier spends on shaping the incoming pulse. The longer the shaping constant, the better resolved the peak but the slower the system, and vice-versa holds true.

The restorer rate in the restorer section is a two position toggle switch used to set the baseline restorer rate. In AUTO mode the baseline restorer rate is automatically optimized by internal circuitry as a function of unipolar output signal duty cycle and count rate. In HIGH mode the baseline restorer is fixed into a high rate. The high restorer rate can be used where a higher than normal restoration rate is required. The HIGH restorer rate is normally not used since there is a loss of resolution due to the increases correlated noise inherent in dc restoration. The restorer mode is a two position toggle switch that selects SYMmetrical or ASYMmetrical baseline restorer modes. In symmetrical mode, the restoration currents are identical for above and below the baseline. In asymmetrical mode, the restorer current above the baseline is much less than that below the baseline. The asymmetrical restorer mode offers superior high count rate performance for high resolution Ge spectroscopy and is used on this system. The symmetrical mode is used on Ge systems with low quality preamplifier, scintillation and proportional counting systems. The threshold auto/var switch is a two position toggle switch which is used to set the baseline restorer threshold. In auto mode, the baseline restorer threshold is automatically optimized by internal circuitry as a function of the unipolar output signal noise level. In variable mode, it provides a manually variable baseline threshold adjustment range of 0 to 200mV dc.

The pile up reject (PUR) switch is a two position switch that enables or disables the PUR / LTC (live time correction). Nuclear spectroscopy with high count rates can be made more accurate by testing for pulse pileup and rejecting contaminated pulses. Pulse pileup produces distortions in the higher ranges of the spectrum because successive shaped amplifier pulses tend to merge, and cause aberrations in the precise amplitude of any single pulse as measured by the analog to digital controller. Since many spectra have higher count rates at lower energies, the pileup of these

pulses strongly affects the less intense higher energy counts and can cause significant errors. A pileup reject circuit provides substantial improvement to the spectrum. The PUR DISC is for adjusting the PUR discriminator threshold level. The LED is a visual aid for setting the DISC threshold at an optimum level.

The BNC connectors at the bottom of the panel are for input and output connectors. The input (on left) accepts positive or negative preamplifier pulses and should be connected to the detector's preamplifier. The unipolar output is used in this setup and connects to the ADC. The unipolar output provides a positive, linear actively filtered near-Gaussian shaped pulses, amplitude linear to +10 volts.

On the back of the amplifier, there are three input/output connectors which are connected in parallel to the front panel connectors, meaning they are used for the same thing. The current setup uses the front panel. Also on the back there are DT (dead time) and PUR connections which should be connected to the corresponding connections on the ADC. There is a power outlet of 24v which should be connected to the power inlet of the detector's preamplifier.

### **2.6.2.2 Analog to Digital Converter (ADC)**

The analog to digital converter translates an incoming voltage to a digital number. The incoming voltage is proportional to the energy of the detected ion from the gamma detector. The ADC model 8077 incorporates a Wilkinson type, 450 MHz clock rate, counter/ramp converter optimized for high count rates, high resolution and low differential non-linearity performance.

The GAIN knob is a six position rotary switch used to select full scale resolution of the input signal. A selection of 512, 1024, 2048, 4096, 8196, or 16384 can be divided into the incoming 10v signal. The GAIN controls the ADC's resolution. A direct coupled input of 0 to +10v is digitized according to the front panel GAIN control into a binary code which corresponds to 512 through 16384 channels. Thus the incoming voltage is divided into a choose number of channels set by GAIN. The larger the number of channels selected, the higher the resolution but the longer it takes to process the data, thus increasing the dead time. As an example, with GAIN set to 8192 and no offset, the maximum conversion time is 18.7 $\mu$ sec. With the GAIN set to 512 and no offset, the maximum conversion time is 1.84 $\mu$ sec. The RANGE rotary switch is set equal to the size of the memory group assignment used in the multichannel analyzer's software. For instance, a memory assignment of 4096 channels in the software would require a range of 4096 channels on the ADC.

A LED is displayed on the front panel which shows the amount of dead time the system is encountering. Dead time occurs when there is an overload of incoming data. The ADC cannot keep up and the data is backlogged, thus resulting in a live counting time less than real time. The live counting time is stretched until all the data that was inputted could be processed. For example a system that has been counting for 60 seconds (real time) and has a high dead time may indicate a live count time of only 10 seconds. The PUR and LTC account for this overload and it is they who slow the live time down so that all the data can be processed. The LED displays the ADC's dead time in increments of 10%.

The front panel six offset toggle switches provide the suppression of digital zero. The offset is used to shift the given toggle switch channel number to zero in the multichannel analyzer's memory. With no offset (all switches down), the ADC's channel numbers are the same as the software's memory channel numbers. For example, if the GAIN is set to 8192 and the software's memory assignment is only 4096, an offset of zero will allow only the lower half of the full scale conversions to be stored, that is pulses up to five volts out of the possible 10v. If in this example, the offset were set to 4096 (the 4096 switch up), channel zero of the software memory would be shifted to correspond to channel 4096 of the ADC. This offset would allow the upper half of the full scale conversion, those above five volts, to be stored in the assigned software's memory.

The lower level discriminator (LLD) and the upper level discriminator (ULD) controls set the limits for the input signals to be accepted by the ADC for conversion. If an input falls within the selected window of channels (higher than the LLD but lower than the ULD setting) the input will be converted. If the input does not fall within the window, the input will not be converted. The window check is made at the conclusion of the linear gate time, an input pulse not within the window will add to the ADC's dead time, since it takes the time to check.

The zero control varies the zero intercept of the ADC conversion function so that the zero energy is stored in channel zero of memory. This zero setting is adjustable with a small screw driver and a pulser. A guide to setting this zero is found in the Canberra's "Fast Analog to Digital Converter Model 8077 Operator's Manual."

Peaks that are not well defined may be from noise or system interruptions. The peak detect function allows for some control over the chosen peaks. Peak Detect is a toggle switch used to select either automatic or delayed peak detection to start the ADC conversion. In auto mode, the linear gate, which allows a valid input pulse to be acquired, opens when the input rises above the input threshold. The input

threshold level tracks the LLD setting up to 0.1 volts max, therefore the input signal's baseline must be less than 0.1 volts for proper ADC operation. A high amplifier gain setting will raise the entire baseline over 0.1 and cause the system to overload thus resulting in a 100% dead time for the system.

The linear gate closes when the pulse falls below 90% of its peak amplitude. Wide pulses may make the automatic detection of the 90% point less certain. To overcome this uncertainty, the DELAYED peak feature may be used. This feature allows input pulses up to 100  $\mu$ sec wide to be converted. In this mode the linear gate closes at the end of the selected delay time. The delay time can be selected with the ADJ control while monitoring the INSP test point next to the ADJ control. The INSPect test point is provided to monitor the linear gate time.

The BNC connector on the front panel is used as the input from the amplifier. This accepts a positive unipolar or bipolar pulses for pulse height analysis (PHA) or specimen voltage analysis (SVA). In the current set up, the switch is set on PHA. The SVA is only for system testing. On the back panel, the PUR and DT connections should be connected to the corresponding connections on the back of the amplifier. The STAB connection is connected to the Digital Stabilizer and the DATA is connected to the IBM computer.

### **2.6.2.3 Digital Stabilizer**

The digital stabilizer stabilizes the ADC. When converting the analog signal to a digital number the ADC might not convert a 2.5v peak to the same number as it did 15 minutes earlier. The ADC wanders a little because it has no relative zero point. This wandering ADC causes the peaks on the computer screen to wander also since the peak's screen position is determined by the ADC. This wandering makes for repeatability very difficult. The Digital Stabilizer is designed to take care of the wandering ADC, it stabilizes the ADC by working in parallel with it. On the front panel, references may be entered to keep the output stable. A low energy peak channel number is entered for the 'zero' setting and a high energy peak channel number entered for the 'gain' setting. These two entered points make a reference for the ADC resulting in a stable peak. The two point stabilization can be turned to on, hold and off by toggle switches on the front panel of the digital stabilizer. When the switches are turned off, stabilization is disabled and the correction voltage is held to zero volts. When the switches are in the hold position, the correction voltage is not updated, but the last correction voltage is maintained at the output.

The % CORRECTION indicator is a ten segment LED bar graph, which indicates the percentage of full scale correction being applied in increments of twenty percent. The five digit display shows one of the four parameters for the Zero or Gain portion of stabilization. The four parameters are PEAK, WINDOW WIDTH, STABILIZATION RATE and ANALOG RANGE.

The Peak display indicates the peak channel which the stabilizer is correcting on. The Window width indicated the number of channels used by the stabilizer as its sampling range, with the window is centered about the peak. The Stabilization rate indicates the count rate of the input data which gives rise to a change in correction voltage. This display is in counts per second (CPS). The Analog Range indicates the value of the Analog Attenuation Factor. The attenuation is applied to the 5v range of the correction voltage from the Digital Stabilizer to the ADC.

### 2.6.3 Liquid Nitrogen System

The purpose of the liquid nitrogen system is to keep the detector element at close to liquid nitrogen temperatures. The liquid nitrogen ( $\text{LN}_2$ ) system has several components to achieve this task. A 50 liter self pressurizing liquid nitrogen tank is used as a large reservoir of  $\text{LN}_2$ . The 50 liter tank is connected to a three liter dewar which is fixed to the detector which was mentioned earlier. Every 24 hours the 50 liter tank automatically fills the dewar by the use of an auto fill controller. The dewar provides  $\text{LN}_2$  to the cryostat which is used as a path for heat transfer from the detector element to the dewar.

The 50 liter tank is manufactured by Cryofab and is insulated by a vacuum. Once filled, the tank must relief the nitrogen gas build up due to vaporization. A relief valve is located on the top of the tank and has been modified to be adjustable by simply screwing in the end piece for a higher tank pressure or screwing out to lower the pressure. The tank pressure should be kept at 3 to 5 psi. The relief valve will make a continuous hissing sound as it relieves the pressure build up. During normal operation the tank should be filled once every week at the cyclotron. The tank also has a special self pressurizing feature which creates large pressures from its own vaporization virtually instantaneously. This self pressurizing system is regulated by a black knobbed valve at the top of the tank. When high pressure is not needed, the valve should be closed, as is the case in the current set up. The tank also contains several safety features which should not be tampered with.

The dewar can be filled manually via a modified funnel or by the 50 liter tank which is the current set up. The dewar comes with a plug for the fill connection making the detector portable. The cryostat is an internal system which cannot be seen and needs no attention.

The auto fill controller is located in the power supply bin with the other electronic equipment. The purpose of the auto fill control is to fill the dewar every 24 hours from the tank of liquid nitrogen. The controller is a time based unit which counts down from 24 hours. When the timer runs out, a solenoid valve opens on the line between the dewar and the tank, permitting the tank to fill the dewar. A sensor located on the dewar's vapor vent line senses the presence of liquid nitrogen in the vapor line and causes the solenoid to close, thus filling stops. This sensor, consisting of a resistor in the flow of the vapor vent, is very sensitive. When the dewar is filling, the liquid nitrogen replaces the nitrogen vapor which exits out the vent line. When the dewar is full, liquid nitrogen will overflow the dewar and exit out the vent line, causing the resistor to cool and reach a certain resistance which triggers the auto fill controller to turn off the fill line solenoid. On the side of the controller, there is a resistance threshold adjustment screw which changes at what temperature the controller turns the filler solenoid off. If the sensor is not properly set, the controller will not fill the dewar all the way up, thus not keeping the detector cool and the detector might not power up (safety device). Also if the sensor is not set properly, the fill solenoid will never turn off and liquid nitrogen will flow out the vent line until the 50 liter tank is empty, so proper adjustment is required.

The time to next fill is displayed on the front panel of the Auto Fill Controller and can be changed by a row of dip switches accessible through the side panel of the controller. The system can be filled at any time by using the manual button on the front panel. When the system is filling the green light will be luminated. The system filling can be prevented by setting the NORM / INHIBIT toggle switch to inhibit. Place the switch in NORM mode for normal operation. A maximum fill time can be set by toggle switches on the side panel to prevent the system from overflowing. When this preset max fill time is reached, an alarm will sound and the fill time exceed light will luminate. The alarm can be reset by pressing the 'error' and 'reset' button simultaneously and the pressing the alarm 'reset' button. The solenoid toggle switch is for abiling and disabling the electronic fill solenoid. When set to off, the solenoid sill not open to let the passage of liquid nitrogen flow to the dewar. The power to the will solenoid is from a connection on the back cover of the auto fill controller. The vapor vent sensor is connected to the 'sense' connection.

## **2.6.4 Multichannel Analyzing System**

The purpose of the Multichannel Analyzing System (MCA) is to take digital data from the Pulse Modification System and to display it in graphical form on the computer screen. Once the data is in graphical form, it can be analyzed in different ways. The Canberra System 100 MCA is the system that is used to acquire the data, put it in graphical form and can be used to analyze the data. Another package called Canberra MicroSampo uses the data from the System 100 package to further analyze the data. Both of these packages are on the IBM model 70 computer.

### **2.6.4.1 System 100**

The System 100 is a software and hardware driven package. This system must be run in Microsoft Windows and requires 2MB of RAM, an DOS of 3.0 or later, EGA or VGA display and a hard disk. System 100 is the final stage of the detection system. The current pulse which originated from the detector was amplified, shaped and then converted into a digital number is then bused from the ADC to the System 100 board located on the mother board of the IBM model 70. The digital number corresponding to the analog voltage peak of varying height enters the software and is placed at a corresponding memory channel. The channel range is 4, 8 or 16 K which is chosen while entering the System 100 software package, and is also chosen on the ADC front panel discussed earlier. The larger the incoming digital number, the higher the corresponding channel number. Channels are displayed on the horizontal axis of the computer screen and the number of gamma rays detected are on the vertical axis. When a digital voltage peak enters the software, a count is added to its corresponding channel. A detected gamma ray is called a 'count', so 500 counts on channel 1500 refers to 500 gamma rays detected in memory location 1500. This displayed graph is the only screen of the System 100 software package. The main features used are discussed here.

The FILE function allows for saving and retrieving graphs that were made.

The ACQUIRE function that enables the computer to acquire the incoming data and display it on the screen. Duration of acquire can also be set under this function.

The DISPLAY function selects the portion of the memory channels to be displayed.

The **LEARN / EXECUTE** function saves and executes previous keyboard sequences for more automation of the program. This function saves of tedious repetition of keys.

The **ENERGY CALIBRATION** creates a mathematical relationship between the channel numbers and the actual gamma ray energies. Once an energy calibration is created and is turned on, the horizontal axis units are gamma ray energies instead of memory channels.

The **ANALYSIS** function analysis specific peaks that have been marked with a 'region of interest' (ROI). A ROI is placed on a peak by coloring the peak red using the shift and arrow keys.

#### **2.6.4.2 MicroSampo - Advanced Gamma Spectrum Analysis Software**

MicroSampo is a software driven system with a software key required for operation. The key is connected to the back serial port of the computer. This software package does not require Microsoft Windows nor does it require as much memory as System 100, but the software is not user friendly nor forgiving. MicroSampo includes automated energy, efficiency and shape calibration features. It does the peak search using generalized second differences and incorporates both linear and nonlinear peak fitting using precalibrated peak shapes thus providing very accurate peak energy and intensity information. It also does the nuclide identification and specific activity calculation using the least-squares solutions for overlapping peaks and nuclides. MicroSampo is currently used for the analysis of specific isotope specimens for the calibration of the entire detection system. Once the detection system is operating correctly, a detection calibration is performed so that an efficiency graph of the system is created for the set up. Using this calibration, unknown isotopes can be identified..

MicroSampo can not acquire data thus it must retrieve a saved file created by the System 100 software. MicroSampo has several functions which all must be used in order to get results. The functions are as follows.

**FILE** - allows for the filing of System 100 and MicroSampo files.

**SPECTRUM DISPLAY** - displays the retrieved spectrum.

**PEAK SEARCH** - finds and displays the peaks of set significance.

**PEAK FITTING** - fits a mathematical curve to the shape of the peak.

**PEAK SHAPING** - fits an calculated smooth area under the peak curve.

**DETECTOR EFFICIENCY CALIBRATION** - uses above data to determine overall detector efficiency.

Although of limited use in this study, the gamma ray detector will become an integral part of the piston ring wear measurement system as described in the appendix.

## **2.7 Nano- Indentation Machine**

The nano-indentation machine is used to measure the hardness of materials [12]. This machine can detect very slight changes in hardness, for instance due to radiation damage. This machine is located in the High Temperature Materials Laboratory (HTML) of the Oak Ridge National Laboratory in Oak Ridge Tennessee. This lab is part of the Department of Energy (DOE) and is currently operated by Martin Marietta Energy Systems, Inc. It is designed to help solve material problems that now limit the efficiency and reliability of advanced energy conversion systems. Cooperation with the U.S. industry is the particular focus of the HTML. The Mechanical Properties Microprobe or the Nano Indenter is a special microhardness tester capable of operating at loads in the microgram range. The instrument consists of three major components: 1) the indenter, 2) an optical microscope, and 3) a precision table that transports the specimen between the microscope and the indenter. Unlike conventional hardness testers, it is not necessary to determine optically the area of an indent in order to calculate the hardness. Instead, the position of the indenter relative to the surface of the specimen is constantly monitored, thus allowing the depth of an indent to be determined. The area of the indent is then calculated from a knowledge of the geometry of the tip of the diamond indenter. The fact that the position of the indenter can be determined to within 0.2nm means that the indenter can be used to sample very small volumes of material. Typical applications include the characterization of thin films, near surface properties, and the different phases in a multiphase material. The instrument is also useful in studies of composite materials and in the de-

termination of interfacial strengths.

The Nano Indenter is essentially a load controlled system. However, a wide variety of indentation parameters may be prescribed, and through the use of feedback techniques, displacement controlled experiments may also be performed. Under both load control and displacement control conditions, load and displacement are measured continuously so that hardness can be determined as a function of indent depth on the basis of a single indent.

The indenter consists of a rod attached at its center to the middle of a special three-plate capacitive sensor. Movement of the capacitor plate is used to produce the displacement of the indenter. The total movement possible is 100  $\mu\text{m}$ . The depth resolution of the system is approximately 0.2 nm. At the bottom of the indenter rod is a three sided diamond pyramid ground so that the sides of the pyramid make an angle of 65.3 degrees with the normal to the base. Thus the indents appear as equilateral triangles, and the length of a side of an indent is approximately 7.4 times its depth. The depth of an indent is related to the diameter of the circle that circumscribes the triangle the indent makes on a surface by the expression :

$$h = 0.113d$$

where  $h$  is the depth of the indent and  $d$  is the diameter of the circumscribed circle.

A coil is attached to the top of the indenter rod and is held in a magnetic field, thus passage of a current through the coil can be used to apply a force to the indenter. There are two load ranges, 0 to 120 mN (0 to 12 grams) and 0 to 20 mN (0 to 2 gm). The load resolution for the more sensitive range is approximately within 0.2  $\mu\text{N}$ . The gross vertical position of the entire indenter head is controlled by a motorized micrometer, referred to as the Z motor. The Z motor may be operated from the console or by a manual control box.

The position of an indent on a specimen is selected using the optical microscope that is built into the system. A TV camera mounted atop the microscope permits the image of the specimen to be viewed remotely. The microscope has three turret-mounted objective lenses that in combination with the eye piece and additional magnification produced by the TV camera provide magnifications of 130, 270 and 2000 X on the TV screen. Both turret rotation and focussing are done remotely from the computer console.

The system used to apply the load to the indenter consists of a magnet and coil in the indentation head and a high precision current source, shown in Figure 5.

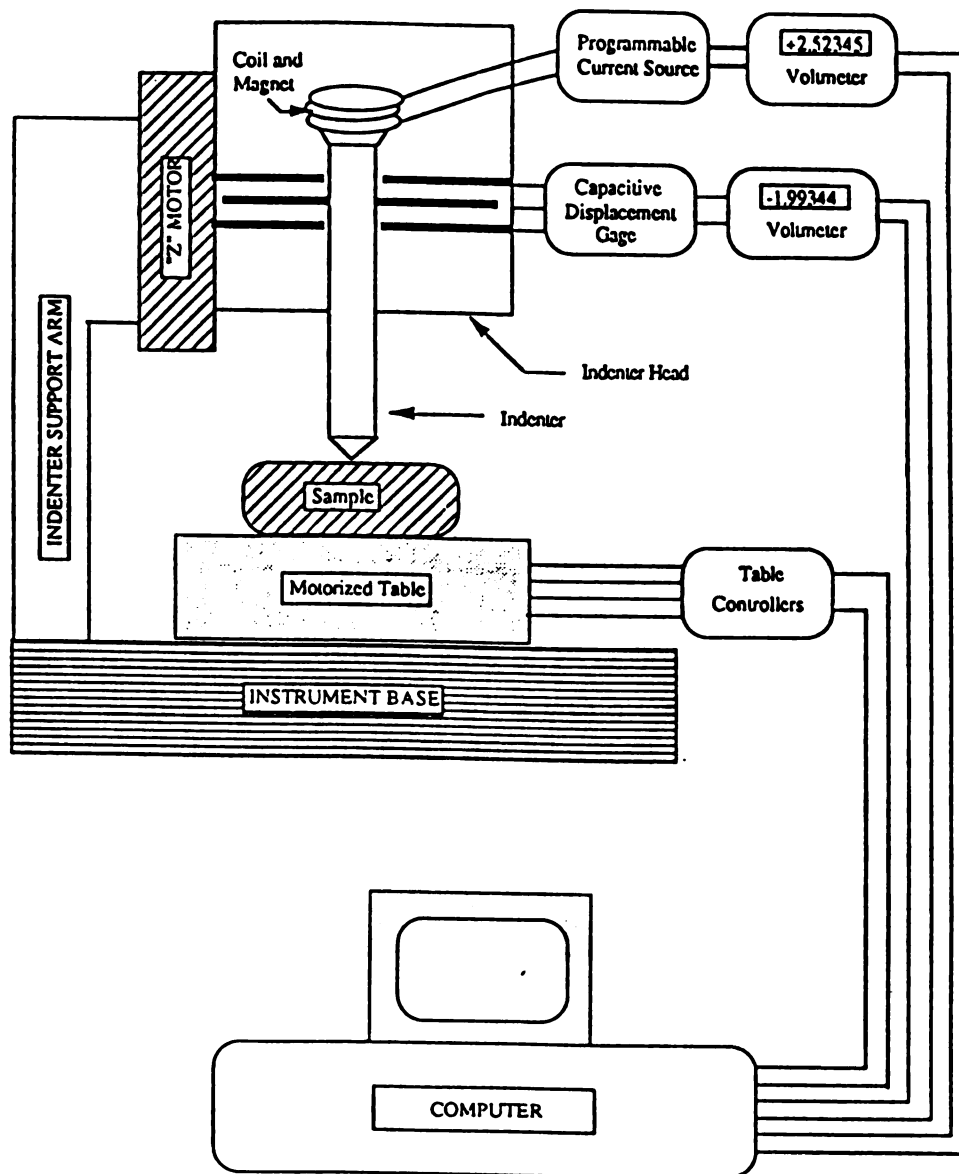


Figure 5 Schematic of Nano Indenter Machine [11]

The current source is applied across a coil in a magnetic field, thus generating a force. The current from the source, after passing through the coil, passes through a precision resistor across which the voltage is measured. It is this voltage that is dis-

played on the displacement voltmeter. The current source is programmable with a resulting range of displayed voltage of -2.0 to +2.0 volts in the high load range and from +0.8 to +1.7 in the low range. The voltage is controlled through a 16 bit DAC, therefore the maximum resolution is  $10\mu\text{V}$ .

The displacement sensing system is the most important part of the Nano Indenter system. It is shown in Figure 6 and consists of a special three-plate capacitive sensor. All three plates are circular disks approximately 1.5mm thick. The two outer plates have a diameter of 50 mm, and the inner moving plate is half that size. All three plates have a hole in their centers large enough to accommodate the indenter column, which is actually attached to the moving plate. This plate and indenter assembly is supported by two leaf springs cut in such a fashion as to have very low stiffness. At the top of the indenter column is a load coil that is used to raise and lower the plate and indenter assembly through its  $100\mu\text{m}$  of travel between the outer plates of the capacitor. This same coil applies the force required to make an indent.

The x-y tables have a real resolution of  $0.1\ \mu\text{m}$ . The motor controller can be controlled by the computer. The screws have a pitch of 40 threads per inch. They have a real accuracy of 20 millionths of an inch per inch and are mounted on bearings with a maximum of 15 millionths of an inch horizontal play. Although the backlash in the stage is virtually nonexistent due to special zero backlash nuts on the screws, it is recommended that each position be approached from the same X and Y directions. The stepping motors have a 50,000 steps per revolution. The motors must be de-energized between moves to prevent excessive heating during the experiment, which leads to thermal drift in the displacement measurement.

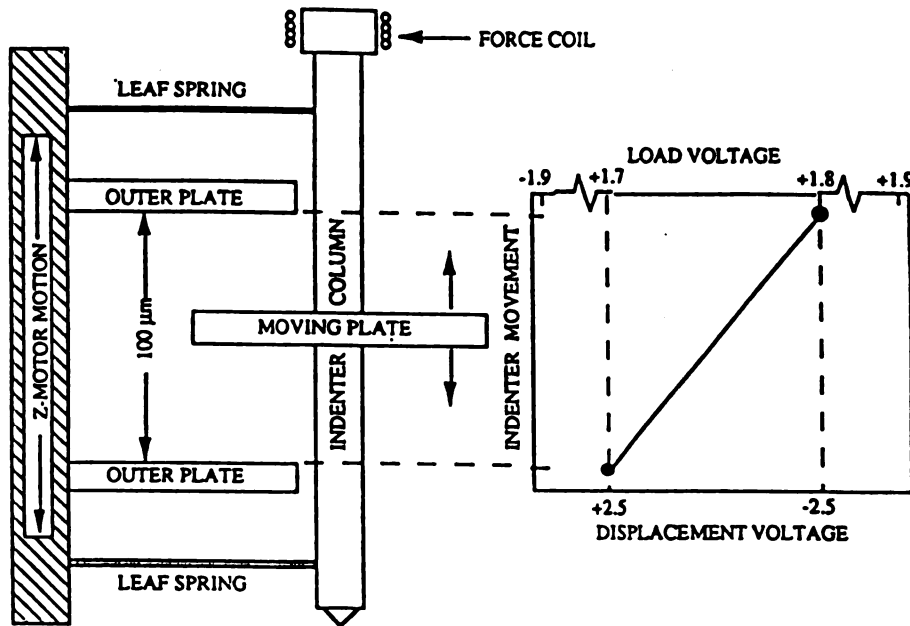


Figure 6 Displacement Sensing System [11]

In the microprobe's most sensitive mode, it operates with loads in the microgram range, although a maximum load of 10 grams is possible. Indent dimensions are not measured directly but are calculated from measurements of the position of the indenter relative to the surface of the specimen and a knowledge of the geometry of the point of the diamond indenter. Sophisticated capacitance techniques are used to measure the position of the indenter relative to the surface with an accuracy of 0.2 nm. Thus very small volumes of material can be studied, and the strength of a material can be characterized on an extremely localized scale. Motion of the specimen stage in the x-y plane is also precisely controlled. The indenter can be positioned within  $1.0\ \mu\text{m}$  of any chosen point on the specimen, and a series of indents, separated by steps as small as  $0.1\ \mu\text{m}$ , may be made in any geometrical pattern. The entire operation of the system is computer controlled, and one or several of indents may be specified and carried out without further operator intervention. The closest indent to the edge possible with this machine is  $4\ \mu\text{m}$ .

Because the indenter penetration is usually only a few nanometers deep, nano indentation test are sensitive to the near surface features on the specimen. They are also very sensitive to microstructural discontinuities such as grain boundaries, twin boundaries, porosity and precipitates which have dimensions comparable to that of the indenter tip's incursion. With this in mind, localized microstructural effects, which might be averaged out below a larger indentation, can have a major effect on hardness number. Because nano indentations specimen only a shallow portion of the specimen surface, the response is greatly influenced by the quality of the specimen preparation. Note that it is possible to obtain a high polish on a surface, yet still retain the remnants of previous course grinding steps.

Load displacement (L-D) hardness testing is what is used in the nano indenter. L-D tests have several features which allow more information to be obtained than from residual impression measurement methods alone. By monitoring the displacement continuously, a curve is produced such as that shown in Figure 7.

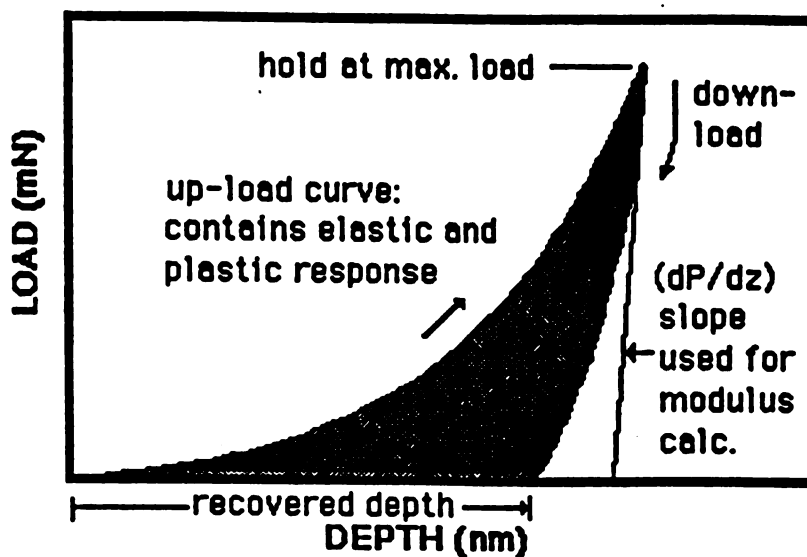


Figure 7 Typical Load Displacement Curve [11]

The curve consists of an upload portion, a hold at peak load, and an unloading portion. The displacement information from the tip load portion contains both elastic and plastic components so that the instantaneous hardness values computed from the up load curve without elastic corrections would tend to appear somewhat lower than values obtained from elastically recovered residual impressions made to the same depth. The unloading curve indicates the elastic behavior of the specimen, and its slope can be used to correct the instantaneous hardness number from the up load portion of the L-D curve to compensate for elastic effects.

Not only elastic corrections can be obtained from the unload portion of the L-D test results, the modulus of elasticity of the surface can also be obtained. This calculation involves assumptions about the indenter geometry, and involves the depth of the indenter at maximum load and at the elastically relaxed condition.

The nano indenter uses a newer, ultra precision L-D instrument known as the Berkovich indenter. This indenter is pyramidal shaped with an equilateral triangular base, shown in Figure 8.

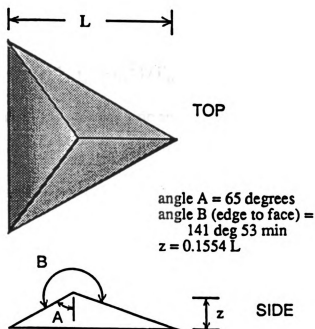


Figure 8 Berkovich Indenter.

The major advantage of this indenter for precision work is that it is much easier to get a sharp point with only three sides meeting than with four sides. This method can give hardness numbers just as Vickers and Knoop indenters can. The geometry of the Berkovich indenter is as follows:

$$\text{Surface area } S = 0.637 L^2$$

$$\text{Projected base area } A = 0.5774 L^2$$

$$\text{Hardness Number } H_B = 1570 (P / L^2)$$

where  $L$  is the altitude of the triangular base of the pyramid.

The elastic modulus is calculated from  $dz/dP$  shown in Figure 8.

$$(dz/dP) = (1/2 z_p)(\pi / 24.5)^{0.5} (1 / E_r)$$

where  $z_p$  is the plastic depth, and  $E_r$  is the composite elastic modulus of specimen and indenter.

$$1/E_r = (1-v^2) / E + (1-v_o^2) / E_o$$

$E$  is Young's modulus,  $v$  is Poisson's ratio and the subscript 'o' refers to the indenter.

## CHAPTER 3

### PREPARATION AND PROCEDURES

#### 3.1 Specimen Preparation

Both of the ceramic and stainless steel specimen were made to the dimensions indicated.

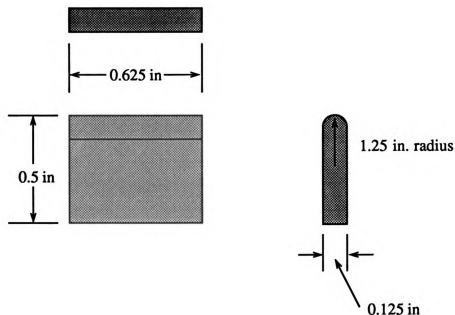


Figure 9 Dimensions of the Specimens

The ceramic specimens were manufactured to size and a surface finish of 16 microinches on the radiused portion by Norton Corporation. Fifty specimens were purchased at \$110.00 dollars a piece. The stainless steel was machined at Michigan State University from a two inch diameter hardened steel rod. The rod was cut into wafers over 1/8 inch thick, then each wafer was cut into four approximately 1/2 x 5/8 inch rectangles. The piece was then surface ground to finish with the exception of the soon to be radiused side. A special tool was built to put the radius on the pieces. The tool was cylindrical with four slots cut into the outside of the cylinder. This tool is set in a lathe with a specimen tightened down in each of its four slots. The diame-

ter was 2.50 inches which when exposed to a grinding wheel put a 1.25 inch radius on the steel.

Now all of the specimens had to be prepared in an appropriated manner for the cyclotron run. Two types of implanted specimens were desired for the cyclotron run. One experiment was to implant the entire 5/8 inch long curved surface with ions, meaning that the curved side must be exposed to the beam. Only the ceramic specimens were to be used for this experiment and the manufactured 16 microinches curved surface finish was adequate for this experiment. These specimens will be subjected to a wear test not covered at this time. A well polished surface was essential for good implantation results. The cyclotron would penetrate a set distance for a given material and beam. If the surface was not polished, peaks and crevices would be apparent and the ions would deposit at a set distance into the material from the non smooth surface, thus giving an implantation depth matching the surface profile. Note also that the angle of incidence affects the implantation profile.

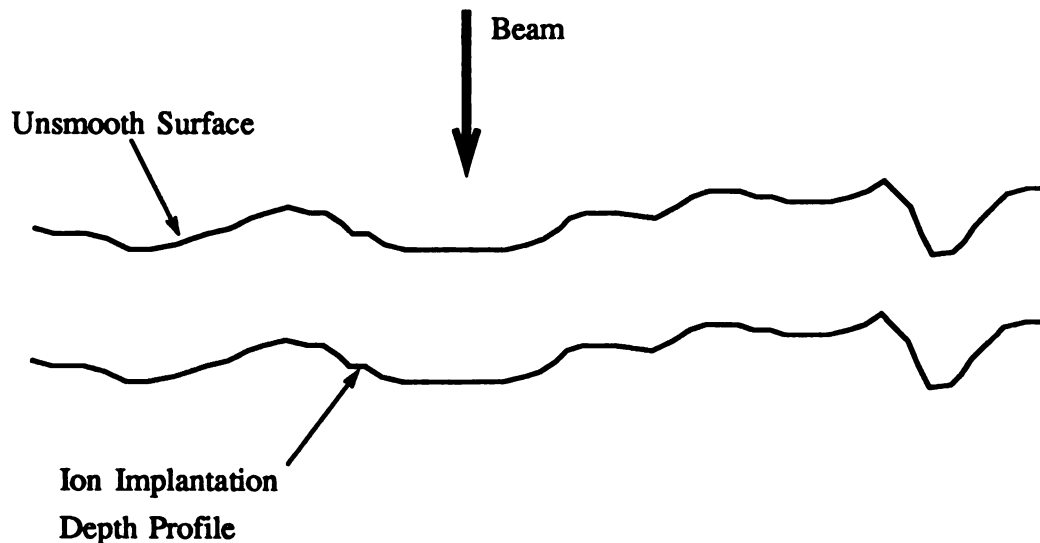


Figure 10 Ion Implantation Depth into a Non Smooth Surface.

The other experiment was the implantation of ions into the large 1/2 x 5/8 surface of the specimen. The specimens would be subjected to a nano-indenter to test the hardness of the material where the beam hit. The cyclotron beam implants ions in

a peak at a set depth into the specimen, so if the specimens were bombarded, the change in properties (if any) would occur not on the surface, but several microns into the surface, resulting in being invisible to the surface testing nano-indenting machine. So it was decided to place two highly polished specimens together with the large faces together and then sending the beam into the intersection of the two. This 'doubling up' would cause the damage to occur on the inside surfaces of each specimen. The radiused portion of the specimens would not be used in this experiment. This experiment would be run for both the silicon nitride and the stainless steel.

As stated before, the ceramic specimens which were to be implanted along the full radiused portion, needed no further polishing, unlike the double type specimens. The specimen mating surfaces should be as smooth as possible so that the double piece seemed as a continuous material to the beam. In order to achieve this, the specimens were first set with the large surface facing down in a Buehler fast curing epoxy and then placed in the five specimen holding device for the planing and polishing stage. Even though the specimens were manufactured to a tolerance less than 0.0005 inch, the specimens were not all perfectly planar so grinding must be done to achieve planar specimens. After the abrasive planing stage was done, the specimens were then polished. The surface preparation procedure for the Silicon Nitride is shown in Table 5.

**Table 5 Surface Preparation Procedure for Silicon Nitride**

	Surface	Abrasive diamond suspension	Time	Force	Speed
<b>Planar Grinding</b>					
Stage	Metlap 10	45 $\mu\text{m}$	5 min	5 lbf/specimen	240 rpm
<b>Specimen Integrity</b>					
Stage	Nylon Texmet	6 $\mu\text{m}$	7 min	5 lbf/specimen	50 rpm
<b>Final Polishing</b>					
Stage	Nylon Texmet	1 $\mu\text{m}$	10 min	10 lbf/specimen	240 rpm

This procedure left a mirror like finish on the flat silicon nitride specimens. Since the Metlap 10 platen was approximately the same hardness as the specimens, after about one hour of grinding and polishing, the platen became 'dished'. The platen was then be reflatened by using the Buehler Platen Dressing Kit. This kit contained a flat platen which connects to the Buehler head and several different sand paper grits which removes all the high spots and eventually flattened the once dished Metlap platen.

The procedure for grinding / polishing the stainless steel is similar, but the time and forces are reduced from the ceramic procedure since it is must softer than the ceramic.

**Table 6 Surface Preparation Procedure for Stainless Steel**

Stage	Surface	Diamond Suspension	Time	Force	Speed
Planar Grinding	Metlap 10	30 $\mu\text{m}$	3 min	5 lbf/specimen	240rpm
Specimen Integrity	Nylon Texmet	6 $\mu\text{m}$	3 min	5 lbf/specimen	240 rpm
Polishing	Nylon Texmet	1 $\mu\text{m}$	3 min	5 lbf/specimen	240 rpm
	Nylon Texmet	MasterMet	3 min	5 lbf/specimen	240 rpm

Once the large sides of the ceramic and stainless steels were polished, the specimens were taken out of the epoxy mounts. The flat ends opposite the curve needed to be polished. All the specimens were mounted in another specimen mount. These mounts were to be used to hold the specimens while being polished and also to hold the specimens in the cyclotron holding pot while the specimens were being implanted with ions. The new mounts were made of copper and were 1.25 inches in diameter, one inch tall with one inch flats on both sides. The one inch flats were for positioning the specimens in the cyclotron holder. A slit was milled in the center so that the specimens would slide into the slit and be held by two set screws. The slot was milled 0.03 inches shy of the 1/2 inch deep specimens so that the specimens would

protrude from the soft copper thus keeping the copper from being touched when the specimens were polished. There were two types of copper holders that were made, one which held one specimen and another type which held two specimens. The single specimen holder exposed a single specimen radius which was to be hit by a multiply degraded cyclotron beam for the wear test rig. The double specimen piece held two highly polished surfaces together with the non-radiused end exposed. The cyclotron beam was to penetrate a spot between the specimens and deposit ions on the inner surface of the specimens. After implantation, the specimens would be separated and the inner ion implanted face tested for a change in hardness.

Each copper specimen holder had two allen screws to hold the specimens in place. The allen screws were machined flat so that a good flat surface contact was made between the set screw and the specimens. A set screw with a burr could damage the specimens or even break them. The specimen holders were made of copper which has the best conductivity of any pure metal. Any heat generated by the beam hitting the specimen would be absorbed into the copper away from the specimens. The specimens with the radiused edge exposed were mounted in the single spaced copper specimen holders and set aside since they were ready for implantation. The highly polished sides were placed together and placed in the double spaced copper holders with the flat ends exposed outward. These ends of these specimens were then ground flat and then polished following the procedures listed above. The specimens were polished so that the crack between the two specimens could not be seen with the human eye, so that the two pieces seemed as one. All the specimens were now ready for implantation.

### 3.2 TRIM

A uniform dose depth profile was desired for the single specimens that were to be implanted on the radius, shown in Figure 11.

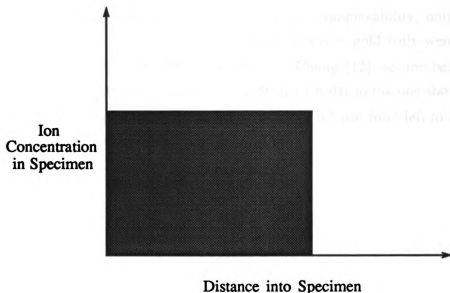


Figure 11 Ideal Ion Implantation Profile

In order to achieve a uniform profile, degraders must be used which degrade the beam energy before hitting the specimen. In degrading the beam, the ions will be deposited at a shallower depth. The thicker the degrader, the shallower the implant. If the degraders, of varying thicknesses are placed in succession in the beam line, then the ion concentration profile will be a number of concentration peaks which are a step in the direction of a uniform concentration profile. Since we are looking for a change in hardness of the material at the implanted locations, we would like the ions to be implanted at a uniform profile up to a set depth. This would show a consistent wear rate through the implanted region, whether it was different from the non-implanted portion or not.

Since the beam deposits ions at a set depth in a peak form, a combination of varying thickness degraders were needed to give a somewhat uniform profile. Inexpensive, quick tests by TRIM enables us to determine the correct foil material and foil thickness for our use. Gold and Nickel foils were chosen due to their dense material and beam degrading ability. Gold seemed to be easiest to sputter into thin foils, so gold was chosen. The preparation of the gold foils was done by Grummon and Shalek [7]. The ion implantation depth desired was 4.5  $\mu\text{m}$  which was deep enough to pro-

vide some wear time but again shallow enough so that the hard slow wearing ceramic would not take too long. Due to size constraints and complexability, only six foils were choose to be used, meaning that six varying thickness gold foils were to make peaks for 0 to 4.5 $\mu\text{m}$  deep. The TRIM operator, Y. Chung [12], set the beam energy variable to 2.5 Mev / nulceon and TRIM gave a profile similar to the one shown in Figure 12. The peaks corresponded to 9.0, 8.5, 8.0, 7.5, 7.0, 6.5  $\mu\text{m}$  from left to right. The deepest peak corresponding to the thinnest foil.

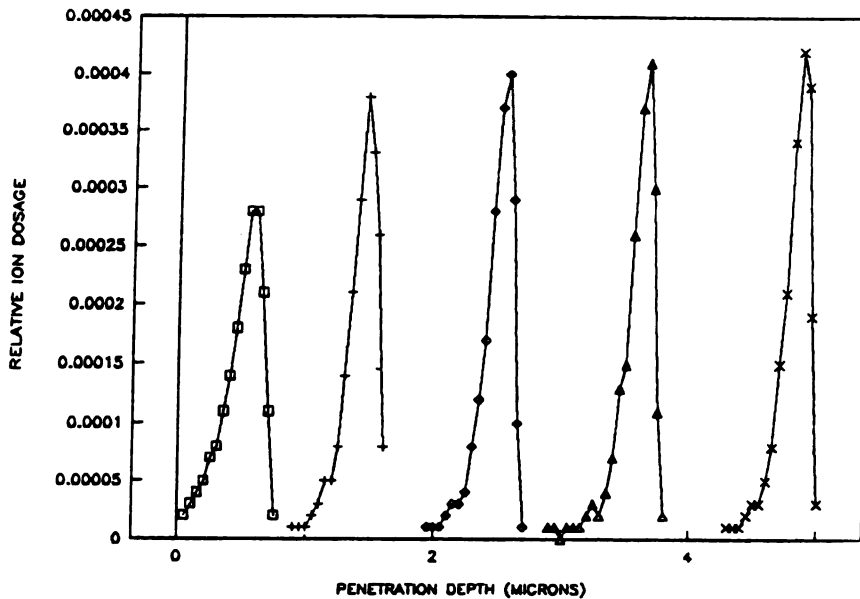


Figure 12 TRIM's Calculated Degraded Ion Implanted Concentration Depth.

For the nano indenter run, we needed to know the distance into the specimen where the maximum concentration of ions would occur. For a non degraded neon beam of 2.5 Mev / nulceon into Silicon Nitride, TRIM gave the profile shown in Figure 13. The peak ion concentration was found at 17.8  $\mu\text{m}$  into the silicon nitride.

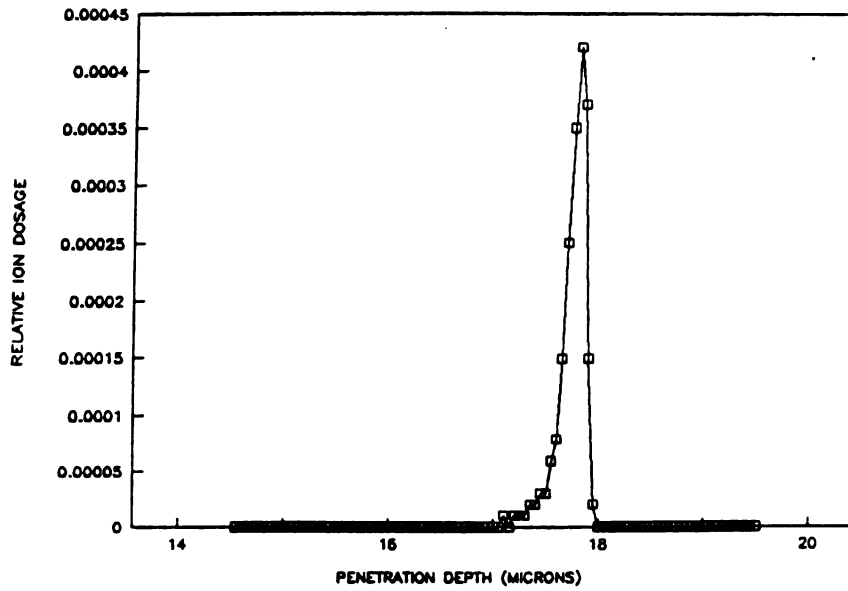


Figure 13 Dose Depth Relation for a Non Degraded Beam into Silicon Nitride.

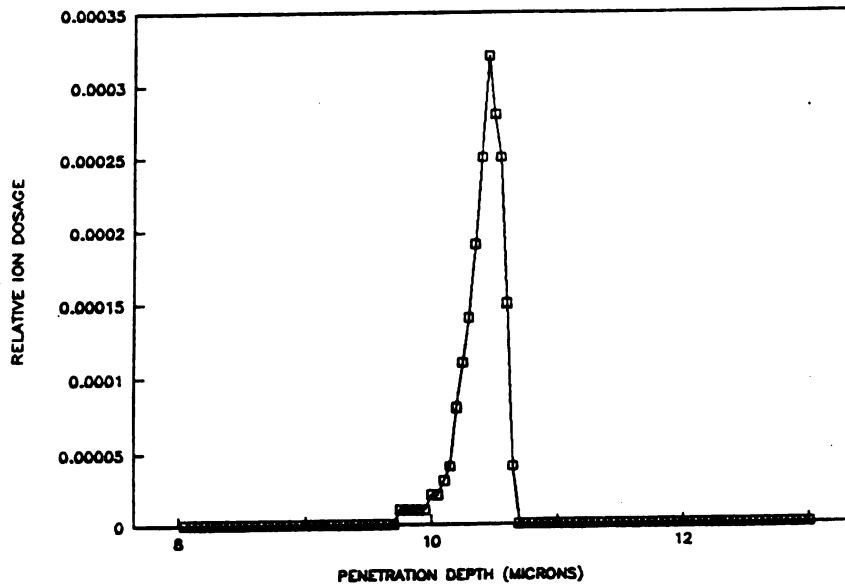


Figure 14 Dose Depth Relation for a Non Degraded Beam into Stainless Steel.

Likewise the same procedure was run for the stainless steel. TRIM gave the profile shown in Figure 15. The peak ion concentration was found at 10.5  $\mu\text{m}$  into the stainless steel.

### 3.3 Cyclotron Ion Implantation

Ideally it was desired to achieve an ion implantation concentration of non-radioactive ions which would be similar to an implanted radioactive ion implantation. An implantation using an equivalent of  $2 \times 10^{13}$  ions/cm<sup>2</sup> of <sup>22</sup>Na would yield the following radioactivity:

$$^{22}\text{Na} : T_{1/2} = 950.4 \text{ days} , \text{ branch ratio} = 99.95$$

$$\text{Probability of decay} = \lambda = \ln 2 / T_{1/2} = 0.693 / 950.4 \text{ d} = 0.0073 / \text{d} = 8.45 \times 10^{-9} / \text{sec.}$$

$$\begin{aligned} \text{Activity} &= \lambda * (\text{number of ions present}) \\ &= 8.45 \times 10^{-9} / \text{sec.} * 10^{13} \text{ ions} \\ &= 8.45 \times 10^4 \text{ disintegrations/ sec} \\ &= 2.28 \mu\text{Ci} \end{aligned}$$

Which is an acceptable activity value for radioactive tracer techniques. The <sup>20</sup>Ne beam was used for implantation due to its similarity to <sup>22</sup>Na in atomic number and its penetration into target material profile.

The cyclotron irradiation procedure went as follows on 12/14/90. First the silicon nitride and stainless steel specimens were placed into the specimen holder rig contained in the stainless steel pot. Starting from the top, the order of the specimens were the scintillator, and then stainless steel number 1, 2, 4 and silicon nitride number 8, 7, 6. The foils put in the other foil holding rig were in the order of number of 18, 19, 20, 21, 22, and 23 which corresponded to the gold foil thickness of 9, 8.5, 8, 7.5, 7, and 6.5  $\mu\text{m}$  respectively as discussed earlier.

Television cameras were set up to monitor the scintillator plate and the scintillator element on the specimen holding rig. The corresponding monitors were set up in the cyclotron control room. The area was cleared, and the cyclotron vault was se-

cured in the proper manner. The cyclotron beam of  $^{20}\text{Ne}$  and 2.5 MeV was then activated and sent to our test pot. The beam was tuned and shaped by the cyclotron operator by viewing the beam on the scintillating plate. The Faraday cup was placed in the beam line. The cyclotron operator condensed the beam to a size as small as possible and increased the current to as high as the 2.5 MeV energy limit allowed. The scintillator plate had 0.5 inch markers drawn from the center of the plate, and the beam was positioned in the middle of the target using these markers.

The beam current was read from the beam hitting the Faraday cup and creating a current which was sent to a count integrator which summed up the number of counts that it receives. The beam current could be calculated in the following manner. The count integrator was set to 20 namps for 60 secs at 1000 counts / sec which was 60000 counts total range for 20 namps for the integrator. Using this data in a proportion is used to find the real time current of the beam hitting the Faraday cup.

$$(\text{count} / \text{min}) / (60000 \text{ cnt} / \text{min}) = X \text{ neA} / 20 \text{ neA}$$

Solving for the X gives the beam current on the Faraday cup. Using this calculated beam current and a beam time corresponding to the number of desired ions to be implanted could be found.

A base reference was used for the time calculation of the  $^{20}\text{Ne}^{2+}$  beam. A beam current of 30 enA has the energy flux of :

$$\begin{aligned} 30 \text{ enA} (1.6 \times 10^{-19} \text{ coul} / e) &= 30 \times 10^{-9} \text{ coul} / \text{sec.} \text{ which corresponds to} \\ (30 \times 10^{-9} \text{ coul} / \text{sec}) / [(1.6 \times 10^{-19} \text{ coul} / \text{charge}) * (2 \text{ charges} / \text{particle})] \\ &= 9.38 \times 10^{10} \text{ part} / \text{sec} \text{ implanted by the 30 neA beam.} \end{aligned}$$

Using the previous calculated beam current, and a method of proportions the real particle implant rate could be calculated.

$$(\text{beam current neA}) / (30 \text{ neA}) = (Z \text{ part} / \text{sec}) / (9.38 \times 10^{10} \text{ part} / \text{sec})$$

where Z is the real particle implantation rate. The desired number of ions implanted divided by the calculated particle implantation rate gives the time required for the desired number of ions to be implanted.

We had problems with collecting data from the Faraday cup so the scintillator plate was used instead. The beam was moved so that it was positioned entirely on the scintillator plate and beam counts were taken and a beam current was calculated from this. Then the beam was moved to the aperture where only the top and bottom fraction of the beam passing through the aperture, known as 'wings', was measured and a current was found.

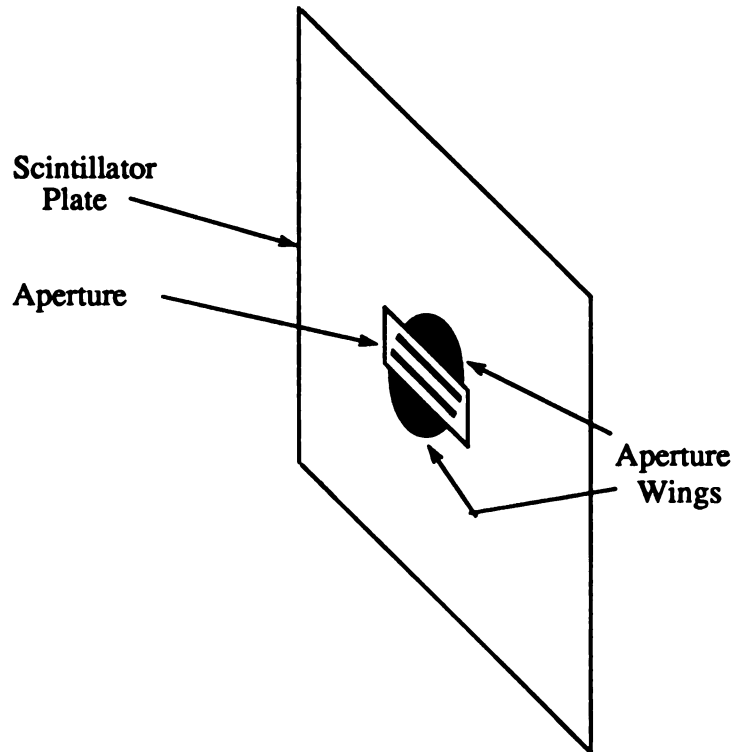


Figure 15 Cyclotron Beam 'Wings' on Scintillator Plate.

The first count number reading from the count integrator from the total beam on the scintillator plate was 9867 counts in one minute and the wings gave 759 counts/minute. The difference in these two numbers was considered to be the counts passing through the aperture and thus reaching the specimens. Using the given proportionality

$$(9108 \text{ cnts / min}) / (60000 \text{ cnts / min}) = X \text{ neA} / (20 \text{ neA})$$

and solving, a beam current of 2.9 neA was obtained. With this known beam current and using the implantation rate proportionality

$$(2.9 \text{ neA}) / (30 \text{ neA}) = X \text{ part / sec} / (9.38 \times 10^{10} \text{ part / sec})$$

an implantation rate of  $9.085 \times 10^9$  particles / second was calculated. If  $10^{12}$  particles were to be implanted, a beam time of  $(10^{12} \text{ part}) / (9.085 \times 10^9 \text{ part / sec}) = 110$  seconds would be needed.

Using this equation with the known beam time gives a test time matrix for the 'doubled up specimens' that were to be used for the nano-indentation experiment. This experiment was run without the use of beam degraders.

Table 7 'Doubled Specimens' Test Matrix

SPECIMEN	POSITION	NUMBER OF IONS	TIME
SCINTILLATOR	1	-	-
SS # 1	2	$10^{12}$	110 sec
SS # 2	3	$10^{13}$	1110
SS # 4	4	$10^{14}$	11000
SN # 8	5	$10^{12}$	110
SN # 7	6	$10^{13}$	1110
SN # 6	7	$10^{14}$	11000

The Faraday cup was dropped out of the beam line and the beam traveled to the specimens. The specimens were not implanted in the above order number but from the shortest implant time to the longest.

The beam current fluctuated a lot but the implanting times were not changed. The beam current was monitored and an implanted ion number was established from

that. Using the measured counts before and after a run, the average of the counts for each run was used to determine the number of ions implanted.

The size of the beam was estimated by the cameras which gave the dimensions to be approximately 1.00 x 0.5 inch which gives an total area of  $0.5 \text{ inch}^2 = 3.23 \text{ cm}^2$ . This beam size is larger than the aperture size of  $0.125 \times 0.625 \text{ inch} = 0.078 \text{ inch}^2 = 0.5 \text{ cm}^2$ . This is due to the refraction of the beam around the edges of the scintillator plate. Since the beam intensity was measured at the scintillator plate of a given dimension, the scintillator aperture total area will be used for the area implanted on the specimen, since that is where the highest intensity of the beam would hit.

SS # 1

Pre-Aperture total - wing cnt =  $9426 - 759 = 8667 \text{ cnts/ min}$

Post-Aperture total - wing cnt =  $9867 - 1150 = 8717 \text{ cnts/ min.}$

Average of intensity through aperture =  $8692 \text{ cnts/min}$

using previous ratio  $8692 / 60000 = x / 20 \text{ neA}$

$x = \text{beam current} = 2.897 \text{ neA}$

then  $2.897 \text{ neA} / 30 \text{ neA} = x / 9.38 \times 10^9 \text{ part/sec}$

$x = \text{particles second} = 9.059 \times 10^9 \text{ particles/second.}$

Total particles in 110 second run =  $9.059 \times 10^9 \text{ particles/second} * 110 \text{ seconds}$

$= 9.965 \times 10^{11} \text{ particles}$

which gives  $1.99 \times 10^{12} \text{ particles / cm}^2$ .

Using this calculation for the rest of this experiments run, Table 8 was constructed.

Table 8 Actual Number of Ions Implanted in Specimen

SPECIMEN	AVG. INTENSITY	TIME	PARTICLES	PART/AREA
SS # 1	8692cnts/min	110 sec	$9.97 \times 10^{11}$	$1.99 \times 10^{12}$
SS # 2	6444	1100	$6.72 \times 10^{12}$	$1.34 \times 10^{12}$
SS # 8	14968	110	$1.56 \times 10^{12}$	$3.12 \times 10^{12}$
SN # 7	17891	1100	$1.87 \times 10^{13}$	$3.73 \times 10^{13}$
SS # 4	14943	10000	$1.56 \times 10^{14}$	$3.11 \times 10^{14}$
SN # 6	11031	10000	$1.15 \times 10^{14}$	$2.31 \times 10^{14}$

Looking at the fluctuating intensities, Table 9 shows the percent change of the beam intensity (counts / minute) which is related to the beam current.

Table 9 Cyclotron Beam Current Fluctuation

INTENSITY	% VARIANCE FROM SMALLEST	BEAM CURRENT
8692 cnts/min	34.9	2.89 neA
6444	0	2.15
14968	132	4.99
17891	178	5.96
14943	132	4.98
11031	71	3.67

Next the single ceramic specimens were implanted. This run required the use of beam degraders to create a crude uniform concentration profile along the full length of the radius portion of the specimen. At this time the intensity was 22716 clicks /

minute which from a previous equation gives 7.57 neA. This current corresponds to  $2.33 \times 10^{10}$  particles/second. A time of 180 seconds was chosen for radiation time for each of the six degraders, which gives a total implanting time of 1080 sec which gives  $2.36 \times 10^{13}$  particles per specimens which is  $5.11 \times 10^{13}$  ions/cm<sup>2</sup>. The six gold foil degraders thicknesses are shown in Table 10.

Table 10 Beam Degrader Foil Thickness

Foil Degrader	Thickness
A1	9.0 $\mu$ m
A2	8.5 $\mu$ m
A3	8.0 $\mu$ m
A4	7.5 $\mu$ m
A5	7.0 $\mu$ m
A6	6.5 $\mu$ m

Table 11 Test Matrix for the Single Specimens with Degraders

SPECIMEN	POSITION	NUMBER OF IONS	TIME
SCINTILLATOR	1	-	-
SN # 16	2	$10^{13}$	1080 sec
SN # 15	3	$10^{13}$	1080 sec
SN # 14	4	$10^{13}$	1080 sec
SN # 13	5	$10^{13}$	1080 sec
SN # 12	6	$10^{13}$	1080 sec
SN # 11	7	$10^{13}$	1080 sec

So for each of the specimens, all six gold foils were placed in front of the specimens one at a time for 180 seconds a piece.

### 3.4 Nano Indentation

The specimens were all kept in their copper mounts during transportation in order to keep them in order. Our procedure was to first run a set of hardness tests on the specimens with the greatest number of implanted ions in order to discover a change in hardness. If the highest dosed specimens contained no damage, then the lower dosed specimens were sure to contain no damage either. The specimens were only removed from the mounts when needed. The first specimen used was Silicon Nitride no. 6 implanted with  $10^{14}$  ions. Only one of the double mounted specimens were used. The specimen was mounted on a metal stud by using a hot plate to heat the stud and then melting a glue stick on the hot stud. The specimen was then put on the stud and left to cool.

For mounting the mount holder was turned face down and propped up at its ends originally with pieces of cardboard to permit the specimens to fall below the specimen holder's surface. The cardboard was quickly replaced with thin metal pieces which held the unit more steady since mounting flatness could make the difference between good or no data from the run. The studs were then positioned so that the implanted edge was facing the front of the holder and that the edge was perpendicular to the holding rig, see Figure 16.

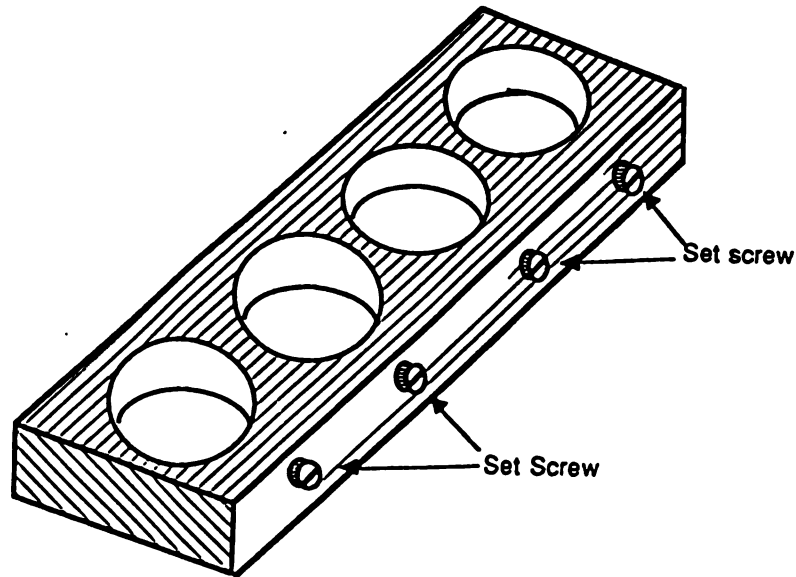


Figure 16 Nano Indenter Specimen Holder

The studs were then secured in the holder by a set screw which cocked the studs when the torque of tightening made contact with the stud, which tilted the specimens non flat position. To get around this dilemma, the stud was first cocked counter rotation and the set screw was not tightened very hard, but enough to hold the maximum 12 grams of indenter force. This routine of trail and error continued until a visibly flat specimen surface was obtained. Once secure and flat, the specimens were sprayed with 'Dust Off' and mounted in the Nano Indenter. The viewing lens was then placed at the middle of the edge of the specimen with the computer controlled system. The insulated cabinet surrounding the indenter was closed and the room where the indenter sat was closed off.

The room temperature was monitored and was not allowed to fluctuate more than 0.5 degrees centigrade. Since the sensitive machine accounts for thermal drift, a large temperature drift would be considered too large for the machine to correct for.

The menu driven computer program was set up to run. The main computer screen is shown in Figure 17.

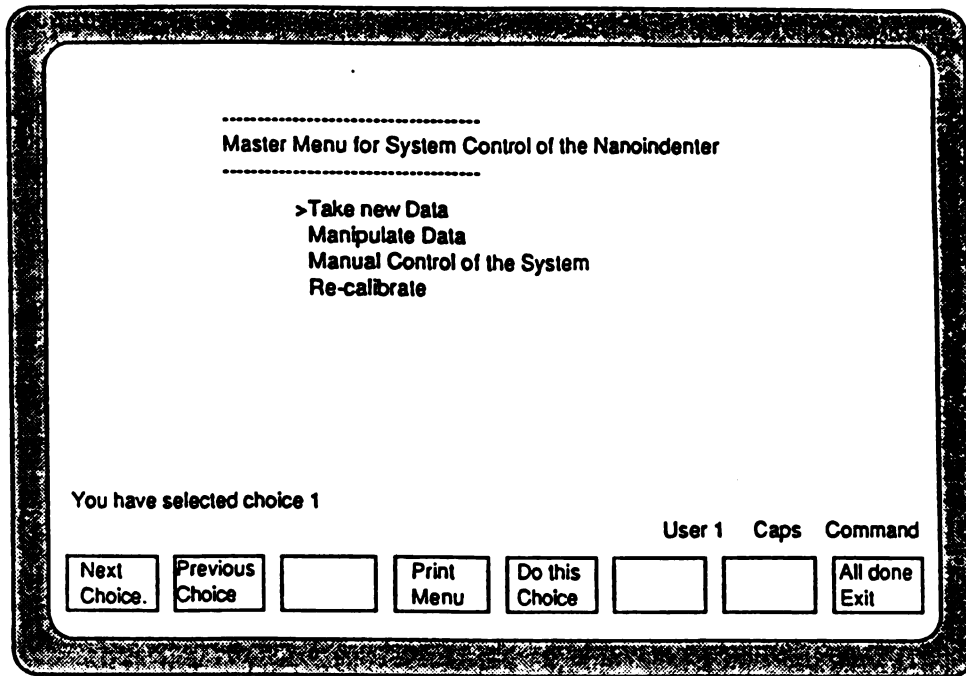


Figure 17 Master Menu of Nano Indenter Computer.

The indentation procedure had to be set up. The closest allowable distance to the specimen's edge was 4  $\mu\text{m}$ . The specimen surface had to be flat since the indenter works on the basis to sensing the specimen surface location. If the specimen surface was not flat, the diamond tip might touch and scratch the surface while moving to the next indentation spot. On the other hand if the surface slopes down, the indenter will move down past where it believes the surface should be, thus aborting the indent. When either of the two conditions arise, the Nano Indenter is said to 'Bomb Out', thus not picking up any data for that point. Since the surface can never be perfectly flat, a head repositioning step is performed at indent locations where the machine should reevaluate the surface plane. Head repositioning steps are automatically done at the beginning of each array of indents taken.

The operator called each indentation run, "material" which is confusing, so this

notation was changed from 'material' to 'run'. The procedure that the indenter was programmed to perform was as follows:

- 1- contact surface
- 2- load indenter to displacement of 50 nm deep
- 3- unload indenter by 15% of full rate to 80% retracted out of indent
- 4- load to 100 nm
- 5- unload at 15% rate to 80% retract
- 6- load to 150 nm
- 7- unload at 15% rate to 80% retract
- 8- load to 200 nm
- 9- hold indenter, take 20 data points
- 10- unload at 15% rate to 80% retract
- 11- hold indenter, take 60 data points
- 12- unload to 100% retracted

This procedure gave data to calculate the hardness, elastic modulus, plastic deformation, stiffness and compliance of the material.

The first specimen, silicon nitride no.6 ( $10^{14}$  ions implanted), had three runs on its surface. The runs were labeled "Run A, B and C", with the run A in the middle of the specimen, see Figure 18. The numbers in the parenthesis are the x and y coordinates. The first run was to get familiar with the machine, so the large distance between indents could have stepped over the radiated area. Using the TRIM calculated concentration peak profile, the full width at half maximum (FWHM) of the damaged peak is  $0.25\mu\text{m}$ , thus the ideal step distance between indents was  $0.125\mu\text{m}$ . But the indents should be taken far enough apart so the area of indent is not effected by the previous indent. An indent separation distance of 10 times the width of the indent is a general rule of thumb. This would result in a indent width of  $0.025\mu\text{m}$ , which was too small for the Nano Indentation machine. In order to get better resolution distance perpendicular to the edge, we placed some of the indentation arrays at an angle. The run C array was to focus around the area of damage at a slant for good resolution.

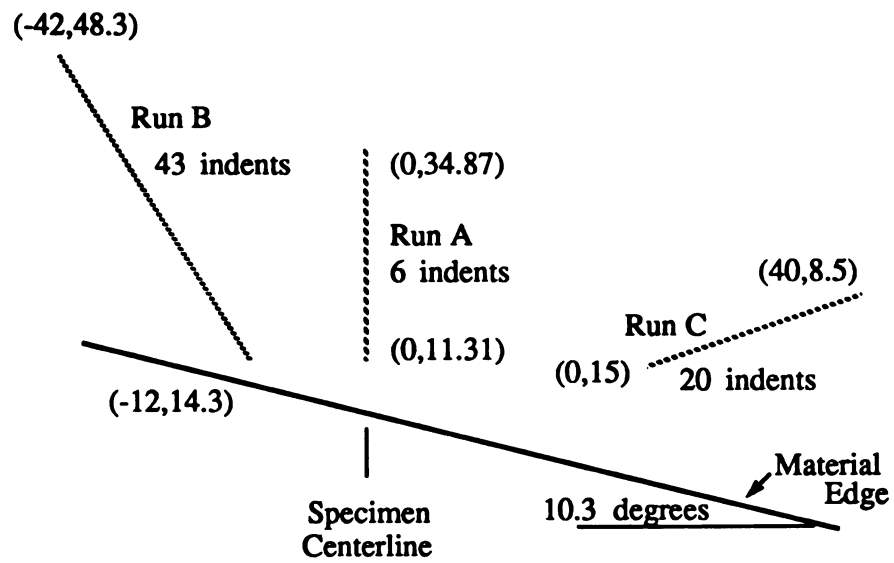


Figure 18 Runs A, B and C on Silicon Nitride no 6 ( $10^{14}$  ions)

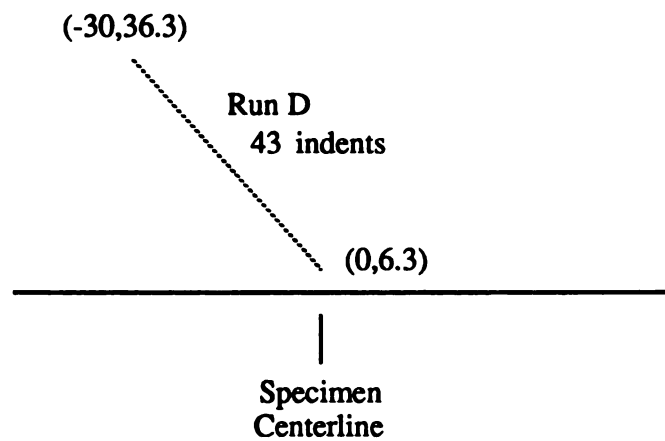


Figure 19 Run D on Silicon Nitride no. 7 ( $10^{13}$  ions)

Run E on Silicon Nitride no. 10 which is the control (non implanted) specimen.

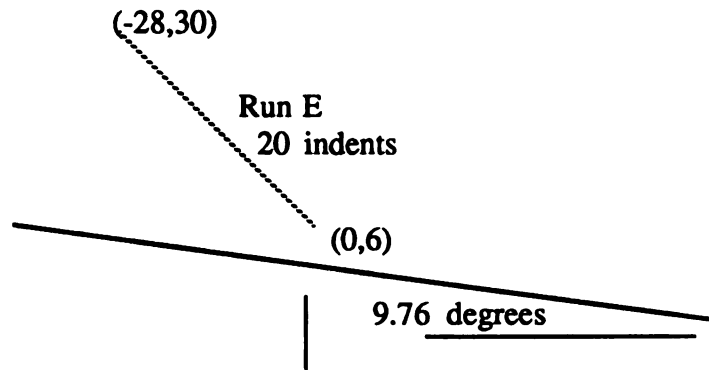


Figure 20 Run E on Silicon Nitride no. 10 (control specimen)

The time required to take one indent was on the average of 15 minutes which made for a long time to make a run. In order to make better use of time, several arrays were done in one programmed setting. Runs F, G and H were done on stainless steel no.4 ( $10^{14}$  ions). Run H was located off of the implanted region at the far left corner. This was considered to be the control run for the stainless steel.

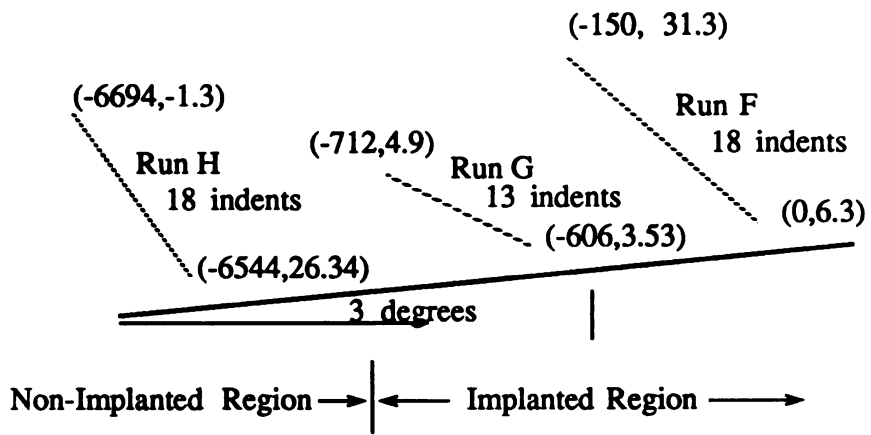


Figure 21 Runs F, G and H on Stainless Steel no.4 ( $10^{14}$  ions)

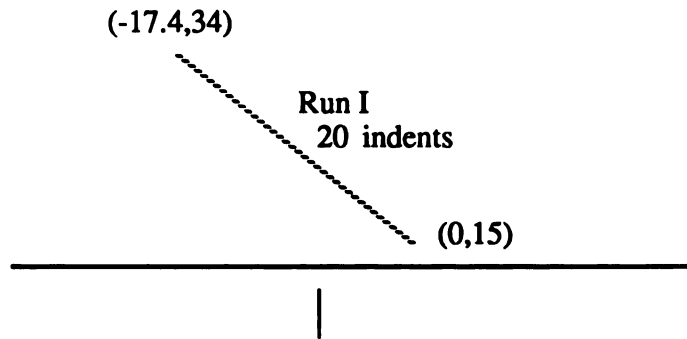


Figure 22 Run I on Silicon Nitride no.7 ( $10^{13}$  ions)

Run J was done on a different material not concerning this subject. The runs were not done in sequence of material number or number of implanted ions but rather based on information obtained from previous runs.

Run K, L, and M were done on stainless steel no.2 ( $10^{13}$  ions)

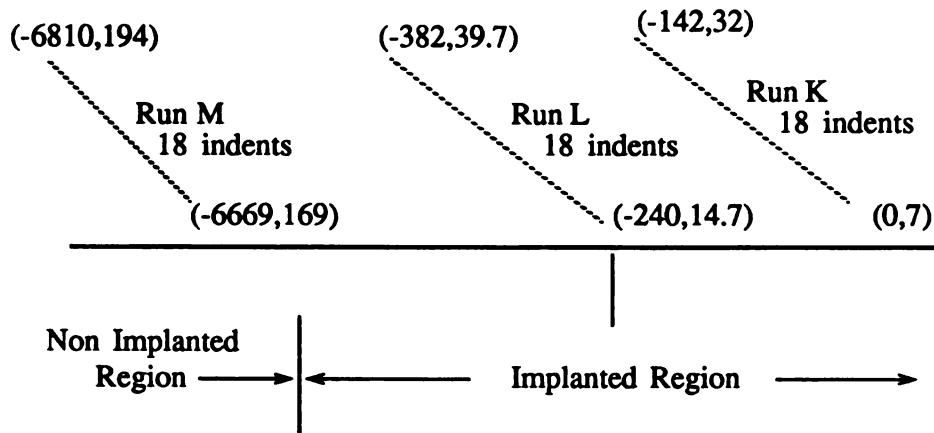


Figure 23 Run K, L, and M on stainless steel no.2 ( $10^{13}$  ions)

Runs N and O were done on materials not part of this subject. Run P was on stainless steel no.1 ( $10^{12}$  ions) which was the lowest ion implanted dose.

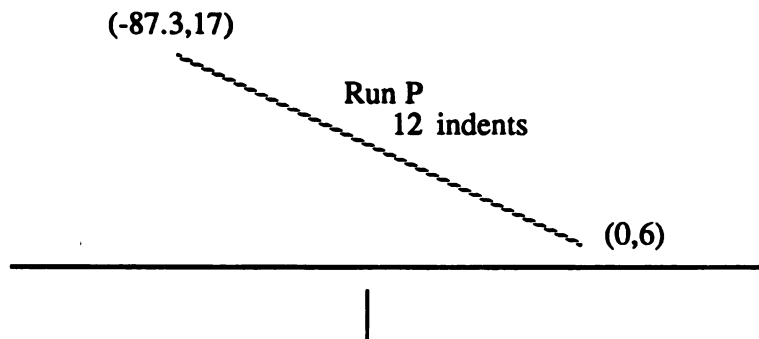


Figure 24 Run P on stainless steel no.1 ( $10^{12}$  ions)

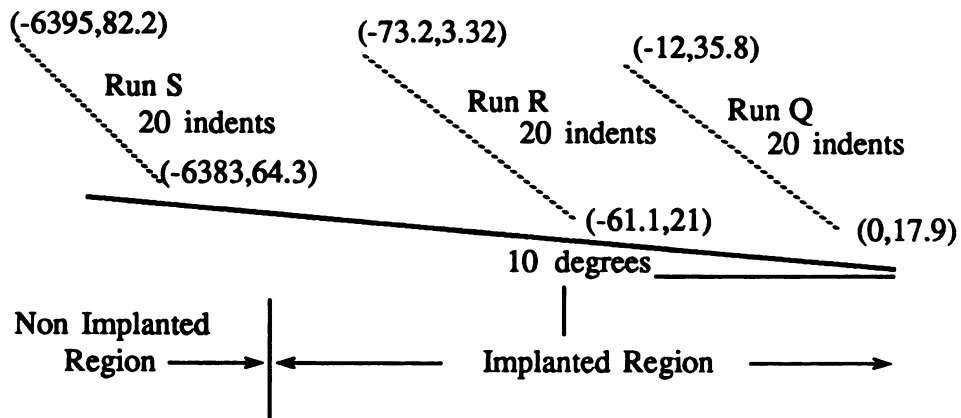


Figure 25 Run Q, R, and S on Silicon Nitride no.8 ( $10^{12}$  ions)

## CHAPTER 4

### RESULTS

#### 4.1 Detection of Specimen's Radioactivity

The 2.5 MeV / nucleon cyclotron beam of  $^{20}\text{Ne}$  had a total energy of 50 MeV which is above the Coulomb barrier for both the ceramic and stainless steel specimens, thus having the potential of causing radioactivity. After the implanted specimens were removed from the pot, they were found to be radioactive. The specimens exposed longest (the silicon nitride # 6 and stainless steel # 4) were found to be the most active. The silicon nitride # 6 was the most active of the two and the gamma ray was detected with a hand held safety detector, with the activity in counts / minute which was read from a dial gauge on the detector. This detector was used instead of the germanium detector at the Engine Research Laboratory since it was portable and available. Table 12 shows the radioactivity of Silicon Nitride # 6

Table 12 Activity of Silicon Nitride # 6

DATE	CNTS/MIN	LN CNTS/MIN	TIME	REF. TIME
12/15/90	41864	10.64	5:22	0 hr
12/15/90	23000	10.04	6:35	1.22
12/15/90	15000	9.62	7:36	2.23
12/15/90	5000	8.52	11:24	6.03
12/16/90	300	5.70	15:24	10.03

Using the exponential decay law  $A = A_{\text{int}} \exp^{-\lambda t}$

$$300 \text{ cnts/min} = 23000 \text{ cnts/min} * \exp^{-[(\ln 2 / \text{half life}) * 8.81 \text{ hr}]}$$

gives a half life of 1.4 hours. Using these numbers, an original activity of 41864.97 cnts/min was calculated which corresponds to 1.13 $\mu\text{Ci}$ .

Using the gamma detector at the Engine Research Laboratory, the energies at

which the gamma rays were being produced could be found. Five different detection runs were taken on the following times and dates:

Date	Time
12/18	10:15
12/18	16:15
12/19	9:00
12/19	23:00
12/20	21:15

The spectrum was taken on 4098 channels and the last three spectrum showed no gamma peaks other than background. The first spectrum was stripped with background shown in Figure 26. The x axis is the channel number and the y axis is the number of gamma rays intercepted by the detector, known as counts.

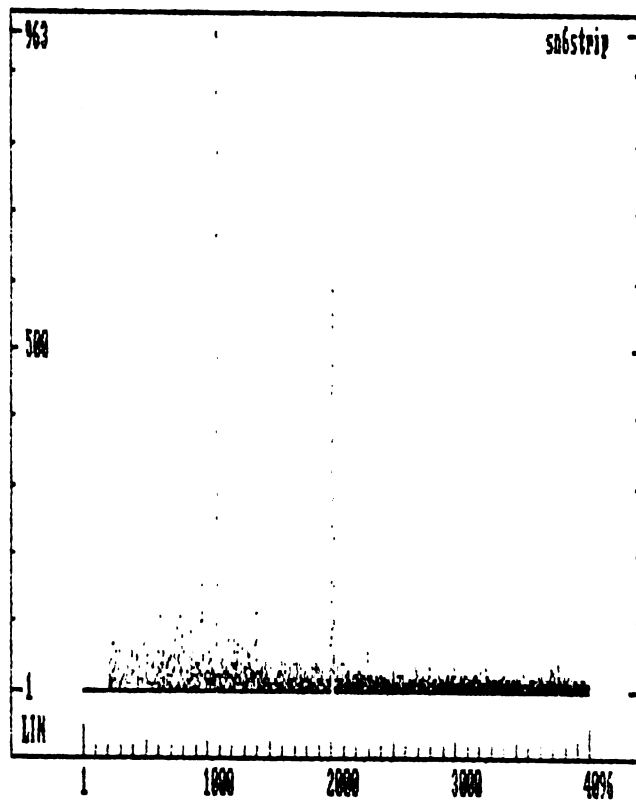


Figure 26 Silicon Nitride no. 6 Detected Spectrum

An energy calibration translates the spectrum channel number to the energy of the gamma ray. The energy calibration shown in Table 13, sets the largest peak at channel 1079.14 in the detected spectrum to a gamma ray energy of 271.07 KeV.

Table 13 Spectrum Energy Calibration

CHANNEL	ENERGY
952.09	238.36 KeV
1079.14	271.07
1823.09	462.6

The second peak is to the right of the first and is located at slightly over channel 2000. This is the residue as a result of the subtraction of a large background peak which had shifted slightly. The next spectrum showed the same 271.07 KeV gamma ray but at a lesser intensity. There is no element in the Standard Table of Radioactive Elements with this energy and a half life of 1.4 hours. The radioactivity had essentially decayed too much by the time the germanium detector was used to make a good assessment of the energy. Using the half life calculated from the first detection, the activity was  $3.136 \times 10^{-17}$   $\mu\text{Ci}$  by the time the first spectrum was read.

## 4.2 Nano Indentation

### Control Silicon Nitride (Run E, S)

The Control (non-implanted) Runs of Silicon Nitride were examined first. The hardness values of Run E on Silicon Nitride no.10 and Run S on Silicon Nitride no.8 were smoothed and averaged giving the result is shown in Figure 27.

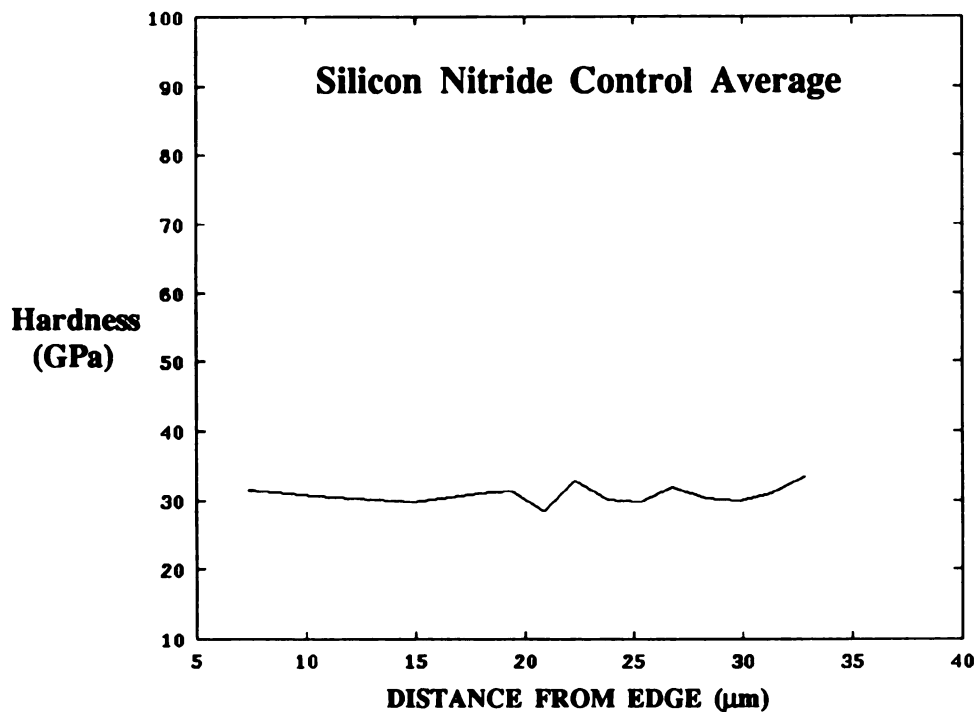


Figure 27 Averaged Control Hardness of Silicon Nitride

This curve will be used as merely a light reference for all the silicon nitride hardness plots. Each individual run has its own damaged and non damaged area statistics, which are all different from the others. The surface finish, exact beam location, beam intensity and indent location are all topics of data variation. Since the variation in data between runs is significant, the conclusions will be based most heavily on the comparisons of the damaged against non-damaged areas for the given run. The statistical values for this run are as follows:

**Averaged Control Run's Hardness Statistics (Run E, S)**

samples	mean	std. dev.	sample std. dev.
14	30.78	1.28	1.327

All units in GPa. The sample standard deviation is always displayed and is used when the number of samples is less than 50. The difference in formula between standard and sample standard deviation is that sample standard has (n-1) replacing a 'n' in the denominator. Additional information about the implanted ion damage may be obtained from the change in elastic modulus of the material. The average of elastic modulus control runs is shown in Figure 28.

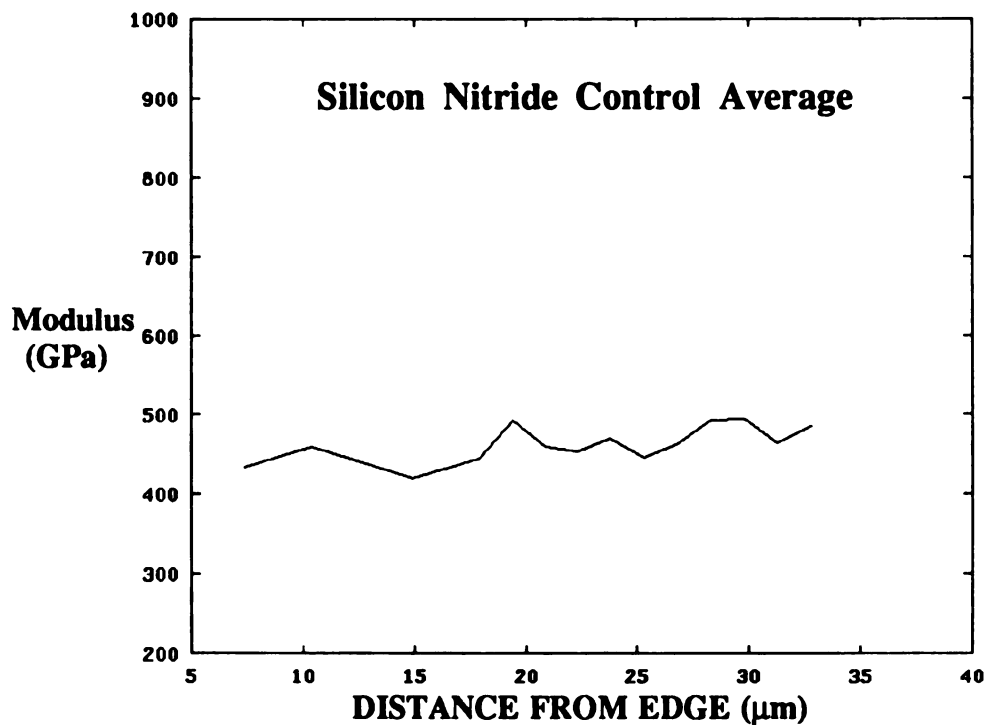


**Figure 28 Averaged Control Elastic Modulus of Silicon Nitride.**

This averaged curve will be used for control data representation of the elastic modulus on silicon nitride for the same reasons as stated for the hardness data. The statistical values for this data are as follows:

**Averaged Control Entire Run Hardness Statistics (Run E, S)**

samples	mean	std. dev.	sample std. dev.
14	462.3	22.1	22.95

## **$2 \times 10^{14}$ ions/cm<sup>2</sup> Dose Silicon Nitride (Run B, C)**

Depths of 50, 100, 150 and 200 nm were taken at each indent. The deepest indent is the most accurate for representing the material hardness. The shallower indents showed more surface and grain boundaries effects. Also the percent error of hardness value is lowered as more of the diamond tip is exposed to the material, thus the deeper the indent, the less the error in measurement. For these reasons, only the values for the 200nm will be used to predict change in hardness. The hardness values shown may be considered high by some deep indent standards. There are several methods to measure material hardness, none of which are directly related to the other. As explained by P. Blau [13].

"Hardness numbers, even though expressed in the same units, need not necessarily be the same if the same load is applied using indenters of different shapes... Since hardness numbers depend on the method of measurement, hardness is not a basic property, but rather a characteristic of the material being tested under the specified indentation conditions... Different hardness scales do not use the same area of the impression in their calculations. For example, Brinell and Knoop hardness are given as load per unit projected area while the Vickers Hardness is expressed as a load per unit facet area. This difference is one factor which can lead to different hardness numbers under the same applied indenter load."

The main factor attributing to high hardness values was as the indents were taken at deeper intervals (50, 100, 150 and 200nm), the hardness decreased, i.e. from 100 GPa for the 50 nm indent to 40 GPa for the 200nm indent. This phenomenon is normal for nano indentation since only the surface is tested and not the bulk material which represents the whole specimen. This hardness values did not reach a constant number for the range tested, but they would decrease to a standard value as deeper indents were taken. A further indication of high surface hardness values for nano indentation is the high documented hardness values for materials tested by nano indentation methods as shown in Table 14.

Table 14 Varying Hardness Values

Material	Standard Hardness	Nano Indentation Hardness	Measured Hardness
NC 132	2 GPa [14]	22 GPa [15]	30 GPa
17-4PH	1 GPa [16]	8 GPa [13]	7 GPa

The 'standard hardness' values are for the bulk material, measured by deep indentation tests which result in lower hardness values than nano indentation tests. The documented 'nano indentation hardness' of 22 GPa [15] for the NC 132 was a result of a higher indentation load than what was used for the 'measured hardness'. The measured hardness of 30 GPa used a light load resulting in a shallow indent. As explained earlier, the hardness values decrease as the load is increased on the nano indenter. Therefore, since the measured hardness tests for NC 132 used a lighter load, the hardness values were greater than that of the documented nano indentation hardness.

It is for this reason that most published nano indented hardness values are normalized or used as reference. The values are left in original form for this research so that a solid basis is maintained for future work. Thus the hardness values shown in this work are the unique values for the shallow nano indentation tests.

Run B of Silicon Nitride no.6 ( $2 \times 10^{14}$  ions/cm<sup>2</sup>) showed a softening of the ceramic in relation to its own average value which does not seem to correspond to the Control Average Value. Figure 29 shows the hardness at a depth of 200 nm into the material from the surface. The horizontal lines in Figure 29 indicate the 2 x standard deviation window. This region is a 95.4% confidence region, meaning in this case that the values located outside this region have a 95.4% probability of indicating a change in hardness..

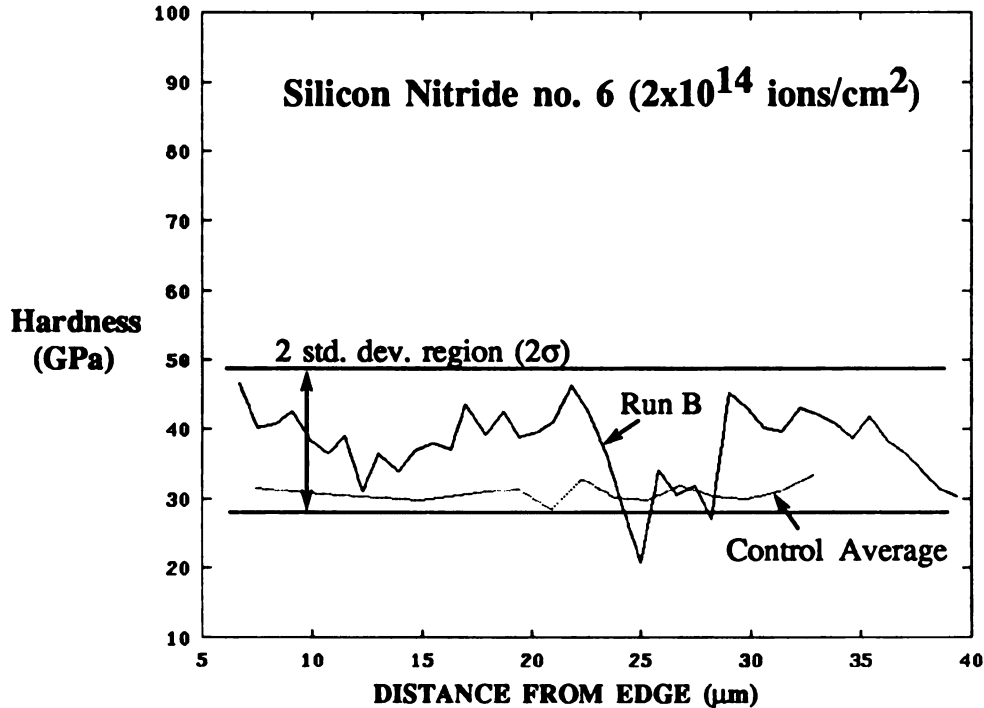


Figure 29 Hardness of Silicon Nitride no.6 (Run B)

The statistics on Run B are as follows, with the damaged portion being from 22 to 29 $\mu\text{m}$ :

$2 \times 10^{14}$  Dose (Run B) Silicon Nitride Non Damaged Portion Statistics

samples	mean	std. dev.	sample std. dev.
34	39.48	3.91	3.97

$2 \times 10^{14}$  Dose (Run B) Silicon Nitride Damaged Portion Statistics

samples	mean	std. dev.	sample std. dev.
7	29.81	4.76	5.144

The soft area is not a well determined peak with a full width at half max (FWHM) of 0.5 $\mu\text{m}$  as TRIM suggested, but rather more of two soft spots approximately 3 $\mu\text{m}$  apart, with the softest being at 25 $\mu\text{m}$  into the material. This deviation from the

TRIM's calculated value will be discussed later. The graph shows a slight hardening immediately before and after the soft portion with the values of 46.3 and 45.2 respectively compared to the non damaged mean hardness of 39.48. The region of damage has a 9.67 GPa average hardness drop which is a 24.5% average decrease in hardness when compared to the outside damaged area (ODA) mean value. If the softest point is compared to the ODA mean, a 47.5% decrease in hardness results. A mean hardness value of 39.48 GPa was found for the ODA, which is a 8.7 GPa difference from the Control Average Run. This change could be attributed to the Nano Indenter System Calibration, possibly from a noted 31% change in room humidity that occurred between the B and Control Runs. Figure 30 shows the elastic modulus for Run B compared with its Averaged Control Run.

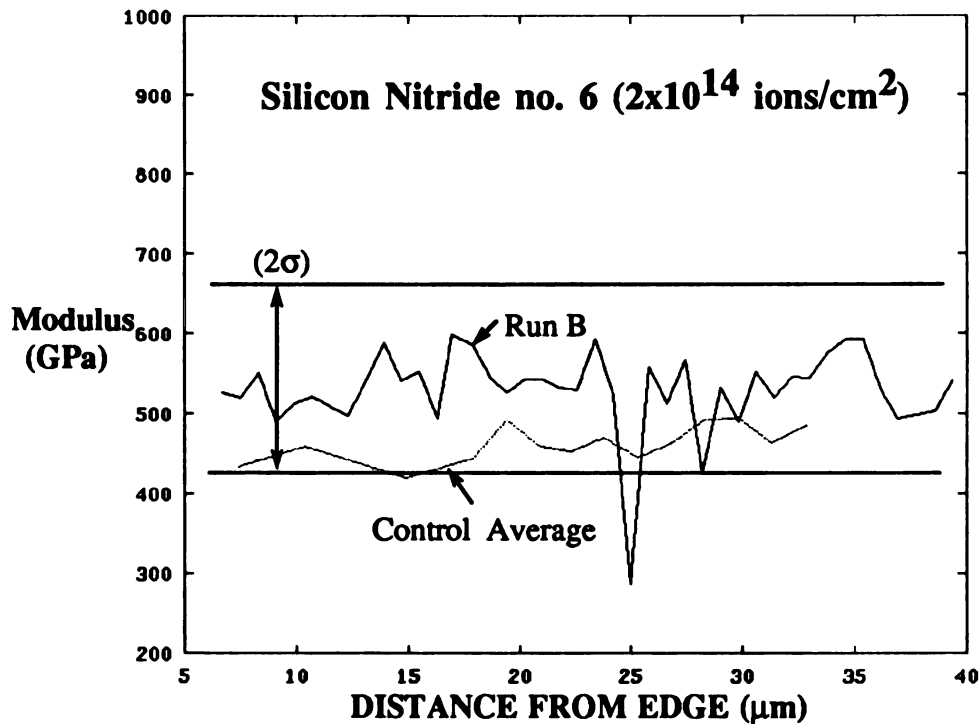


Figure 30 Elastic Modulus of Silicon Nitride no.6 (Run B)

As in the hardness plots, a decrease in elasticity is shown to occur at 25 $\mu\text{m}$ . The double soft region is not as apparent in this case as in the hardness plot. Once again the Control Average is much lower than that of Run B, which gives further evi-

dence of varying machine calibration. If the low extreme value is used along with the ODA mean for this run, the Silicon Nitride decreased in elasticity by 46.5 %. This value is close to the 47.5% decrease in hardness. Even though the second soft peak is not dominant, it still falls outside the ODA standard deviation indicating that the damaged region for elasticity still exists for 22 to 29 $\mu$ m.

The statistics on the Run are as follows, again with the damaged portion being from 22 to 29 $\mu$ m:

$2 \times 10^{14}$  Dose (Run B) Silicon Nitride Non Damaged Portion Statistics

samples	mean	std. dev.	sample std. dev.
34	536.4	30.19	30.65

$2 \times 10^{14}$  Dose (Run B) Silicon Nitride Damaged Portion Statistics

samples	mean	std. dev.	sample std. dev.
7	494.6	98.32	106.2

In Run C, a window of the beginning of the damaged region can be seen in Figure 31.

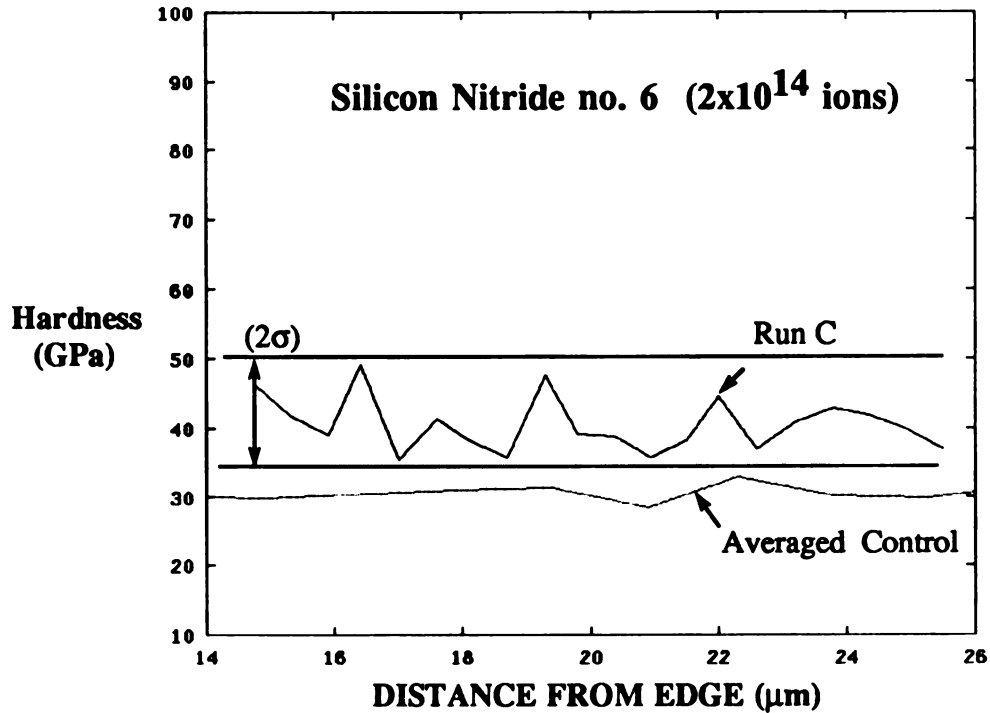


Figure 31 Hardness of Silicon Nitride no.6 (Run C)

This data is tough to decipher and does not show the signs of softening. This was taken to the right of Run B and could have been outside the implanted area. Another possibility is that of miscalculated distance, so that the shown distance in from the edge may not be correct. In any case, this run did not seem to traverse the damaged region so it may be used as a Control Run.

$2 \times 10^{14}$  Dose (Run C) Silicon Nitride Entire Run Statistics

samples	mean	std. dev.	sample	std. dev.
20	40.55	3.89	3.99	3.99

Run C was performed on the same day as Run B. The mean here is 40.55 GPa comparing it to the ODA Run B mean of 39.48 GPa shows that the indenter gave consistent values for that day, but very different values for the other days. The entire run standard deviation for Run C is 3.89, and 3.91 for the ODA region of Run B, so these statistics indicate that Run C is a ODA Run.

This same run gave the elastic modulus, shown in Figure 32..

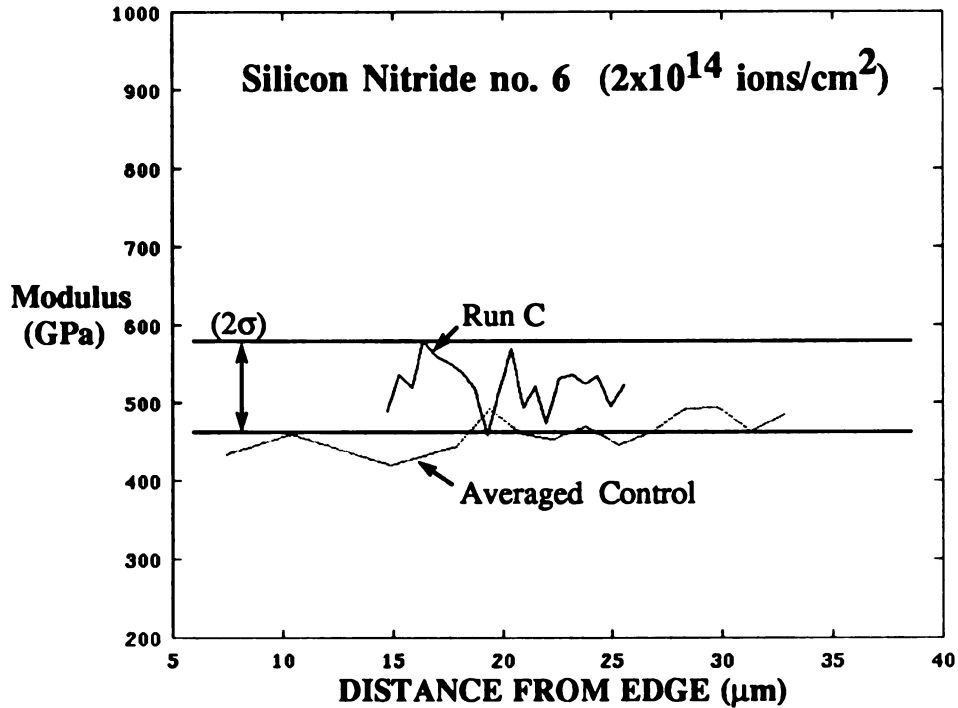


Figure 32 Elastic Modulus of Silicon Nitride no.6 (Run C)

The statistics for this run are:

$2 \times 10^{14}$ Dose (Run C) Silicon Nitride Entire Run Statistics			
samples	mean	std. dev.	sample std. dev.
20	523.5	30.17	30.95

Notice that the range of distance of this plot is greater than the hardness plot, giving the curve a more short and choppy appearance. The standard deviation of 30.17 is greater than that of the Averaged Control Run, but all points are in an acceptable confidence region. Thus this run can still be considered a Control Run.

## $2 \times 10^{13}$ ions/cm<sup>2</sup> Dose Silicon Nitride (Run D, I)

Figure 33 shows Runs D and I and the Averaged Control Run on the next lower implanted ion dose in Silicon Nitride, no.7 ( $2 \times 10^{13}$  ions/cm<sup>2</sup>).

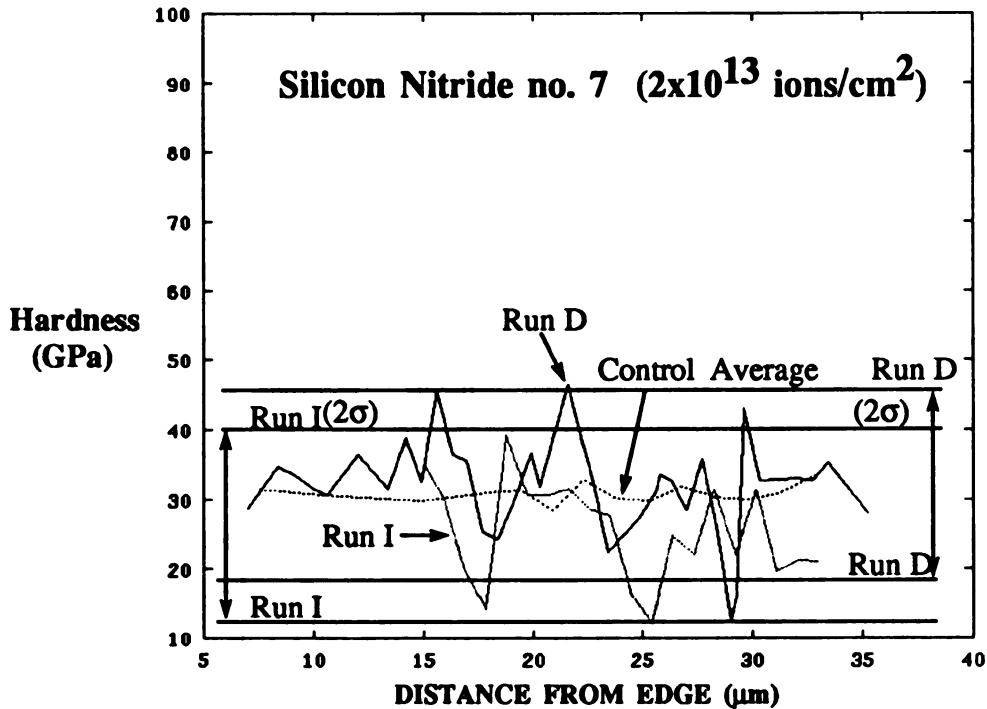


Figure 33 Hardness of Silicon Nitride no.7 (Run D and I)

The data here is hard to decipher. Runs D and I show a resemblance to each other but the resemblance to the Runs on  $2 \times 10^{14}$  dosage is somewhat lost. Run I has a ODA mean hardness value of 26.79 GPa where Run D has a ODA value of 32.8 GPa. These runs were taken on different days. Run I shows a softening in two places, one at 18μm and at 25μm. Run D has three soft spots at the depths of 18, 24 and 29μm. Unfortunately the resolutions of the points are not better, there is a possibility of a softer point at 25μm for Run D according to the straddling of the point's slopes around it. The statistical data on these runs are as follows:

**$2 \times 10^{13}$  Dose (Run D) Silicon Nitride Non Damaged Portion Statistics**

<b>samples</b>	<b>mean</b>	<b>std. dev.</b>	<b>sample std. dev.</b>
27	32.81	7.45	7.59

 **$2 \times 10^{13}$  Dose (Run D) Silicon Nitride Damaged Portion Statistics**

<b>samples</b>	<b>mean</b>	<b>std. dev.</b>	<b>sample std. dev.</b>
9	29.9	4.14	4.39

 **$2 \times 10^{13}$  Dose (Run I) Silicon Nitride Non Damaged Portion Statistics**

<b>samples</b>	<b>mean</b>	<b>std. dev.</b>	<b>sample std. dev.</b>
14	26.79	6.82	7.08

 **$2 \times 10^{13}$  Dose (Run I) Silicon Nitride Damaged Portion Statistics**

<b>samples</b>	<b>mean</b>	<b>std. dev.</b>	<b>sample std. dev.</b>
6	22.46	6.56	7.18

The damaged area portion is again taken to be 22 to 29 $\mu$ m where softening was seen on the  $2 \times 10^{14}$  dose Silicon Nitride. The damaged area results are tough to confirm since the hardness from the non damaged areas is as low as the damaged area. The standard deviations of the ODA runs are both higher than the damaged area's standard deviation. This data is much rougher than the previous runs, but the results should be based on comparing the damaged region statistics to the ODA statistics for same specimen. Based on this data, this region of interest does not clearly show material damage.

The elastic modulus for Runs D and I are shown in Figure 34.

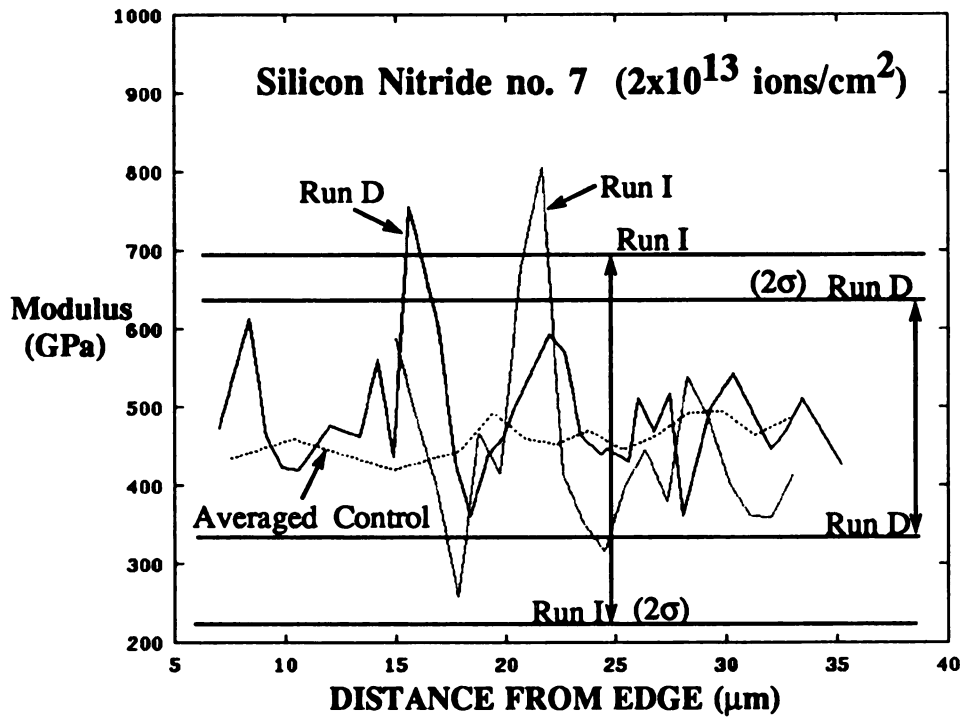


Figure 34 Elastic Modulus of Silicon Nitride no.7 (Run D and I)

The statistics for these runs are as follows:

$2 \times 10^{13}$  Dose (Run D) Silicon Nitride Non Damaged Portion Statistics

samples	mean	std. dev.	sample std. dev.
23	493.4	83.3	85.2

$2 \times 10^{13}$  Dose (Run D) Silicon Nitride Damaged Portion Statistics

samples	mean	std. dev.	sample std. dev.
9	467.2	56.68	60.11

$2 \times 10^{13}$  Dose (Run I) Silicon Nitride Non Damaged Portion Statistics

samples	mean	std. dev.	sample std. dev.
14	475.0	136.5	141.6

**$2 \times 10^{13}$  Dose (Run I) Silicon Nitride Damaged Portion Statistics**

<b>samples</b>	<b>mean</b>	<b>std. dev.</b>	<b>sample std. dev.</b>
<b>6</b>	<b>385</b>	<b>42.4</b>	<b>46.44</b>

As in the hardness plots, there exists regions of softening where for higher ion dosages there were not any. As in the hardening plots, the apparent softening at 18  $\mu\text{m}$  clouds the 25  $\mu\text{m}$  softening. Notice that Run I has both the highest and lowest values, thus a higher standard deviation of 136.5 for the ODA regions. This elastic data is rougher than the hardness data, which led us to believe that the material was not as polished as the others. In any case, the softening is not noticeably apparent.

## $2 \times 10^{12}$ ions/cm<sup>2</sup> Dose Silicon Nitride (Run Q, R)

The lowest dose ( $2 \times 10^{12}$ ) Silicon Nitride no. 8 is shown in Figure 35.

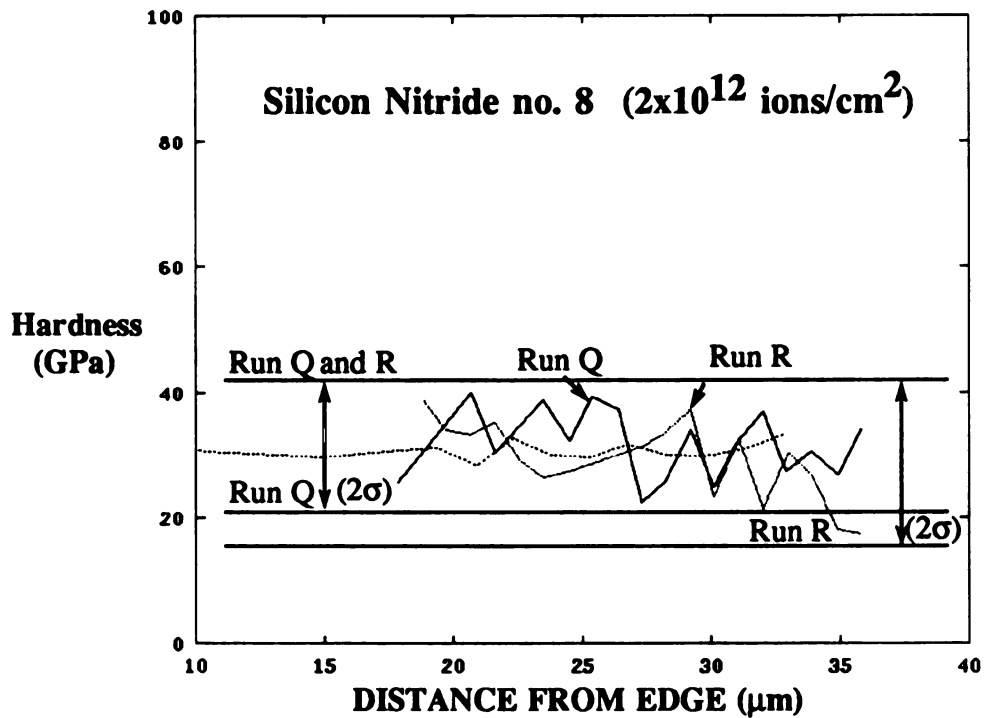


Figure 35 Hardness of Silicon Nitride no.8 (Runs Q and R)

The statistical data from these runs are as follows:

### $2 \times 10^{12}$ Dose (Run Q) Silicon Nitride Non Damaged Portion Statistics

samples	mean	std. dev.	sample std. dev.
11	31.19	4.54	4.77

### $2 \times 10^{12}$ Dose (Run Q) Silicon Nitride Damaged Portion Statistics

samples	mean	std. dev.	sample std. dev.
6	32.7	6.55	7.18

$2 \times 10^{12}$  Dose (Run R) Silicon Nitride Non Damaged Portion Statistics

samples	mean	std. dev.	sample std. dev.
12	29.1	9.10	7.41

$2 \times 10^{12}$  Dose (Run R) Silicon Nitride Damaged Portion Statistics

samples	mean	std. dev.	sample std. dev.
5	29.64	2.57	2.87

Fortunately, this data is much better than the previous. The standard deviations are much smaller, making it easier to see data deviation. This run shows no damaged area. Actually the mean values for the damaged region are greater than the ODA regions.

The elastic modulus plot for this run is shown in Figure 36.

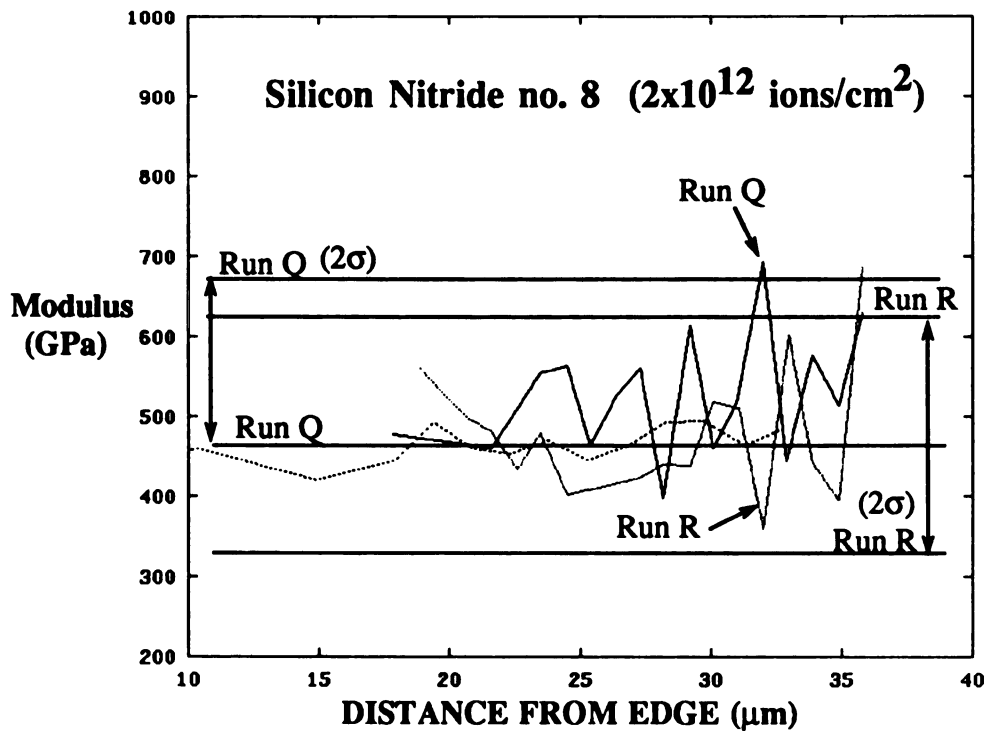


Figure 36 Elastic Modulus of Silicon Nitride no.8 (Runs Q and R)

The statistical data from these runs are as follows:

**$2 \times 10^{12}$  Dose (Run Q) Silicon Nitride Non Damaged Portion Statistics**

samples	mean	std. dev.	sample std. dev.
11	540.2	77.02	80.78

**$2 \times 10^{12}$  Dose (Run Q) Silicon Nitride Damaged Portion Statistics**

samples	mean	std. dev.	sample std. dev.
5	502.2	63.53	71.03

**$2 \times 10^{12}$  Dose (Run R) Silicon Nitride Non Damaged Portion Statistics**

samples	mean	std. dev.	sample std. dev.
13	496.5	84.96	88.4

**$2 \times 10^{12}$  Dose (Run R) Silicon Nitride Damaged Portion Statistics**

samples	mean	std. dev.	sample std. dev.
4	435.5	28.32	32.7

The data, even though very unsmooth, shows no change in the elasticity of the material.

### Control Stainless Steel (Run H, M)

The control (non-implanted) runs of stainless steel were again examined first. Run H off to the side of Stainless Steel no.4 and Run S on Stainless Steel no.2 were averaged and are shown in Figure 37.

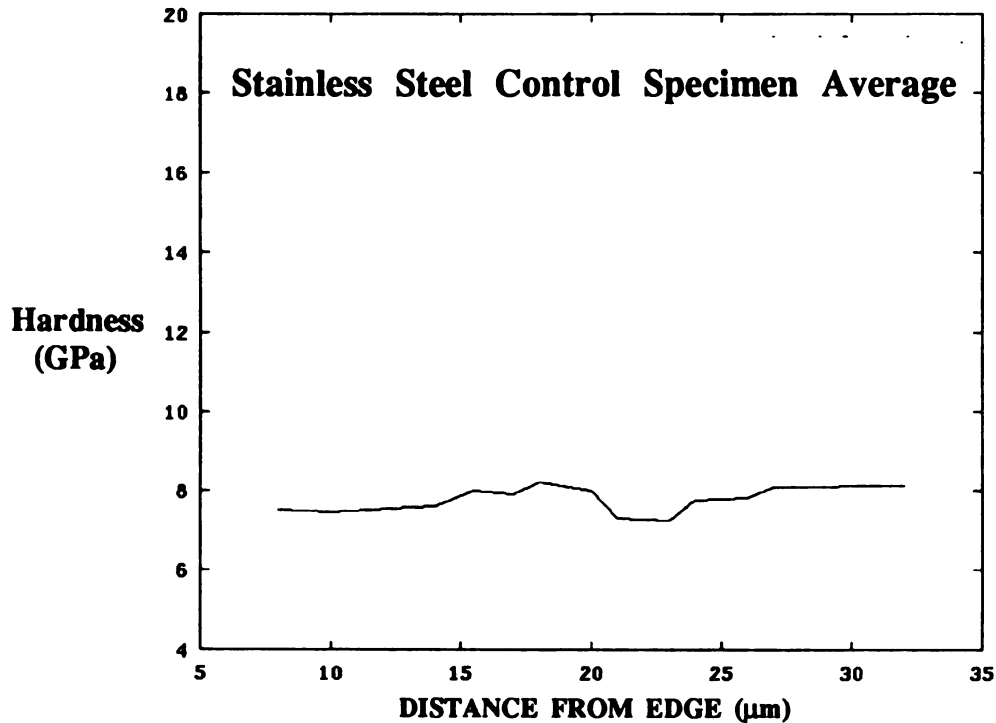


Figure 37 Hardness for Stainless Steel (Control Runs H and M)

The statistical data for this Run is as follows:

#### Averaged Control Entire Run Statistics (Run H, M)

samples	mean	std. dev.	sample std. dev.
14	7.75	0.305	0.316

The softer stainless steel made it easier to obtain a highly polished surface, thus the stainless steel data was much smoother, resulting in smaller standard devi-

ations.

Figure 38 shows the elastic modulus for the Controlled Average Run.

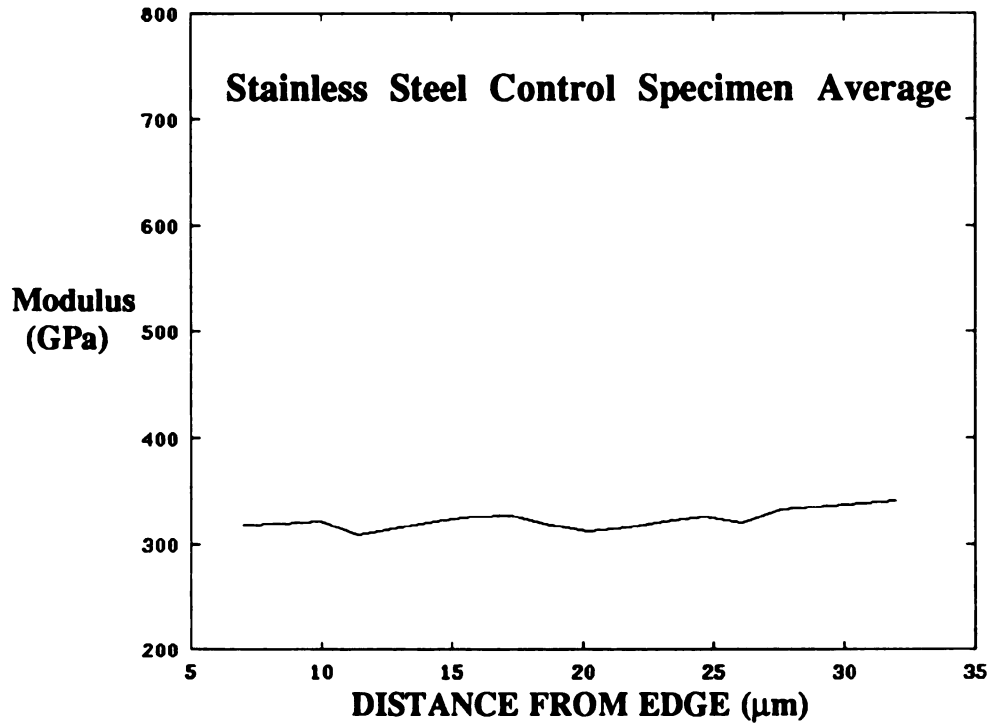


Figure 38 Elastic Modulus for Stainless Steel (Control Runs H and M)

The statistical data for this Run is as follows:

**Averaged Control Entire Run Statistics (Run H, M)**

samples	mean	std. dev.	sample std. dev.
15	322.1	7.68	7.95

## $2 \times 10^{14}$ ions/cm<sup>2</sup> Dose Stainless Steel (Run F, G)

The highest implanted ion dose of Stainless Steel was no.4 ( $2 \times 10^{14}$  ions/cm<sup>2</sup>). Runs G and F were done on Stainless Steel no. 4 and they show good repeatability. Figure 42 shows Run G, F and the Averaged Control Run. A soft region is clearly seen for both Run G and F, around the region of 12 to 21 $\mu$ m, the softest region being 16 to 17 $\mu$ m.

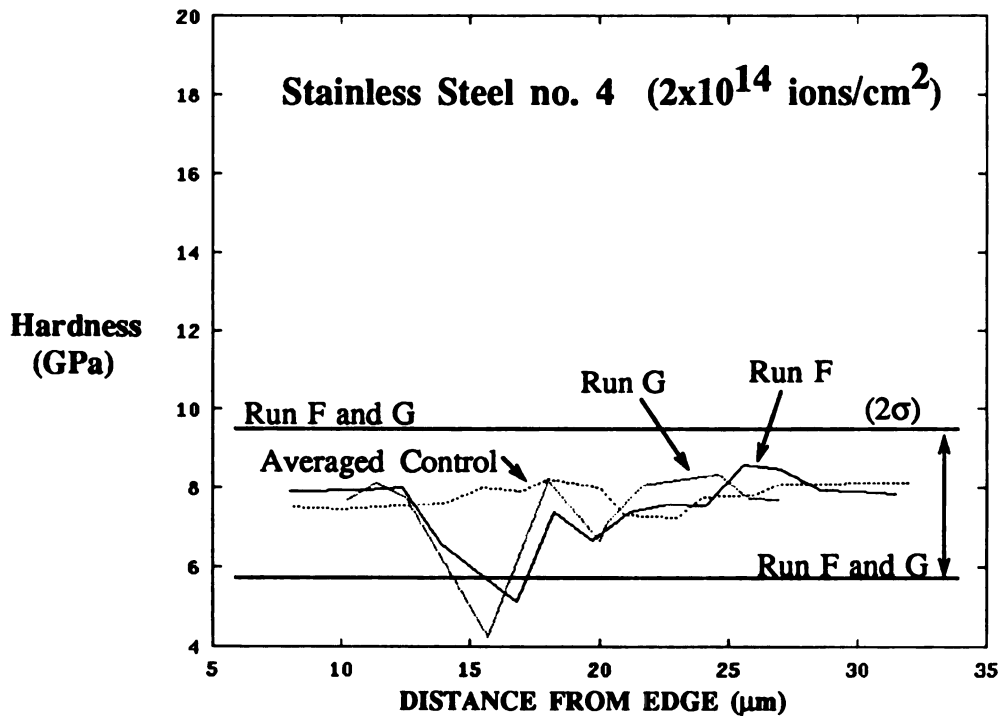


Figure 39 Hardness of Stainless Steel no.4 (Run F and G)

The statistical data on these Runs is as follows:

### $2 \times 10^{14}$ Dose (Run F) Stainless Steel Non Damaged Portion Statistics

samples	mean	std. dev.	sample std. dev.
10	7.98	0.306	0.322

**$2 \times 10^{14}$  Dose (Run F) Stainless Steel Damaged Portion Statistics**

samples	mean	std. dev.	sample std. dev.
5	6.62	0.833	0.931

 **$2 \times 10^{14}$  Dose (Run G) Stainless Steel Non Damaged Portion Statistics**

samples	mean	std. dev.	sample std. dev.
7	7.91	0.239	0.258

 **$2 \times 10^{14}$  Dose (Run G) Stainless Steel Damaged Portion Statistics**

samples	mean	std. dev.	sample std. dev.
5	6.81	1.39	1.56

The damaged region was considered to be 12 to 21 $\mu$ m. Run G, which was more focused on the damaged region, shows a leveling off to the same hardness as Run F. The double soft peaks which were seen in the Silicon Nitride of  $10^{14}$  dosage, can be also seen here but in a less significant state. Comparing the control mean hardness value of 7.75 GPa to that of ODA of Runs F and G, 7.98 and 7.91 respectively shows a maximum deviation of 2.9%. The averaged softening of the material is calculated to be 13.4%. But if the peak softness value is used, an overall maximum softening of the material is 49.5%.

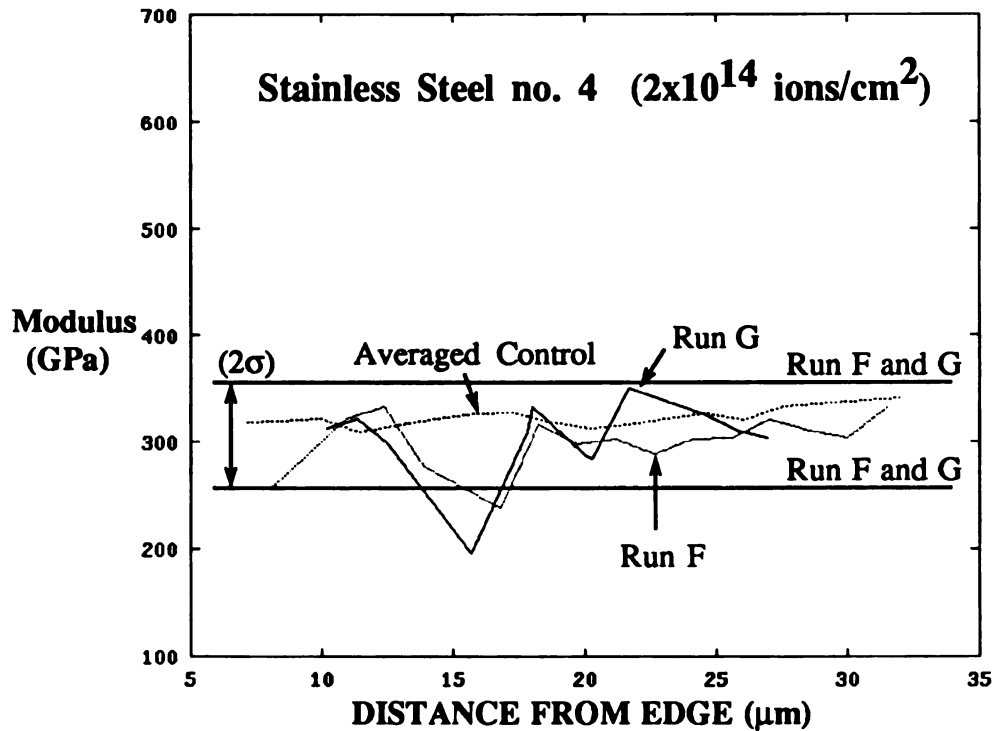


Figure 40 Elastic Modulus for Stainless Steel no.4 (Run F and G)

There is a large similarity between this elastic modulus plot and the hardness plot, both show a drop at 25 $\mu\text{m}$ .

The statistical data for Runs G and F are as follows:

$2 \times 10^{14}$  Dose (Run F) Stainless Steel Non Damaged Portion Statistics

samples	mean	std. dev.	sample std. dev.
10	307	21.95	23.13

$2 \times 10^{14}$  Dose (Run F) Stainless Steel Damaged Portion Statistics

samples	mean	std. dev.	sample std. dev.
5	286	27.5	30.75

**$2 \times 10^{14}$  Dose (Run G) Stainless Steel Non Damaged Portion Statistics**

<b>samples</b>	<b>mean</b>	<b>std. dev.</b>	<b>sample std. dev.</b>
<b>7</b>	<b>317.1</b>	<b>16.08</b>	<b>17.36</b>

 **$2 \times 10^{14}$  Dose (Run G) Stainless Steel Damaged Portion Statistics**

<b>samples</b>	<b>mean</b>	<b>std. dev.</b>	<b>sample std. dev.</b>
<b>5</b>	<b>281.6</b>	<b>46.75</b>	<b>52.27</b>

This shows a 6.8 % decrease in the modulus of elasticity for Run F and a 11.4 % decrease for Run G, an average of 9.1 % using the mean values. Using the extreme values results in a 22.8 % and a 38.5 % decrease for Runs F and G respectively.

## $2 \times 10^{13}$ ions/cm<sup>2</sup> Dose Stainless Steel (Run K, L)

Run K and L were on Stainless Steel no.2 which is the next lower dose of ions ( $10^{13}$  ions), the hardness graph is shown in Figure 41.

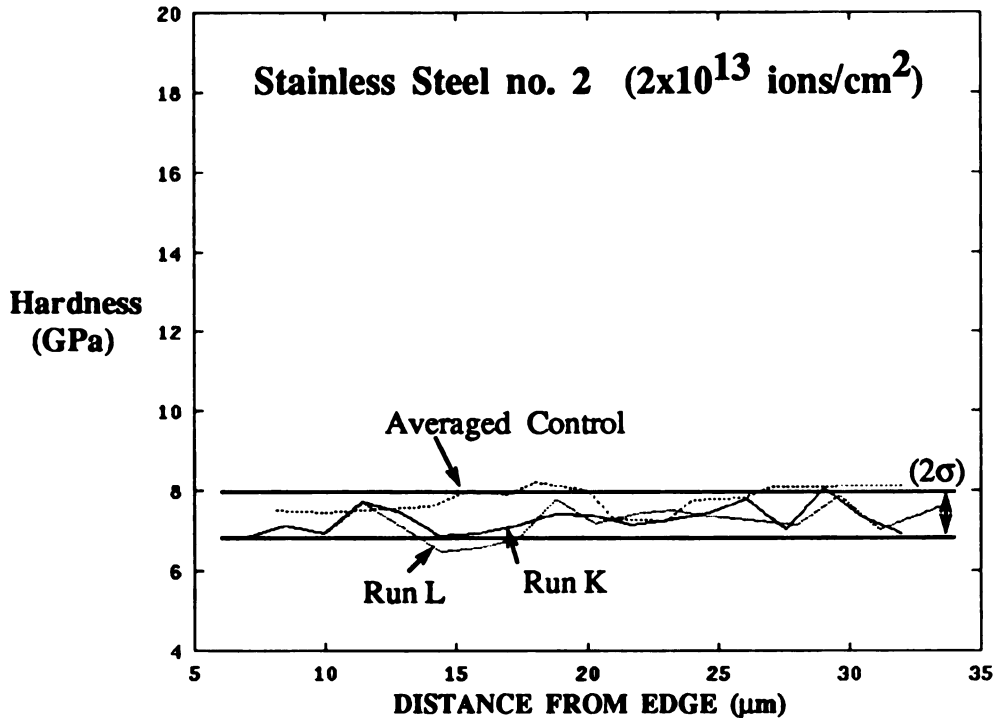


Figure 41 Hardness of Stainless Steel no.2 (Run K and L)

The softening of the material shown previously, but at a much lower significance.

### $2 \times 10^{13}$ Dose (Run K) Stainless Steel Non Damaged Portion Statistics

samples	mean	std. dev.	sample std. dev.
14	7.31	0.373	0.387

### $2 \times 10^{13}$ Dose (Run K) Stainless Steel Damaged Portion Statistics

samples	mean	std. dev.	sample std. dev.
4	7.22	0.199	0.229

$2 \times 10^{13}$  Dose (Run L) Stainless Steel Non Damaged Portion Statistics

samples	mean	std. dev.	sample std. dev.
11	7.29	0.379	0.397

$2 \times 10^{13}$  Dose (Run L) Stainless Steel Damaged Portion Statistics

samples	mean	std. dev.	sample std. dev.
4	7.09	0.453	0.523

The ODA mean hardness values are within 8.5% of each other, making for good repeatability. The average decrease in hardness here is 1.98% which is inside the standard deviation, making the damaged region virtually undetectable according to statistics. If the softest region is used, the decrease in hardness is 11%.

The elastic modulus of Runs L and K are shown in Figure 42.

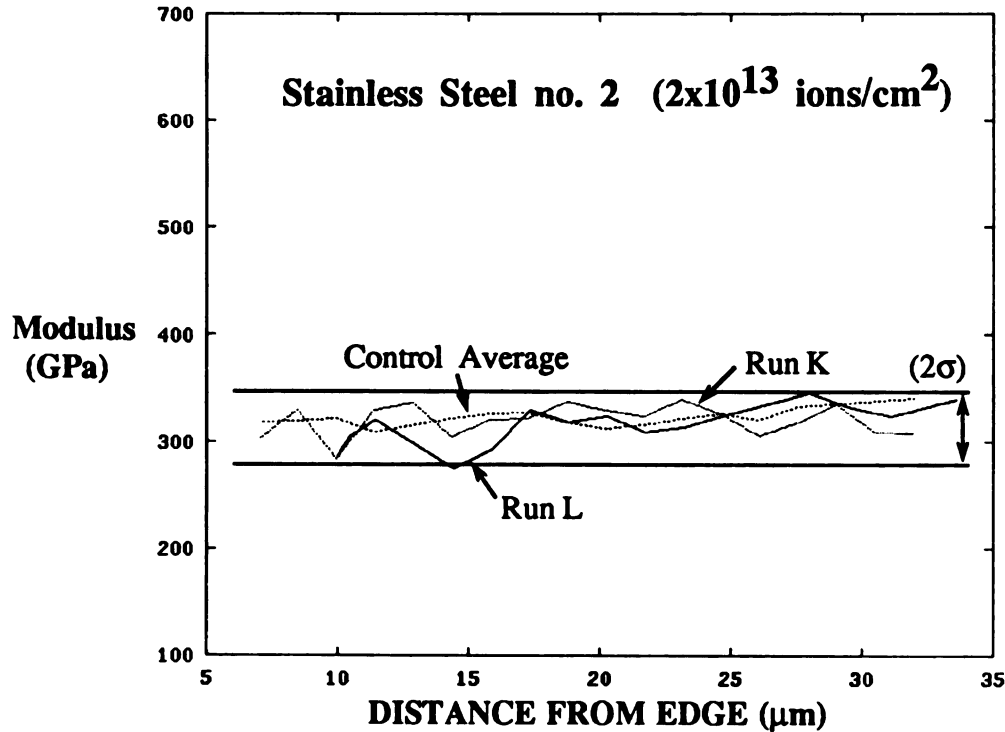


Figure 42 Elastic Modulus of Stainless Steel no.2 (Run K and L)

The statistical data is as follows:

$2 \times 10^{13}$  Dose (Run K) Stainless Steel Non Damaged Portion Statistics

samples	mean	std. dev.	sample std. dev.
14	319.4	15.22	15.8

$2 \times 10^{13}$  Dose (Run K) Stainless Steel Damaged Portion Statistics

samples	mean	std. dev.	sample std. dev.
4	322.5	12.36	14.27

$2 \times 10^{13}$  Dose (Run L) Stainless Steel Non Damaged Portion Statistics

samples	mean	std. dev.	sample std. dev.
10	320	16.8	17.7

$2 \times 10^{13}$  Dose (Run L) Stainless Steel Damaged Portion Statistics

samples	mean	std. dev.	sample std. dev.
5	307.8	20.9	23.37

Run K shows no apparent change at  $25\mu\text{m}$ . Run L shows a 3.8% decrease in damaged region but the decrease falls inside the large ODA standard deviation of 16.8 from the mean value of 320 which drops the allowable ODA deviation to 303.2 which is actually lower than the dip in the damaged region. Thus the stainless steel can be assumed to have no change in elastic modulus at this dosage.

## $2 \times 10^{12}$ ions/cm<sup>2</sup> Dose Stainless Steel (Run P)

The lowest dose ( $2 \times 10^{12}$  ions) was on Stainless Steel no.1 which is tested in Run P. Only one Run was performed due to time constraints. Run P shown in Figure 43 shows no distinct softening of material as would be expected from the trend of previous data.

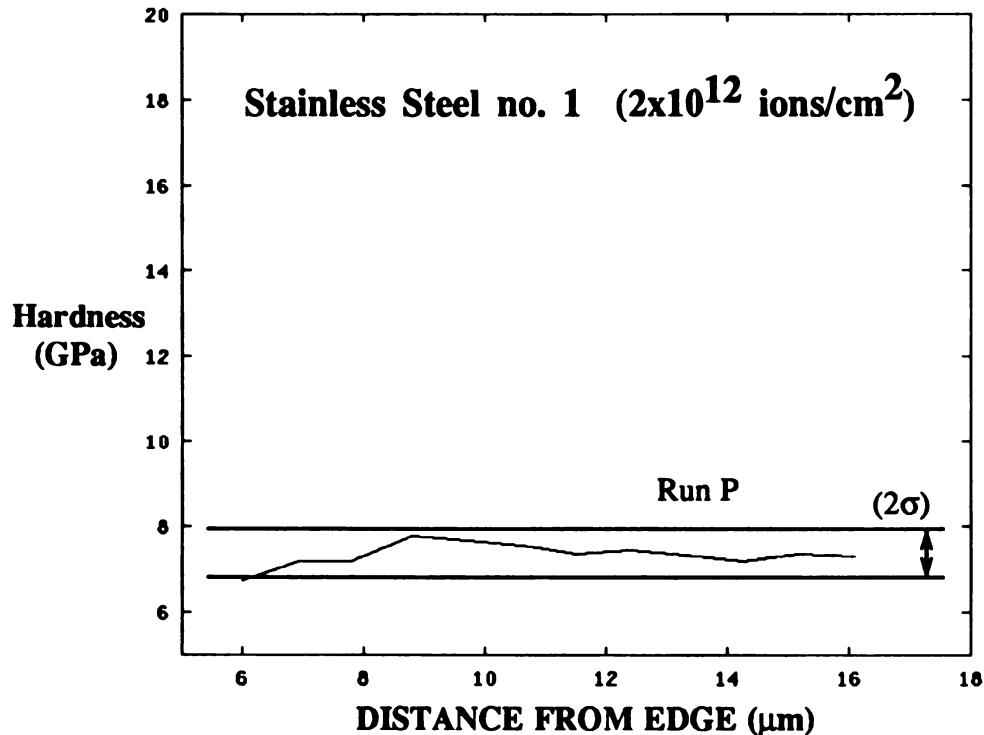


Figure 43 Hardness of Stainless Steel no.1 (Run P)

The statistical data is as follows:

### $2 \times 10^{12}$ Dose (Run P) Stainless Steel Entire Portion Statistics

samples	mean	std. dev.	sample std. dev.
11	7.31	0.25	0.26

The Control Average has a mean of 7.75, a standard deviation of 0.305 and a sample standard deviation of 0.32 which is very similar to this run.

Figure 44 shows the elastic modulus of Run P.

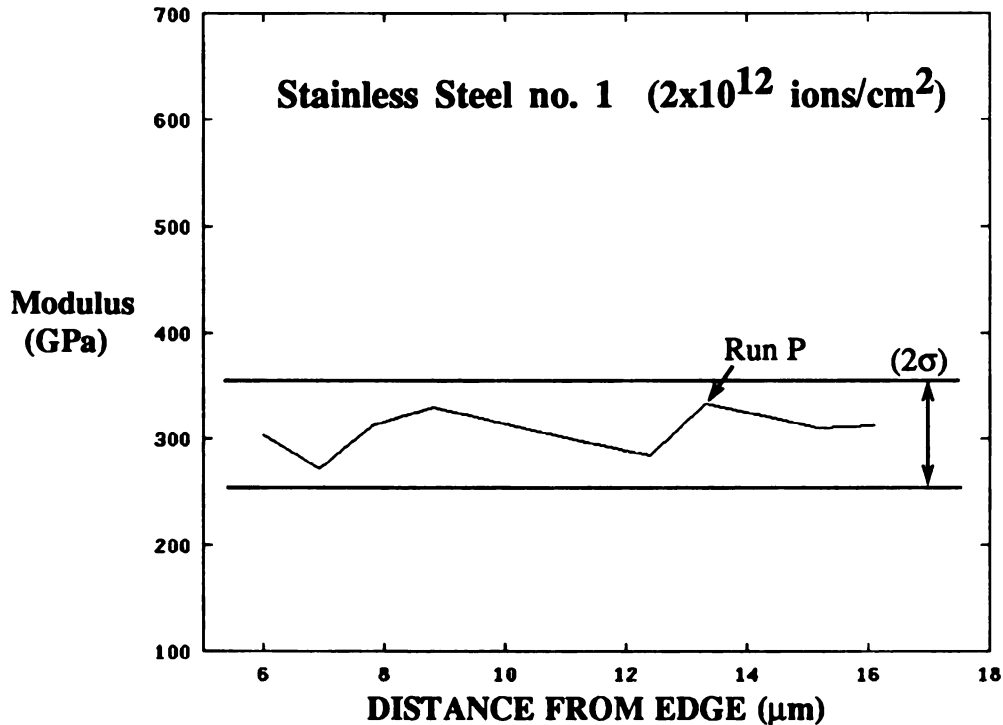


Figure 44 Elastic Modulus of Stainless Steel no.1 (Run P)

$2 \times 10^{12}$  Dose (Run P) Stainless Steel Entire Portion Statistics

samples	mean	std. dev.	sample std. dev.
11	317.45	36.39	38.17

The large point near 10μm, causes some problems, if it is eliminated the mean is 307.4, the standard deviation is 18.56 and the sample standard deviation is 19.57 which drops the statistics dramatically but still does not drop them to the Control Run values.

The smooth surface and low variation in data points outside the damaged portion for the stainless steel indicated that the spacing between indents was adequate. If the spacing had not been close enough, the data would be more erratic, much like the silicon nitride data. Ironically with the stainless steel being a softer material, the indenter penetrated deeper into the material thus requiring the indents further apart

than those in the hard silicon nitride. In the stainless steel, the indents were placed approximately 8  $\mu\text{m}$  apart, since the apparent width of the indent was 4  $\mu\text{m}$ . Traversing the damaged region at an angle, the resolution between indents from the edge is at best 1.8  $\mu\text{m}$ . The indents in the silicon nitride were less than 1  $\mu\text{m}$  in width and placing the run at an angle, a 0.8  $\mu\text{m}$  resolution between indents from the edge was achieved. Even with this better resolution, the points were too far apart for the silicon nitride's rough surface. The data was too scattered for comfort, but fortunately the damaged regions could still be seen.

### 4.3 TRIM

TRIM predicted a damaged depth of 17.8  $\mu\text{m}$  with a FWHM of 0.25  $\mu\text{m}$  for the silicon nitride, and a depth of 10.5  $\mu\text{m}$  and a FWHM of 0.5  $\mu\text{m}$  for the stainless steel. The results showed a damaged region in the silicon nitride from 22 to 29  $\mu\text{m}$  with the maximum damage at 25  $\mu\text{m}$ . The stainless steel damaged region was from 12 to 21  $\mu\text{m}$  with the most change at 16  $\mu\text{m}$ . The silicon nitride shows a sort of double soft region while the stainless steel shows more of a distinct softening at a point. This error between the two is not distinctive of TRIM. One reason for the error may be in that TRIM considers the target to be amorphous with atoms at random locations, and thus directional properties of the crystal lattice are ignored. Also the nuclear reactions are not considered in TRIM. These may be subjects that might change the results a little but certainly not enough to match the experimental results. The plots of TRIM shown were for an ion dosage of only  $10^4$  ions/cm<sup>2</sup> due to the amount of computer time required. If the desired  $10^{14}$  ions/cm<sup>2</sup> dosage was run, the maximum concentration peak would stay the same, but the FWHM would grow, resulting in a damage region of greater than 0.5  $\mu\text{m}$ . But the TRIM's result would most likely be far from the experimental result.

A more likely error would come from the physical set up of the specimens in the beam line. The intersection of the flats of the two specimens, where the beam penetrated into the crack, could be the cause of conflicting implanted depths. Under 5000 X magnification, the intersection of the two specimens was quite obvious, the crevice caused by the surfaces not being perfectly smooth. Under high magnification the surfaces would be rough, with the specimen flats riding on each others ridges, see Figure 45.

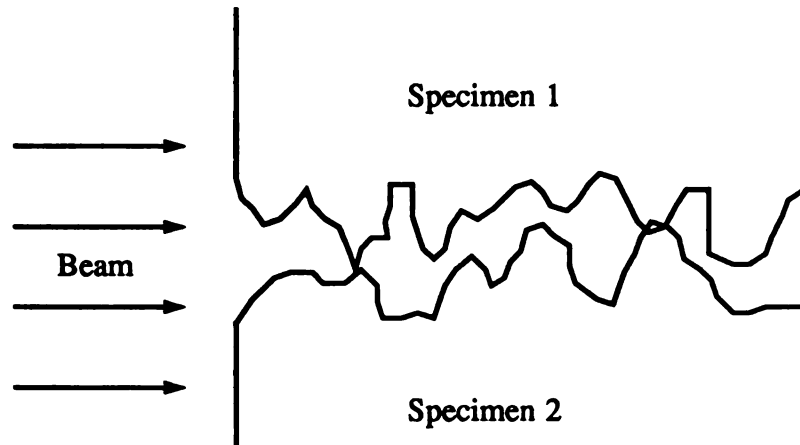


**Figure 45 Beam Incident on Magnified Specimen Contact Surfaces**

As seen in TRIM, the beam penetrates a set amount of material and then deposits ions at that location. Using this scenario, the beam will enter the crack, travel through several voids and material peaks until it has penetrated the set amount of material. This will cause the ions to be implanted at a distance further in than if the beam penetrated solid material. The beam that travels along the centerline of the crack will encounter a less dense material and deposit further into the material, resulting in a distance implantation profile as shown in Figure 46.

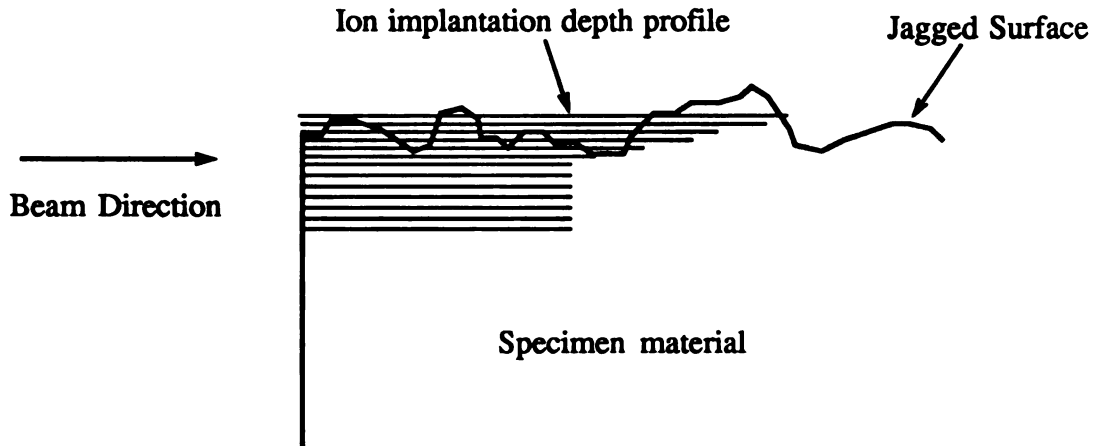


Figure 46 Varying Ion Implantation Depth with Jagged Surface.

The maximum depth of the indent was 200 nm which is 0.2  $\mu\text{m}$ . This depth could be at the same magnitude as the surface finish of the silicon nitride, meaning that the depth of the indent may not be deep enough to overcome the varying surface implantation depths, see Figure 47.

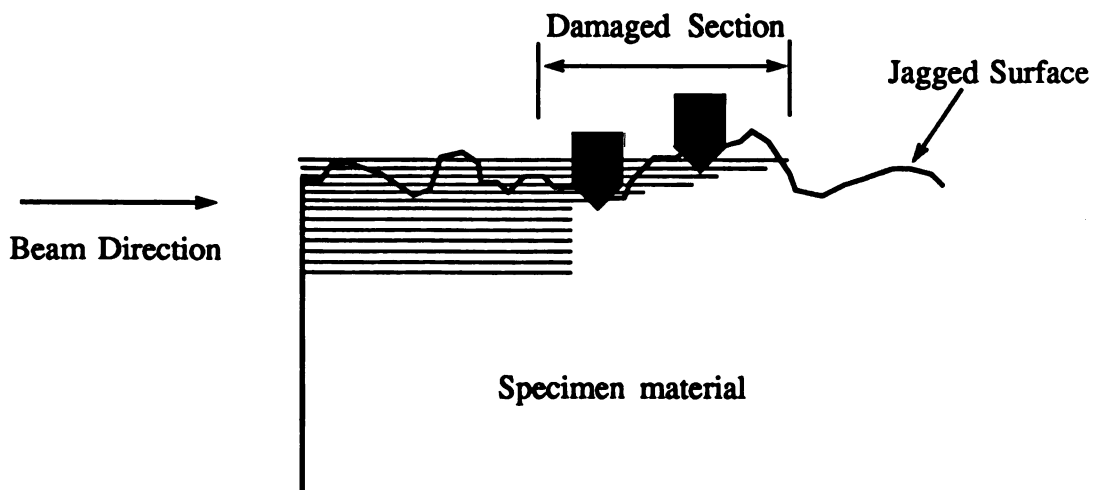


Figure 47 Indentation of Deeper Implanted Regions

Using this scenario, the damaged regions would be located deeper than expected and would also be broader than expected. Also, the smoother the specimen's surface, the closer the damaged depth would be to the calculated depth. With this in mind, the error in damaged depth of the stainless steel is 5.5  $\mu\text{m}$  where the error in depth for the silicon nitride is 7.2  $\mu\text{m}$ . According to the hardness data, the stainless steel had the smoother surface.

## CHAPTER 5

### SUMMARY AND CONCLUSIONS

1) The implantation dosage of  $2 \times 10^{14}$  ions/cm<sup>2</sup> caused a change in hardness and elastic modulus in both the stainless steel and silicon nitride. The threshold local dosages for both the stainless steel and silicon nitride is  $2 \times 10^{13}$  ions/cm<sup>2</sup>, to be conservative. The stainless steel having a better surface finish, enabled the data to be smoother, thus easier to read. Both materials showed no radiation damage at the lower dose of  $2 \times 10^{12}$  ions/cm<sup>2</sup>, thus the threshold implantation dosage to create material property change was achieved.

2) An implanted sample for wear studies would contain a series of these local implants, the threshold for implant based on these studies is an order of magnitude greater than that which caused local damage.

3) The measured hardness and elastic modulus values for both the silicon nitride and the stainless steel were high when compared to tabulated values. The measured silicon nitride hardness was 30.78 GPa, compared to a typical documented value of 13 GPa. The measured modulus of elasticity was 462.3 GPa compared to 380 GPa typical. The measured stainless steel hardness was 7.9 GPa while the typical value is 1.05 GPa. The measured modulus of elasticity was 322.1 GPa and 200 GPa for the theoretical. The high values are typical of nano indentation tests. The data was used in a relative sense, so exact hardness was not needed.

4) The implanted  $2 \times 10^{12}$ ,  $2 \times 10^{13}$  and  $2 \times 10^{14}$  ions/cm<sup>2</sup> non radioactive ions were carefully chosen to equal to the number of radioactive ions to produce a required activity for wear analysis. Using these dosages, the resulting radioactivity of Na<sup>22</sup> ions would yield 0.228, 2.28 and 22.8  $\mu$ Ci respectively. If Be<sup>7</sup> ions were implanted at these dosages, the resulting activity would be 4.06, 40.6 and 406  $\mu$ Ci respectively.

5) The nano indenter machine is set up so that no reading calibration is needed other than horizontal plane calibration (x-y plane). Thus the same hardness values should occur at different times, but this was not the case. Noting humidity change as our only time variant, the variation in hardness was from 30.78 GPa for the Averaged Control Run to 40.55 GPa for Run C, an unexplained variation of 24%. The same variation shows up in the modulus of elasticity values for that same day. The Nano In-

denter is an extremely sensitive machine, one which corrects for thermal drift. There seems to be a need for other ambient corrections such as humidity change as well.

6) The detected gamma ray from the silicon nitride no. 6 specimen, had an energy of 271.07 KeV. This energy could not be found in the Radiation Tables. This measured energy value has an estimated error of at most 3 KeV, which still does not match a known gamma ray to our created gamma ray. There is a possibility, in the path of new research, to come across new results. Before introducing this possible new gamma ray, more samples should be examined.

7) From these results, the Ion Implantation method is an excellent radiotracer wear detection method as long as the threshold implanted ion dose is not reached.

8) A engine wear ion detection system was designed for internal combustion engine studies, shown in the appendix.

## **Chapter 6**

### **RECOMMENDATIONS**

In order to continue the progress toward a better understanding of the damage effects of Ion Implantation, these recommendations for future work seem appropriate.

1. A more highly polished specimen surface needs to be obtained. More non-diamond compounds and chemical etching should be included in the final preparation process.
2. A secure and easy specimen mounting system should be designed and fabricated for the Nano Indentation Machine to ensure proper alignment and flatness of specimen mounted surfaces.
3. The cyclotron beam should be more controllable, resulting in less beam current fluctuations. A higher beam current would most likely be more stable and also more economical for implanting high ion doses.
4. The testing of implanted samples with polyenergetic ions will provide additional verification of wear damage. Battelle Memorial Institute of Columbus, Ohio is planning to provide this testing. These implanted samples must be used in engine tests to determine the factors that influence wear measurement under realistic conditions. This work could begin with SLA activated parts.

## **REFERENCES**

## LIST OF REFERENCES

1. Personal communication.
2. Bhattacharya R.S., Rai A.K., Pronoko P.P.. "Journal of Applied Physics.", 15 May 1987, 61, (10) 4791-4794.
3. Townsend P.D., "Rep. Prog. Physics,", May 1987, 50, (5), 501-558.
4. Burggraaf A.J., Gelling P.J., Scholten D.. "High Tech Ceramics." (Part A) [Processing Conference], Milan, Italy, 24-28 June 1986, Elsevier Science Publishers.
5. Cochran J.K., Legg K.O., Solnick H.F.. "Defect Properties and Processing of High-Technology Nonmetallic Materials." [Processing Conference], Boston, USA, 14-17 Nov. 1983, Elsevier Science Publishers.
6. Oliver W.C., McHargue C.J., Farlow G.C., White C.W.. "Defect Properties and Processing of High-Technology Non-Metallic Materials." [Processing Conference], Boston, Massachusetts, USA 2-4 Dec. 1985, Materials Research Society.
7. Burkhardt T., McHarris W., Chung Y., Lloyd J., Rachel T., Schock H., Grummon D., Shalek R., Ronningen R., Mallory M.. "Developments in High Energy Ion Implantation for Wear Studies." Michigan State University, Status Report MSUERL-90-5. 1990.
8. Personal communication.
9. Mallory M., Schock H., McHarris W., Ronningen R., Sherill B.. "Production and Implantation of  $^7\text{Be}$  For Wear Analysis.", Michigan State University Report, Nov. 17, 1988.
10. General Electric, 'Chart of the Nuclides', Nuclear Energy Operations, 175 Curtner Avenue, M/C 684, San Jose, California 95125 U.S.A.
11. Ziegler J.F. Biersack J.D., Littmark U.. 'The Stopping Power of Ions in Solids.'

Pergamon Press Inc., Maxwell House, Fairview Park, Elmsford, N.Y. 10523 U.S.A.

12. Cathcart J.V. "Operating Instructions for the Mechanical Properties Microprobe.", High Temperature Materials Laboratory. Oak Ridge National Laboratory, Oak Ridge, Tennessee. September 1988.
13. Personal communication.
14. Blau P., "The Lab Handbook of Microindentation Testing." Oak Ridge National Laboratory, Oak Ridge, Tennessee. (1988).
15. NC 132 Material Documentation. Norton Company, Industrial Ceramics Division, Worcester, Mass. 01606
16. Tanaka I., Pezzotti G., Okamoto T., Miyamoto Y., Koizumi M.. "Hot Isostatic Press Sintering and Properties of Silicon Nitride without Additives." *Journal of American Ceramic Society.*, 72 [9] 1656-60 (1989).
17. Lindeburg M. Engineer in Training Review Manual, Sixth Edition. Professional Publications, Inc. Belmont, CA 94002.
18. Mallory M. L. *IEEE Trans. Nucl. Sci.*, NS-30, No.4 (1983) 2061.
19. Caskey G., Heilbronn L., Remington B., Galonshy A., Deak F., Kiss A., Seres Z., MSUCL-626, Michigan State University, Preprint (Nov. 1987).
20. Remington B. S., Caskey G., Galonshy A., Gelbke C.K., Heilbronn L., Heltsley J., Tsang M.B., Deak F., Kiss A., Kasagi J., Kolata J.J.. *Phys. Rev. C*, 34 (1986) 1985.
21. Lynch W. G., *Ann. Rev. Nucl. art. Sci.*, 37:1 (1987) 493.
22. Mallory M. L. Proc. 11th Int. Conf. on Cyclotrons and Their Applications, Ionics, Tokyo (1987) 558.
23. Ajsenberg-Selove F. and Lauritsen T. , *Nucl. Phys.*, A227 (1974) 68.

## **APPENDIX**

### **DESIGN OF A PISTON RING WEAR MEASUREMENT SYSTEM FOR ION IMPLANTATION**

Even though the main thesis is based on the question of material property change due to ion implantation, a system to actually use the wear measurement technique has been designed and documented but has yet to be run. The system consists of a one cylinder research engine, dynamometer, oil and piston ring ion detection systems and an exhaust dilution system.

#### **Research Engine**

The engine chosen for the study of radioactive piston ring wear was a one cylinder 11 HP Briggs and Stratton Engine model number 254422, type 4015-01, with an aluminum block, cast iron bore which was donated by Briggs and Stratton. The engine is a compact, self sufficient unit that controls its engine speed via a carburetor governor. The Briggs and Stratton engine is mechanically simple, reliable and parts are readily available. The design of the engine makes it less sensitive to bolt torque tolerances and leaves little room for mistakes in assembly, making it a good choice for frequent tear down. The engine has several oil holes for easy connection to an external oil detection system. The engine also has a low oil shut off system that shuts the engine off when the oil level is low. This option is a good safe guard since the engine oil will move through the engine into other components for oil detection. The engine is turned off by grounding the ignition ground wire (not spark). The top ON/OFF switch merely makes or breaks contact with the grounded engine cover. This switch was disconnected and the grounding wire attached to a red cut out button on the dynamometer's control panel for quick engine cut out. The low oil cut out switch is operated using a float which rises up when the oil level is at the correct level, opening the switch so that the ignition switch is not grounded. When the oil level drops to a certain level, the switch closes, grounding the ignition and thus stopping the engine. The grounding of the oil switch also causes a red bulb to glow on the front cover of the engine. The recommended oil capacity is a 1.25 quarts, but the engine is not full until 2 quarts are used.

Besides detecting the engine oil, a piston ring will be detected. The second compression piston ring was chosen to be radiated in order to distribute more of the radioactive ions in the oil. Placement of the detector in relation to the radioactive portion of the ring is critical. In order to keep the second piston ring from rotating about the piston, the piston ring was pinned. To pin the piston ring, notches were made in both ends of the piston ring. Then a hole was drilled in the piston secondary ring groove at an area of thick piston wall. A hardened pin was then pressed into the hole and the piston ring installed so that the grooves matched up with the pin. This pinned ring design makes it impossible for the pin to come out of the piston since the notch is constantly pressing on the pin. The pinned ring was done early in the break in period of the engine so that wear patterns were created in junction with the non rotating piston ring. The one gallon stock fuel tank were replaced by a five gallon fuel tank to accommodate the fuel supply for the long wear data runs.

### **Dynamometer**

The dynamometer is used to produce a load on the engine. With the dynamometer, the engine can be run at a set speed or a set torque can be placed on the research engine. The dynamometer can also be used to motor or even start the engine. The dynamometer is a EATON 50 HP eddie current dynamometer controlled by DYNAMATIC controllers, all of which was donated by NASA.

The dynamometer's support bed is extended for mounting the engine on to the bed. An engine stand was made to support the engine and to also match the engine's drive shaft with the dynamometer's drive shaft. The engine stand was make of three inch channel for the legs and half inch steel plate for the base plate. The half inch plate was drilled and tapped to the engine's bolt hole pattern. The dynamometer's bed was also drilled and tapped to secure the engine stand. A two inch tall steel lip was welded around the engine stand's base plate as a safety measure to contain the engine oil in case of a spill. The basin created by the lip allows for containment of all the engine oil.

There must exist a flexible coupling between the dynamometer and the engine, so that engine vibrations are not transmitted through the drive shafts. A Sure Flex sleeve rated at 25 HP and fourteen degrees rotational flexibility was used as the coupling, any less flexibility would shear under load.

Running the engine and dynamometer indoors caused noise and exhaust problems, so the dynamometer was made mobile by placing it on caster wheels. A rail

system was made to guide the wheels out a bay door to the outdoors. The track was long enough as that the dynamometer could be completely removed from the building and the bay door closed. To accommodate this mobile dynamometer, long water and electrical lines were used and the control panel stand was also put on wheels. The control panel controls the entire dynamometer / engine setup.

The dynamometer is always run in manual mode, and either in the drive or absorb mode. In absorb mode, the dynamometer absorbs power from the firing engine which can be controlled by the speed indicator. In drive mode, the dynamometer drives the non firing engine. Drive mode is only used for starting the engine in the present setup. The red button on the top of the control panel, when pulled out will enable the engine and dynamometer to operate. When pushed in, the engine's ignition and the absorbing power of the dynamometer is cut off. On the control panel, there is a torque indicator which displays a voltage which is read from the load cell on the dynamometer. The gauge must be plugged into the load cell on the dynamometer. The torque indicator always reads negative since the load cell is on the tension side of the dynamometer. The load cell reads a voltage which must be multiplied by a calibrated conversion factor, which is currently 60 ft\*lbs/volt.

The dynamometer requires water as a cooling medium to flow through it. Safety features require water for the dynamometer to operate. Thermocouples are placed in the inlet and outlet water lines which read the water temperature. A thermocouple box on the bottom of the control panel stand must be plugged into the thermocouples in order to view the inlet and outlet water temperatures. The dynamometer does not automatically turn off when it gets too hot so the water temperature must be watched closely.

### **Oil and Piston Ring Ion Detection System**

The oil detection system transports the ion contaminated oil to the gamma detector in a manner which makes the detector most susceptible to gamma ray interception. The stock Briggs and Stratton engine contains no oil pumping system, the engine components are oiled by the means of an arm connected to the crank which splashes oil up on the components. An external oil pump is used to move the oil around the oil detection system. The oil, which is heated in the engine, must be cooled before surrounding the germanium detector. Warming of the detector would first lead to an large increase in system noise resulting in increased dead time, then the safety features would turn the detector off. The oil is cooled by a liquid to liquid

heat exchanger using water as the cooling medium. A oil sheath was designed to slip over the end of the detector and cover the entire ion detecting chamber. The oil enters one side of the oil sheath through a mixing board and exits out the bottom opposite side. This design of totally encapsulating the detector with the contaminated oil will give the best rate of gamma rays interception by the detector. Flexible tubing was used to transport the oil between the components because some relative movement is needed between the engine and other oil components since the dynamometer rolls in and out.

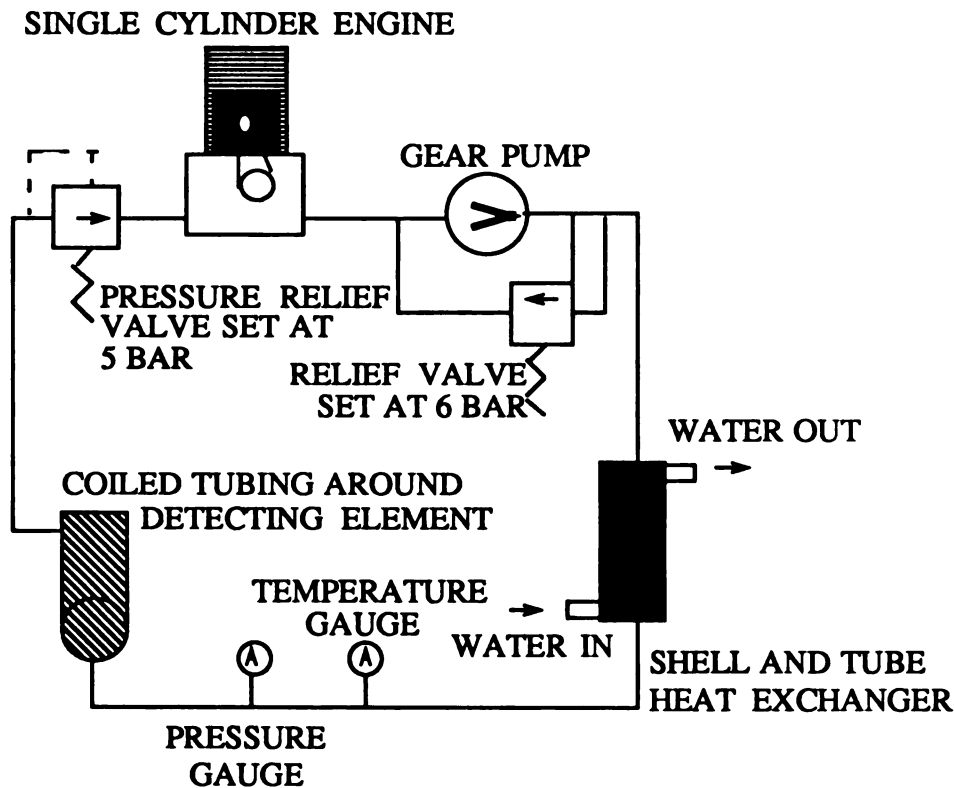


Figure 48 Oil Detection System

The total system oil capacity is approximately 4.4 quarts. The recommended time between oil changes for the engine is 50 hours of run time. Using a crude method of proportions, the oil should be changed every 126 hours. The ideal case is not to have to change the oil at all since an oil change modifies the activity of the oil.

To detect ions exiting through the block, the germanium detector has to be placed close to the block. An engine mounted stand was designed to hold the detector secure close to the block where the activated portion of the piston ring was locat-

ed. The stand mounts to the head bolts and lower engine mount bolts. Gamma ray detection at the engine block must be done while the engine has stopped and the piston is at top dead center. Positioning of the activated portion of the piston ring and detector is critical.

### Exhaust Dilution System

In order to meet safety regulations governing the amount of radioactive ions being exhausted to the atmosphere from the engine, an exhaust dilution system is required. The system has to dilute the contaminated exhaust and send it to a location where winds would not have a tendency to blow the contaminant into the building. The system had to dilute the exhaust so that the concentration of radioactive ions was well inside the limit of safety. The system had to also endure the weather conditions since the system operated outdoors. The radioactive ion to be implanted in the piston rings is  $^{54}\text{Mn}$ .  $^{54}\text{Mn}$  has a branch ratio of 99.98% , a half life of 0.878 years and a gamma ray energy of 834.83 KeV. The engine has a displacement of  $392 \text{ cm}^3$ , an assumed volumetric efficiency of 70% and an operating speed of 3300 rpm. The ion concentration in the exhaust was calculated for worst case as follows:

$$^{54}\text{Mn} \text{ Probability of decay} = \lambda = \ln 2 / \text{half life} = 1.5125 \times 10^{-6} / \text{sec.}$$

$$\begin{aligned} \text{Volumetric flow rate of engine} &= \text{displacement}/2 * \text{rpm} * \text{pumping efficiency} \\ &= (392 \text{ cm}^3 / 2) (3400 \text{ rev}/\text{min}) (0.7) = 466480 \text{ cm}^3 / \text{min.} \\ &= 7774.7 \text{ cm}^3 / \text{sec.} \end{aligned}$$

$$\begin{aligned} \text{Maximum expected activity of piston ring} &= 10 \times 10^{-6} \text{ Ci} (3.7 \times 10^{10} \text{ dps} / \text{Ci}) \\ &= 3.7 \times 10^5 \text{ dps.} \end{aligned}$$

$$\begin{aligned} \text{Number of ions of } ^{54}\text{Mn} \text{ associated with } 3.7 \times 10^5 \text{ dps} &= \text{activity} / \text{probability of decay.} \\ &= 3.7 \times 10^5 \text{ dps} / 1.5125 \times 10^{-6} / \text{sec.} \\ &= 2.446 \times 10^{11} \text{ ions.} \end{aligned}$$

Maximum ion wear rate of engine = number of ions / time to wear away all ions.

$$= 2.446 \times 10^{11} \text{ ions} / 200 \text{ hours (min time).}$$

$$= 3.397 \times 10^5 \text{ ions/sec.}$$

Concentration of ions in exhaust = wear rate / mass flow rate of engine.

$$= 3.397 \times 10^5 \text{ ions/sec} / 7774.7 \text{ cm}^3/\text{sec}$$

$$= 43.7 \text{ ions} / \text{cm}^3 .$$

Activity of ion in exhaust = probability of decay \* concentration of ion in exhaust.

$$= (1.5125 \times 10^{-6} / \text{sec}) * (43.7 \text{ ions} / \text{cm}^3) * (2.7 \times 10^{-5} \text{ } \mu\text{Ci} / \text{dps})$$

$$= 1.78 \times 10^{-9} \text{ } \mu\text{Ci} / \text{cm}^3 .$$

Hence the calculated undiluted ion concentration in the exhaust is  $1.78 \times 10^{-9} \text{ } \mu\text{Ci} / \text{cm}^3$ . For  $^{54}\text{Mn}$  ion in an unrestricted area, the Office of Chemical and Biological Safety (ORCBS) - "Standards for Protection Against Radiation" maximum permissible concentration form 10CFR20 states a maximum permissible concentration of  $1 \times 10^{-9} \text{ } \mu\text{Ci} / \text{cc}$  of air. So a dilution system is needed in this worst case scenario. The dilution is accomplished by adding more air to the exhaust. A positive displacement blower was chosen since the flow rate is known for a given blower speed. Using various blower flow rates in place of the engine's volumetric flow rate, blower flow rates affecting concentration can be found.

Table 15 Exhaust Activity Verses Blower Flow Rate.

ACTIVITY ( $\mu\text{Ci} / \text{cc}$ of air)	FACTOR OF SAFETY	CFM REQUIRED
$1.78 \times 10^{-9}$	0.59	17.4
$1.00 \times 10^{-9}$	1.00	29.4
$1.00 \times 10^{-10}$	10.00	294.0
$1.00 \times 10^{-11}$	100.00	2940.0
$1.00 \times 10^{-12}$	1000.00	29400.0

The exhaust dilution system contains a blower, exhaust stack and ion detector in the stack to monitor activity level. The diluted stack must be attached to the side of the building extending 15 feet from the roof. This 15 feet was an estimated height for a given building height and flow rate out of the stack from the MSU Building and Planning Office. The exhaust stack is an aluminum four inch diameter tube, with all joints sealed. The flexible connection between the movable dynamometer and the permanent stack is made of heat resistant rubber material. The blower and blower motor assembly is mounted on wheels in order to be mobile.

A ion detection monitor is placed in the stack to show if ion concentrations were getting too high, from possible mechanical failure. The monitor shows a count per minute reading which can be related to the activity.

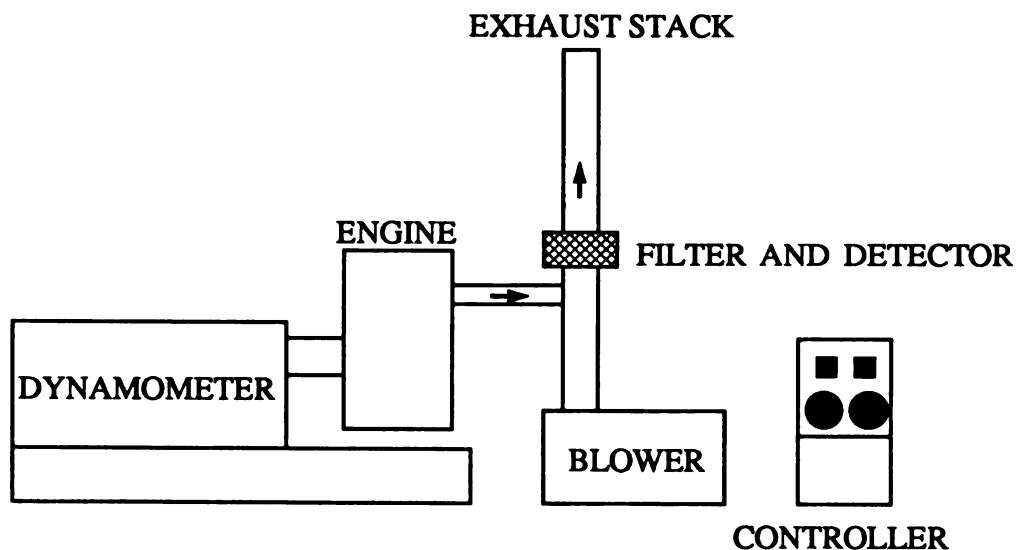


Figure 49 Exhaust Dilution System

The operation of the wearing ion detection in a running engine will occur at a later date.

MICHIGAN STATE UNIV. LIBRARIES



31293009008842